Semiconductor laser transmitter for water vapor lidar on Mars
by Greggory W Switzer

A thesis submitted in partial fulfillment of the requirements for the degree of Doctor of Philosophy in Physics
Montana State University
© Copyright by Greggory W Switzer (1998)

Abstract:
This dissertation investigates the feasibility of a novel, low power miniature lidar intended to measure the vertical distribution of atmospheric water vapor on Mars. This instrument could provide valuable information crucial to understanding the past and present climate of Mars. The emphasis is to develop a compact, efficient, allsemiconductor laser transmitter and demonstrate its ability to measure water vapor at high and low atmospheric pressures.

Current lidar systems are too large, complicated and require too much electrical power to be considered for a space-born mission. Recent advancements in high power semiconductor lasers and highly sensitive semiconductor detectors have, for the first time, made it possible to develop a small, rugged, lidar system that could meet the strict requirements for a future Mars Lander mission.

The laser transmitter consists of a wavelength tunable, single mode, narrow linewidth external cavity diode laser whose CW output is amplified and pulsed using a flared semiconductor amplifier. The pulsed output of the device must be able to scan its wavelength across the strongly absorbing &lambda = 935.68nm water vapor absorption line without frequency chirp. The desired output of the external cavity diode laser was modeled based on its mechanical and optical design. The laser was designed, machined, assembled and its output was characterized. The laser was used to optically seed a flared semiconductor amplifier whose drive current was pulsed. The combined transmitter emitted 0.36μJ pulses that were free from frequency chirp.

The pulsed transmitter beam scanned the water vapor absorption line at low pressures using a multipass optical cell. The profile of the measured absorption line agrees with the profile predicted using HiTran ’96 atmospheric database to within a few percent. The maximum altitude the lidar could measure during sunlit conditions on Mars was estimated based on the laser transmitter output and optical receiver parameters of the current bread board system. A maximum altitude of 1.3km for measuring water vapor and 3.2km for aerosols was theoretically predicted using estimates of the atmospheric conditions from previous missions to Mars. Simple improvements would enable the lidar system to measure the dynamics of the water vapor up to 5km.

SEMICONDUCTOR LASER TRANSMITTER FOR WATER VAPOR LIDAR ON MARS

by

Greggory W. Switzer

A thesis submitted in partial fulfillment
of the requirements for the degree

of

Doctor of Philosophy

in

Physics

MONTANA STATE UNIVERSITY – BOZEMAN
Bozeman, Montana

November 1998

D378
Sw68

APPROVAL

of a thesis submitted by

Greggory W. Switzer

This thesis has been read by each member of the thesis committee and has been found to be satisfactory regarding content, English usage, format, citations, bibliographic style, and consistency, and is ready for submission to the College of Graduate Studies.

Dr. John Carlsten _____ (Signature) 12-4-98 Date

Approved for the Department of Physics

Dr. John Hermanson _____ (Signature) 12-4-98 Date

Approved for the College of Graduate Studies

Dr. Joseph J. Fedock _____ (Signature) 12/8/98 Date

STATEMENT OF PERMISSION TO USE

In presenting this thesis in partial fulfillment of the requirements for a doctoral degree at Montana State University – Bozeman, I agree that the Library shall make it available to borrowers under rules of the Library. I further agree that copying of this thesis is allowable only for scholarly purposes, consistent with "fair use" as prescribed in the U.S. Copyright law. Requests for extensive copying or reproduction of this thesis should be referred to University Microfilms International, 300 North Zeeb Road, Ann Arbor Michigan 48106, to whom I have granted "the exclusive right to reproduce and distribute my dissertation in and from microform along with the non-exclusive right to reproduce and distribute my abstract in any format in whole or in part."

Signature Gregory W. Switzer

Date Dec. 4, 1998

To Grandpa.

Thanks for encouraging me to

"Give college a try for awhile and see how you like it."

ACKNOWLEDGEMENTS

The first and foremost person I would like to thank is my advisor Dr. John Carlsten for the opportunity to do this work. His belief in my abilities were often stronger than my own.

I am very grateful for the help and training I received from Jim Wessel, Kevin Repasky and especially Meg Hall, whom I grew up with in the lab. I have also enjoyed working along side Jay Brasseur, Pete Sellin, Pete Roos, Lei Meng, Xiaoguang Sun, and a few fly-bys like Rand Swanson, Phil Battle and Phil Himmer. I owe my new machining skills to Norman Williams and my very existence to Margaret Jarrett, Jeannie Gunderson, Rose Waldon. I would also like to thank Larry Johnson and ILX Lightwave for their support and the opportunity to collaborate with a local industry.

I am indebted to NASA Goddard Space Flight Center for their support, collaboration and an unforgettable experience. I am especially thankful to Pam Millar, Jim Abshire, Gerald Soffen, and Don Cornwell (whom I aspire to become someday.) I thank Mike Krainak, Peter Heim, Gary Duerksen, John Rall, Anthony Martino, and Barry Coyle for all that they taught me in the short time I was in Maryland. I am most grateful to Mariusz "Marty" Miodek for his endless help with Labview and Jim Fitzgerald for his electronic wizardry and great stories.

Finally, I would like to thank Tami "Sue" Faircloth for never letting me give up.

TABLE OF CONTENTS

1. PROPOSED WATER VAPOR LIDAR INSTRUMENT FOR MARS

The need for Measuring the Atmospheric Water Vapor on Mars 1
The Basic Components of a Lidar System 3
Wavelength Tunable Sources as Candidates for the Laser Transmitter 4
Proposed Transmitter and Receiver for a Mini-Lidar Instrument 7

2. DEVELOPMENT OF THE EXTERNAL CAVITY DIODE LASER (ECDL) AT 935nm

2.1 Introduction and Motivation 10
Introducing the Laser Diode 10
Controlling the Output Wavelength with Optical Feedback 17

2.2 Theory of Laser Design and Construction 21
External Cavity Configuration 21
Facet Reflectivity of the Semiconductor Laser 23
Longitudinal Modes of the External Cavity 29
Wavelength Selection by the Diffraction Grating 35
Conditions for Single Mode Operation 37
Pivot Point for Continuous Tuning 42
Final Laser Design 49
Summary of Laser Design 54

2.3 Laser Performance 57
Single-Mode, Narrow Linewidth Output 57
Broad Wavelength Tuning Range 63
Continuous Wavelength Tuning 65
Fine Wavelength Tuning Range 68
Side-Mode Suppression Ratio 70
Power and Wavelength Stability 72
Beam Profile 75
Summary of Laser Performance 80

TABLE OF CONTENTS -- Continued

3. WATER VAPOR LIDAR TRANSMITTER USING THE EXTERNAL CAVITY DIODE LASER

3.1 Introduction and Motivation 82
Why the ECDL Alone is Not Enough 82

3.2 Amplify and Pulse using a Flared Semiconductor Amplifier 86
Coupling Light Into and Out of the Amplifier 88
CW Operation 91
Pulsed Operation 96

3.3 Overall Laser Transmitter Performance 103

4. MEASURING WATER VAPOR AT 935nm

4.1 Spectroscopy of the Optimal Water Vapor Absorption Line 104

4.2 Measuring Water Vapor at One Atmosphere Using the ECDL 109
Model the Absorption Line using HiTran Parameters 109
Measure the Absorption Line using the ECDL 112
Using the Laser to Monitor the Relative Humidity in the Lab 116

4.3 Measuring Water Vapor at Low Pressures Using the ECDL/Amplifier . 124
Model Absorption Line using HiTran Parameters 124
Measure the Absorption Line using the ECDL/Amplifier 127

5. USING LIDAR TO MEASURE ATMOSPHERIC WATER VAPOR CONCENTRATION FROM THE SURFACE OF MARS

5.1 The Atmosphere on Mars 135

5.2 How the Lidar will Measure Atmospheric Water Vapor Concentration 140
Backscatter Coefficients for the Atmosphere 142
Transmission Through the Atmosphere 146
Evaluating the Return Lidar Signal 150
Using DIAL to Measure Atmospheric Water Vapor Concentration .. 156

TABLE OF CONTENTS -- Continued

6. CONCLUSION 160

APPENDICES 162

A. Comparison of External Cavity Mode Spacing with Mode Shift While Tuning the Wavelength of the ECDL 163

B. Spatial modes in the output beam of the ECDL 166

C. Undergraduates and their projects 171
Tony Roberts 172
Amy Hyfield 175
Keith Ypma 178
Misty Bare 182
Kevin Flanagan 183

REFERENCES CITED 188

LIST OF TABLES

1.1	Candidate lasers for the water vapor lidar transmitter at 935nm	5
2.2.1	Output requirements of the external cavity diode laser	21
2.2.2	Optical path length of the 935nm external cavity	30
2.2.3	Reflectivity's of optical surfaces of the external cavity	33
2.2.4	Specialty components used in the 935nm ECDL	54
2.3.1	Summary of laser requirements and actual performance	81
3.3.1	Performance summary of the overall 935nm laser transmitter	103
4.2.1	Atmospheric conditions inside the lab at NASA/GSFC	110
4.2.2	Sources for experimental error and their worse-case values	115
4.3.1	Atmospheric conditions inside the low pressure optical cell	126
5.2.1	Atmospheric composition of Mars by volume	144
5.2.2	Typical values for the optical parameters of the lidar receiver	151
C.1	Center wavelength of a few acetylene absorption lines	180

LIST OF FIGURES

Figure		Page
1.1	The basic components of a lidar system	3
1.2	Molecular resonance will absorb laser light	4
1.3	Artists conception of proposed Mars Lander	7
1.4	Schematic of mini-lidar system	8
2.1.1	Structure of the 935nm semiconductor laser	12
2.1.2	Energy band diagram for a semiconductor laser	13
2.1.3	Photo of the 935nm laser diode	15
2.1.4	Multimode output of 935nm diode laser	16
2.1.5	External cavity configurations	17
2.1.6	Interaction between the facet mode, gain and loss profiles	18
2.1.7	Spectral output of the 935nm Fabry-Perot laser diode	19
2.2.1	The Littman-Metcalf optical configuration of the 935mn ECDL	22
2.2.2	Longitudinal facet modes of the diode laser	24
2.2.3	Spectral output of 935nm diode laser with and without AR coating	27
2.2.4	A Single Angled Facet (SAF) semiconductor laser	28
2.2.5	The optical path lengths of external cavity	29
2.2.6	1st order diffraction efficiency for the 1600 lines/mm grating	31

LIST OF FIGURES -- Continued

2.2.7	Incident and diffracted angles of the external cavity	32
2.2.8	Calculated longitudinal modes of the external cavity	35
2.2.9	Calculated spectral dispersion of 1600lines/mm grating	37
2.2.10	Spectral overlap of the longitudinal modes with the grating dispersion	38
2.2.11	Spectral overlap after reducing cavity length by 30%	40
2.2.12	Spectral overlap after increasing cavity length by 30%	41
2.2.13	Spectral overlap showing how a mode hop occurs while tuning	43
2.2.14	Mode hops cause a discontinuous step in the output wavelength	44
2.2.15	The three principle planes of the external cavity	46
2.2.16	Calculated effect of mis-locating the pivot point by 18.7μm	48
2.2.17	Mechanical drawing of 935nm ECDL	49
2.2.18	Photo of 935nm ECDL after assembly	53
2.3.1	Experimental setup for measuring linewidth of ECDL using Fabry-Perot	58
2.3.2	21.5MHz linewidth of 935nm ECDL measured on Fabry-Perot	59
2.3.3	Experimental setup for a heterodyne linewidth measurement	60
2.3.4	Heterodyne linewidth of 170kHz	61
2.3.5	Photograph of the two ECDL's used to measure the heterodyne linewidth	63
2.3.6	Broad wavelength tuning range on 935nm ECDL	64

LIST OF FIGURES -- Continued

2.3.7	Near continuous wavelength tuning of the 935nm ECDL over 10nm	66
2.3.8	Identifying "spatial mode hops" from longitudinal mode hops	67
2.3.9	Scanning wavelength of ECDL electronically using a PZT	69
2.3.10	Side-mode suppression ratio as a function of wavelength	71
2.3.11	Power versus current curve for the 935nm ECDL	73
2.3.12	Power and wavelength stability over 10 hours	74
2.3.13	Far field beam profile of 935nm Fabry-Perot laser diode	76
2.3.14	Photo of collimated beam using the f = 4.5mm, 0.55NA aspheric lens	77
2.3.15	Output polarization of the 935nm ECDL	79
3.1.1	Frequency chirp caused by pulsing the drive current to the ECDL	84
3.2.1	Injecting 935nm ECDL output into flared semiconductor amplifier	86
3.2.2	Photo of the flared semiconductor amplifier	88
3.2.3	Optical schematic for the semiconductor flared amplifier	89
3.2.4	Schematic for seeding the optical amplifier with the 935nm ECDL	90
3.2.5	Spectral output of seeded amplifier	92
3.2.6	PI curve of the lidar transmitter output	93
3.2.7	Single pass gain curves for the flared amplifier	95
3.2.8	Output pulse from the semiconductor amplifier	98

LIST OF FIGURES -- Continued

3.2.9	Pulsed output spectrum of the flared amplifier with no seed laser	99
3.2.10	Chirp-free linewidth of output from pulsed, seeded amplifier	100
3.2.11	Frequency chirp seen using the 935.68nm water vapor absorption line	101
4.1.1	Absorption spectra of atmospheric water vapor at 1atm, 23°C	105
4.1.2	Absorption spectrum of the 935nm region at 1atm, 23°C	106
4.1.3	The 935.68nm absorption line 4.56Torr and -30^{0}C	108
4.2.1	Set up to measure the water vapor in the air in the lab	112
4.2.2	Measured and predicted absorption line at 1atm	114
4.2.3	Method for making on-line/off-line absorption measurements	117
4.2.4	Relative humidity of the air in the lab measured by the 935nm ECDL	121
4.2.5	Commercially available relative humidity meters	122
4.3.1	Photo of low pressure, multi-pass optical cell	125
4.3.2	Set up to measure the water vapor in the cell at low pressures	128
4.3.3	Measured and predicted absorption line at 5Torr	129
4.3.4	Scans made using ECDL/amplifier vs. ECDL only	131
4.3.5	Transmission at 935.68nm as a function of path length	133
4.3.6	Absorption linewidth as a function of pressure	134
5.1.1	Temperature and pressure profiles at the Viking 2 Lander site	136

LIST OF FIGURES -- Continued

5.1.2	Vertical profile of water vapor density at the Viking Lander 2 site	137
5.1.3	Atmospheric water vapor concentration on Mars and Earth	138
5.2.1	Predicted backscatter of the lidar signal	145
5.2.2	Predicted transmission of the lidar signal	147
5.2.3	Predicted transmission of the lidar signal due to absorption of water vapor	149
5.2.4	Schematic of the bread board lidar receiver	150
5.2.5	Geometrical overlap of transmitter beam with receiver FOV	152
5.2.6	Predicted number of photoelectron counts from the lidar receiver	154
5.2.7	Vertical profile of the water vapor density "measured" by our lidar	158
B.1	Spatial modes of the gain guided, 935nm laser diode	167
B.2	Frequency output of the lowest and higher order spatial modes	168
B.3	Spatial profile of the lowest and higher order spatial modes	169
C.1	Improving the transmission peak of a scanning, high finesse cavity	173
C.2	Stabilizing the frequency of a 780nm ECDL to a Fabry-Perot	174
C.3	Experimental setup for high resolution spectroscopy of acetylene	176
C.4	A high resolution plot of the P9 absorption line of C_2H_2	177
C.5	Acetylene absorption cell used as a calibration source for OSA's	179
C.6	The P - 11 absorption line measured with the optical spectrum analyzer ...	181
C.7	FOS 79870 8-channel fiber optic source developed with ILX Lightwave	182

LIST OF FIGURES -- Continued

C.8 Mechanical drawing laser diode beam profiler 184

C.9 Beam profile of the output from 935nm laser diode 185

ABSTRACT

This dissertation investigates the feasibility of a novel, low power miniature lidar intended to measure the vertical distribution of atmospheric water vapor on Mars. This instrument could provide valuable information crucial to understanding the past and present climate of Mars. The emphasis is to develop a compact, efficient, all-semiconductor laser transmitter and demonstrate its ability to measure water vapor at high and low atmospheric pressures.

Current lidar systems are too large, complicated and require too much electrical power to be considered for a space-born mission. Recent advancements in high power semiconductor lasers and highly sensitive semiconductor detectors have, for the first time, made it possible to develop a small, rugged, lidar system that could meet the strict requirements for a future Mars Lander mission.

The laser transmitter consists of a wavelength tunable, single mode, narrow linewidth external cavity diode laser whose CW output is amplified and pulsed using a flared semiconductor amplifier. The pulsed output of the device must be able to scan its wavelength across the strongly absorbing $\lambda = 935.68$nm water vapor absorption line without frequency chirp. The desired output of the external cavity diode laser was modeled based on its mechanical and optical design. The laser was designed, machined, assembled and its output was characterized. The laser was used to optically seed a flared semiconductor amplifier whose drive current was pulsed. The combined transmitter emitted 0.36μJ pulses that were free from frequency chirp.

The pulsed transmitter beam scanned the water vapor absorption line at low pressures using a multipass optical cell. The profile of the measured absorption line agrees with the profile predicted using HiTran '96 atmospheric database to within a few percent. The maximum altitude the lidar could measure during sunlit conditions on Mars was estimated based on the laser transmitter output and optical receiver parameters of the current bread board system. A maximum altitude of 1.3km for measuring water vapor and 3.2km for aerosols was theoretically predicted using estimates of the atmospheric conditions from previous missions to Mars. Simple improvements would enable the lidar system to measure the dynamics of the water vapor up to 5km.

CHAPTER 1

PROPOSED WATER VAPOR LIDAR INSTRUMENT FOR MARS

The Need for Measuring the Atmospheric Water Vapor on Mars

Since people began to speculate about what Mars is like, water has been the central issue. Our neighboring planet may be more similar to Earth than we realize. Initial observations indicated a cold, dry planet with little geographical or biological interest. Then in November of 1971, the Mariner 9 fly-by revealed large canals cut by rivers, flood planes and huge volcanoes that revived the interest in the biological potential of Mars. Today, it is generally accepted that 3.5-3.8 billion years ago, Mars once had a water-rich past just like that of Earth and, therefore, had a high possibility for supporting life. The big question is, where is the water now? One hypothesis suggests Mars suffered large impacts with asteroids which are able to create a hot vapor plume that expands outward with sufficient energy to blow off all or part of the overlying atmosphere [1]. Loss of the atmosphere caused the planet to cool and freeze the remaining water below the crust. This hypothesis cannot be tested until we learn more about how much water there is on the planet and its distribution.

In the remaining atmosphere, water is transported almost entirely by dust. As morning temperatures rise, ice stored in the crust sublimes and forms water vapor that

can attach itself to dust particles. Blowing dust transports the water vapor until the temperatures fall, forming ice which then settles onto the surface. Other than observing the formation and retreat of the polar ice caps containing CO_2 ice and water ice, little is known about the actual origin, dynamics or final destination of the water vapor.

Fortunately, much information about Mars is available thanks to detailed studies of Mars using observations from Earth, photos from the fly-by Mariner spacecraft (1965-1971), orbiter and lander information from the Viking missions (1976), and recently, Mars Pathfinder (1997) and Mars Global Surveyor (1998). These successful programs have provided us with a wealth of knowledge about the planet such as its global geography, soil and atmospheric content, and climatic season and dust storms. Still, little is known about the dynamical processes of the lower atmosphere. Dust, carbon dioxide and water vapor are the three primary atmospheric constituents which play a major role in Martian atmosphere. The dynamical interplay between dust, CO_2 and water vapor determines the climate on Mars almost exclusively. An understanding of these dynamical processes can not only provide information about the current climate on Mars, but can also tell us something about its past, rich climate and possibly what caused it to change. Frequently measured vertical profiles are needed at several locations on the surface of the planet in order to track the dynamics of the water vapor. The water vapor lidar instrument proposed for this project could provide us with this information, crucial to understanding the past and present climate on Mars and the evolution of the planet to its current state.

The Basic Components of a Lidar System

A "light identification, detection, and ranging" or lidar system provides a way to optically probe the atmosphere through absorption and elastic scattering of light. A lidar system consists of two basic components: a laser transmitter and optical receiver (Fig. 1.1).

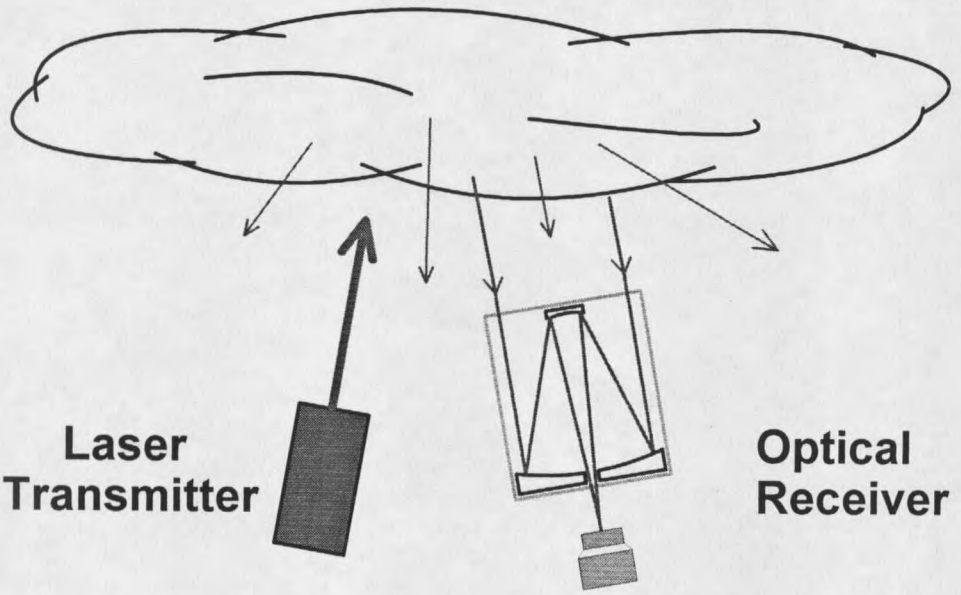


Figure 1.1. The basic components of a lidar system.

Short, single pulses of light from the laser are sent vertically into the atmosphere and scattered elastically off molecules and aerosols. "Aerosols" is a general term used for atmospheric particulates such as dust, ice crystals, fog, haze, and clouds. A fraction of light is scattered back towards the optical receiver where it is detected by photon-counting detectors. Ambient light is filtered out optically by placing a narrow bandpass filter in front of the detector whose center wavelength matches that of the laser beam. The time between the departure from an individual laser pulse and the arrival of the

scattered return can be directly related, through the speed of light, to the range at which the scattering occurred. In addition, the laser wavelength can be tuned to a vibration/rotation resonance of a particular gas molecule, such as H_2O, causing the received light to be preferentially absorbed (Fig. 1.2).

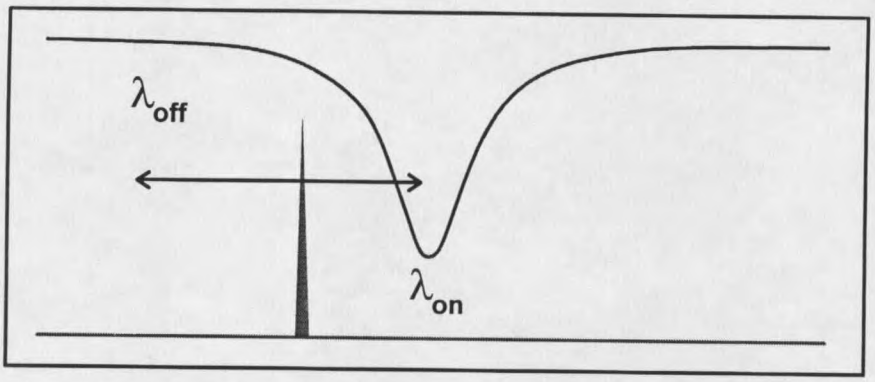


Figure 1.2. Molecular resonance will partially absorb the laser light as a function of wavelength.

The ratio of the return light detected while the wavelength of the laser is on the center of the molecular resonance (λ_{on}) to the off-resonance wavelength (λ_{off}) leads to a direct measurement of the absorption caused by the water molecule. The known absorption parameters for the selected resonance can be applied to the absorption to determine the molecular concentration for each range. The result is a range-resolved, vertical profile of atmospheric water vapor concentration. This technique is often called "differential absorption lidar" or DIAL.

Wavelength Tunable Sources as Candidates for the Laser Transmitter

A DIAL lidar instrument requires that the output of the laser transmitter be single frequency and have a narrow linewidth that can be scanned across the water vapor

absorption line. The output wavelength of the laser transmitter must scan about λ = 935.68nm where a strong water vapor absorption line was selected (discussed further in section 4.1). To be considered for a space-based mission such as flying to the surface of Mars, the laser must be small, lightweight and energy efficient. Table 1.1 below lists several, commercially available, tunable lasers which may be considered for this project.

Table 1.1. Candidate lasers for the water vapor lidar transmitter at 935nm.

Laser	Gain Medium	Pumping Method	Energy	Size
Free Electron	High energy electrons in alternating **B** field	High voltage, permanent magnets	10μJ	huge
Dye	Jet stream of organic dye in solvent	Nd:YAG, flashlamp Ar Ion for CW	400J	large
Titanium Sapphire	Ti:Al_2O_3 crystal	Nd:YAG, Nd:YLF, flashlamp	60μJ	large
Chromium LiSAF	LiSAF crystal with Cr^{3+} sat. absorber	Flashlamp, laser diode Ar Ion	100mJ	large
Color Center	LiF with F_2^+ center center lifetime = days	Nd:YAG, Ar Ion	0.6μJ	large
Nd:YAG Micro-chip 946nm emission	1.8%Nd in YAG with Cr^{4+}sat. absorber	808nm fiber coupled laser diode	6mJ	tiny
Nd Fiber Laser	0.07% Nd co-doped with Ge optical fiber	808nm fiber coupled laser diode	0.16μJ	tiny
Semiconductor ECDL + amplifier	Quantum well InGaAs in AlGaAs	Electrical current DC and pulsed	0.36μJ	small

The laser transmitter must be very small, lightweight and consume as little electrical power as possible to be consider for a space mission. The laser must also be

rugged and have maintenance-free lifetimes of 2 to 4 years. The first five lasers require a second laser to pump their gain medium, have a poor wall-plug efficiency, typically occupy an entire optical table and are high in maintenance [2]. Although their high output pulse energies are attractive for lidar, they are not an ideal tunable laser source for space flight. The Nd:YAG micro-chip laser was specifically developed by MIT/Lincoln Labs in collaboration with NASA/GSFC as a source for a small water vapor lidar system. Unfortunately, its emission wavelength is not tunable and centered near the weaker 944nm water vapor absorption line. The Nd doped optical fiber laser is simple, small, efficient, robust and is a very promising lidar transmitter. However, it may be limited to low output powers by the 3-level transition of Nd at 935nm. Finally, semiconductor lasers require only electrical current as their pump source, are highly efficient, small and have long lifetimes. Semiconductor lasers are the only type of lasers that meet all of the requirements for a space-based mission, but would they be powerful enough for an atmospheric lidar system?

Until very recently, only large, high power pulsed lasers were considered capable of transmitting enough power (10-1000mJ per pulse) for atmospheric lidar. However, with the development of high quantum efficiency photon counting detectors and very narrow band filters to reject most of the ambient light, less optical power from the transmitter is needed. In addition, the recent advancements in high power semiconductor devices are opening the possibilities for using laser diodes as the source for lidar transmitters. For this reason, the development of an all-semiconductor laser transmitter was chosen in order to demonstrate the feasibility of measuring low concentration,

atmospheric water vapor remotely. Not only are the semiconductor lasers ideal for a future space born lidar, but they are nicely suited for demonstrating this proof of concept because they are the least expensive and quickest to obtain thanks to their popular commercial uses.

Proposed Transmitter and Receiver for a Mini-Lidar Instrument

The Mars Lander instrument will be a small spacecraft that will land on the surface of Mars much like the two Viking landers in 1976 and, more recently, the Mars Pathfinder in 1997 (Fig. 1.3).

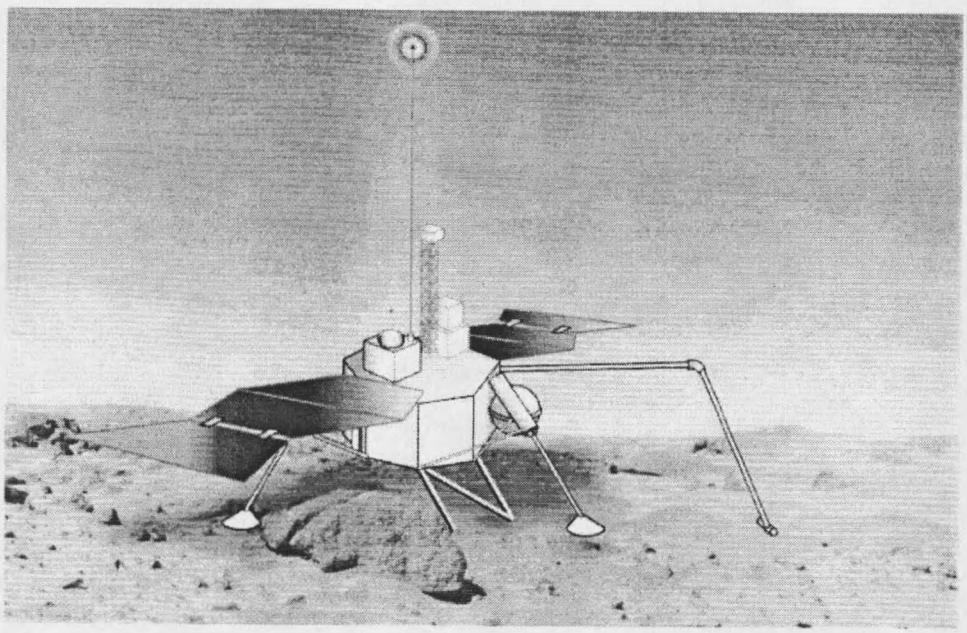


Figure 1.3. Artists conception of the proposed Mars Lander containing the water vapor lidar instrument.

The lander will contain many instruments to measure the local dusty, dry atmosphere. One of the instruments will be the water vapor lidar instrument proposed by NASA/GSFC and being developed as part of this thesis project [3]. The lidar instrument

alone must be very small, have a mass less than 2kg, and operate on less than 2W of electrical power. An all-semiconductor laser transmitter is the only way to meet the strict size, mass and power requirements of the instrument, and became the focus for this project. Figure 1.4 below is a schematic of the mini-lidar system proposed for a Mars Lander mission [4]

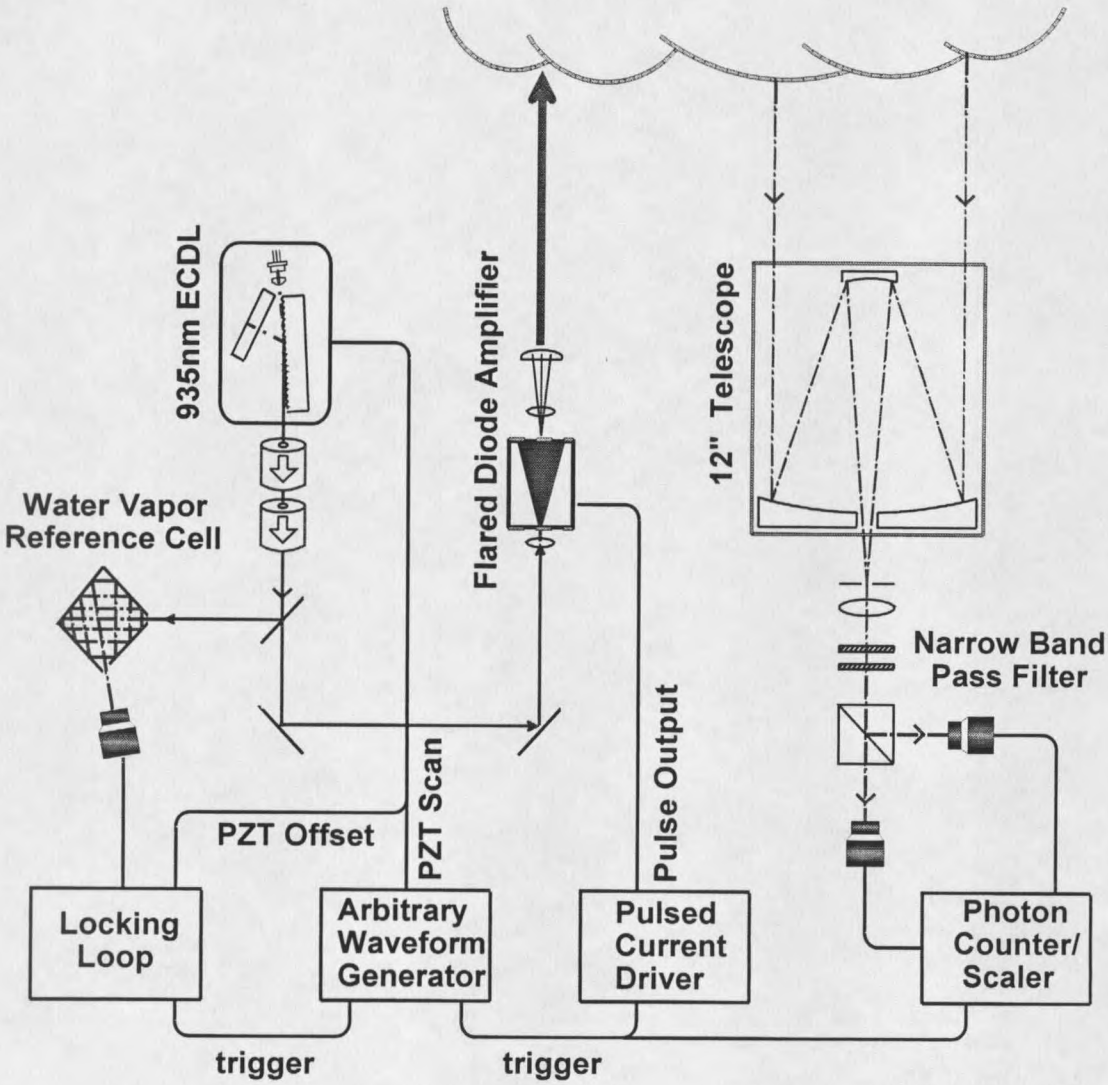


Figure 1.4. Schematic of mini-lidar system proposed for a Mars Lander mission.

The scope of this project is the development of the all-semiconductor laser transmitter for this proposed mini-lidar system. This transmitter consists of two basic components: a master oscillator (labeled 935nm ECDL in Fig. 1.5) and a power amplifier (labeled Flared Diode Amp in Fig. 1.5). The master oscillator is a CW, wavelength-tunable, external cavity diode laser discussed in detail in chapter 2. The power amplifier is a pulsed, flared, semiconductor amplifier discussed in detail in chapter 3. The master oscillator will tune its wavelength on and off the water vapor line while the power amplifier will optically amplify and pulse this output for time-of-flight range information. Chapter 4 will demonstrate that the pulsed laser transmitter can accurately measure the 935.68nm water vapor absorption line at low pressures similar to atmospheric pressures found on Mars. Finally, chapter 5 describes how the water vapor concentration can be determined from the actual return lidar signal using the DIAL technique.

CHAPTER 2

DEVELOPMENT OF THE EXTERNAL CAVITY DIODE LASER (ECDL) AT 935 nm

2.1 Introduction and Motivation

The transmitter for the proposed Mars water vapor lidar system consists entirely of semiconductor devices because of their small size and unmatched electrical to optical efficiency. A brief history of these devices is presented, followed by a description of their structure and how their unique properties can be used to develop a small, wavelength tunable source. This chapter focuses on the development of the master oscillator of the proposed lidar transmitter; the external cavity diode laser.

Introducing the Laser Diode

In the early 1960's, semiconductor device researchers were aware of the fact that p-n junctions could emit light. Electrons and holes could be injected into the p-n junction by applying a forward bias to the device resulting in recombination radiation, emitting light. Emission from these first light emitting diodes (LED's) was weak and few considered their possibility as lasers. Then in 1962, Rediker's Lincoln Laboratory group reported using a simple Zn-diffused GaAs p-n junction to emit infrared (IR) radiation and

transmit signals over long distances. In a very real sense, optoelectronics had begun. If the recombination radiation from a direct-gap p-n junction could be used to broadcast a signal that could be detected over long distances, then the light must be substantial. This provided sufficient interest to make the light coherent [5]. In the fall of 1962, four different groups were successful in demonstrating the first laser diodes. These simple devices were made from direct-gap GaAs or GaAsP material with polished front and rear facets (used to create a laser cavity), were pulse-operated and cooled to liquid nitrogen temperatures [6,7,8,9]. By 1970, more complicated double-heterostructure GaAs-Al_x $Ga_{1-x}As$ devices were able to operate continuously at room temperature of 300K [10]. Then in 1977, the quantum well device appeared reducing the size of the gain region which improved the density of states and its performance [11,12].

Today, the semiconductor laser (or laser diode) remains the smallest, least expensive, most efficient and reliable laser source known. Over 99% of all lasers used in the world today are semiconductor lasers only 36 years after their discovery. Their commercial uses span a broad range from telecommunications to compact disc players to grocery store scanners. While their size and electrical efficiency are also ideal for space and planetary missions, they have only recently been considered as sources for lidars and altimeters with the development of high power semiconductor amplifiers. The challenge of this project is to determine if a water vapor lidar intended for Mars whose source consists entirely of semiconductor laser devices would actually work.

The basic semiconductor laser is a forward biased p-n junction with cleaved ends or facets (Fig. 2.1.1).

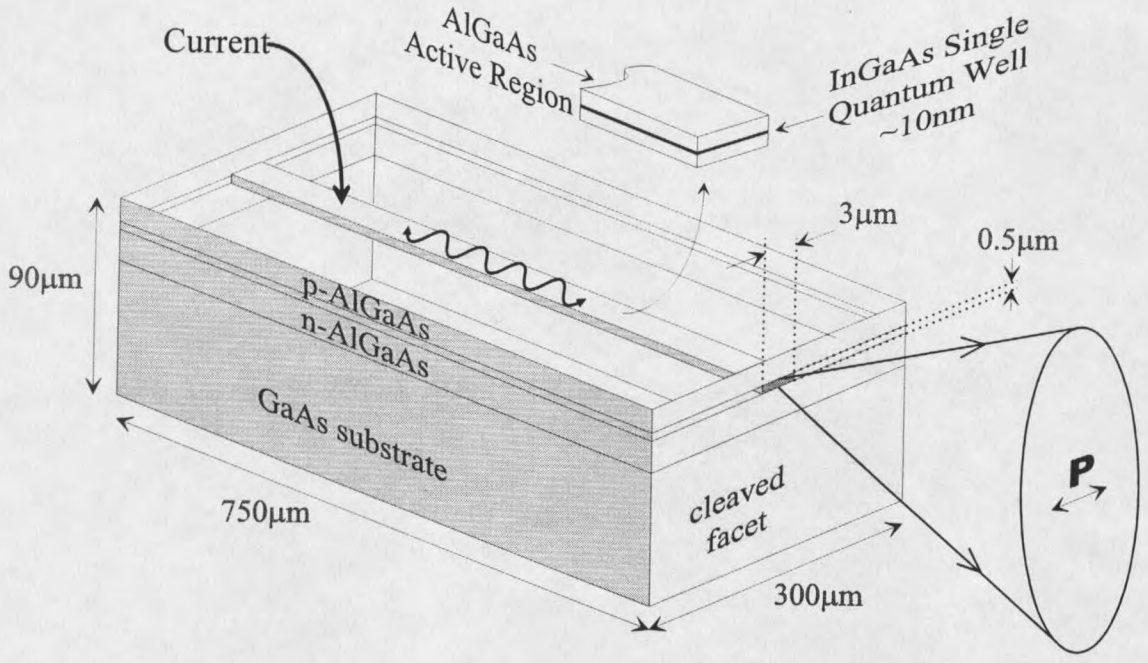


Figure 2.1.1. Structure of the 935nm semiconductor laser. Dimensions were provided by the manufacturer [13].

The facets act as partially reflecting mirrors and form the laser resonator. This epitaxial design consists of a single InGaAs quantum well active region surrounded by AlGaAs confining and cladding layers [14]. Light is generated inside the tightly confined active region sandwiched between the p and n type regions. The AlGaAs regions surrounding the active region have a slightly larger band gap energy which helps guide the light inside the quantum-well InGaAs region. This structure is called a double-heterostructure because it optimizes the confinement of both the charge carriers and the photons inside the active region. Light leaving the small, asymmetric waveguide diverges quickly and is polarized along the 3μm axis of the waveguide. The n type AlGaAs region just below the waveguide provides extra free electrons to the conduction band and the p-type AlGaAs region just above the waveguide provides extra free electron vacancies, known as holes,

to the valance bands. When the junction is forward biased (usually 1.5V) the Fermi energy level corresponding to the n-type region rises above the conduction band into the active region providing excess electrons that can radiatively decay via stimulated or spontaneous emission (Fig. 2.1.2).

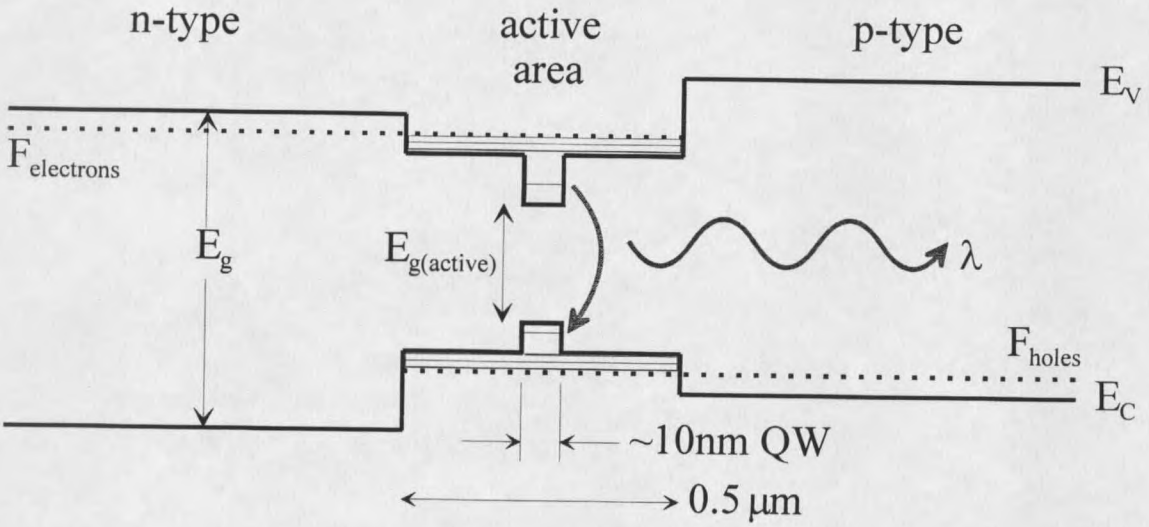


Figure 2.1.2. Energy band diagram for a semiconductor laser under forward bias. Fermi levels for the electrons and holes shown by the broken lines

A similar effect provides excess holes in the active region. This leads to a population inversion needed for amplification of the radiation. Electrons are continuously pumped back into the conduction band by a DC current (usually 50mA). The central quantum well, labeled "QW" above, further confines the electrons and tends to quantize the transition in a way that reduces the threshold current needed for stimulated emission. This basic structure of a semiconductor lasers allows for unique and important properties that are not found in any other type of lasers.

First, the materials that make up the semiconductor laser roughly determine the emission wavelength which can provide flexibility in available wavelengths. For

instance, InGaAs was chosen for the quantum well in the active region because, it has a bandgap energy of $E_{g(active)} = 1.22$ eV at 300K [15]. A radiative transition will emit a photon whose wavelength is:

$$\lambda = \frac{hc}{E_{g(active)}} \rightarrow 1010nm \qquad 2.1.1$$

where h is Plank's constant and c is the speed of light. However, by adjusting the depth of the quantum well (the thickness of the InGaAs layer), the energy gap between the fundamental states of the transition can be increased until the emission is reduced to the desired wavelength of 935nm. A wide variety of wavelengths are possible from 514nm to 4,200nm by choosing among several different materials providing a wavelength flexibility not found in other types of lasers [16,17]

Second, the optical gain found in the active region of the laser is extremely high, in the range of hundreds of cm^{-1}. This is orders of magnitude greater than any other type of laser. This is why the semiconductor laser can be made as small as a grain of salt, typically 350 -1000μm long [15]. The small size and mass of these lasers make them ideal for spacecraft. The devices are so small, that they are usually soldered to a larger, gold coated heat sink that also supplies the electric contacts to the semiconductor diode using tiny bond wires. The 935nm laser diode for this project was mounted in an industry standard 9mm diameter "can" shown below in figure 2.1.3. For reference, the large pin on the left contacting the bond wires is 0.020" (510μm) in diameter.

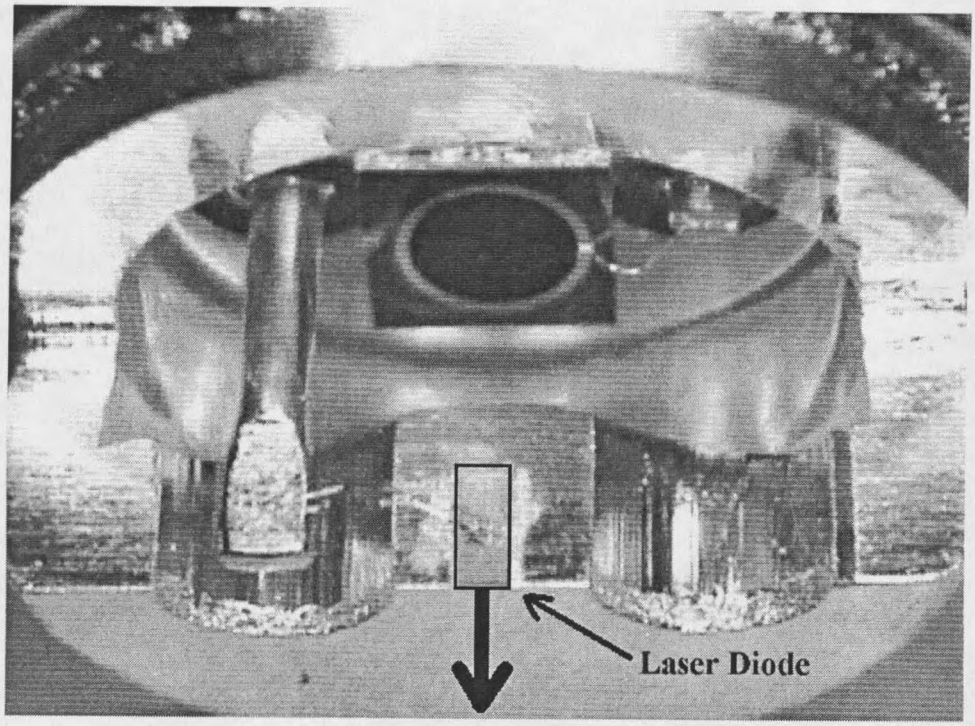


Figure 2.1.3. Photo of the 935nm laser diode mounted in a 9mm "can". This image is magnified 20 times the actual size.

Finally, optical transitions can take place among the many energy levels, or bands, inside the active region which provides gain over a large wide spectral bandwidth from 10 to 50nm wide. Only one or two transitions are allowed among the well defined states inside the quantum well, which will pull the emission to a longer, desired wavelength. The broad distribution of gain is important for developing a wavelength tunable source such as the external cavity laser.

Unfortunately, the spectral output of the semiconductor lasers is seldom monochromatic like you would expect from other lasers. Cavity resonances occur when an integral number of half wavelengths fall between the two parallel, partial-reflecting

end facets of the laser diode. This generates many longitudinal modes in the output spectrum (Fig. 2.1.4).

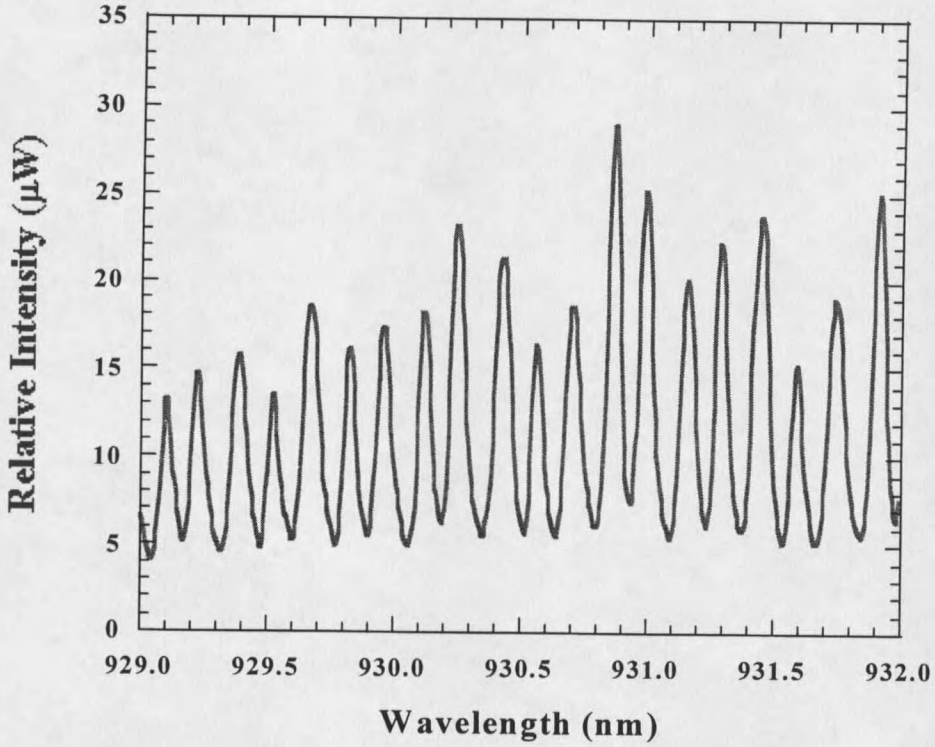


Figure 2.1.4. Multimode output of 935nm diode laser.

For this reason, this particular laser structure is often referred to as a "Fabry-Perot" laser diode. Such a multimode output is unacceptable for the numerous applications where narrow, single mode lasers are needed, such as spectroscopy. As a result, commercially available semiconductor lasers are limited to applications where only the intensity is important such as in CD players, grocery store scanners, and laser pointers.

Controlling the Output Wavelength with Optical Feedback

An elegant way to eliminate the unwanted multimode output of the semiconductor laser and enhance its performance is to place the device inside a wavelength-selective optical cavity. This forms a cavity that is external to the device, giving the configuration the name "external cavity diode laser". The semiconductor device is used purely as a gain medium for the larger external cavity, taking full advantage of its high amplification over a broad spectral range. Two popular optical configurations for external cavity diode lasers are shown below (Fig. 2.1.5).

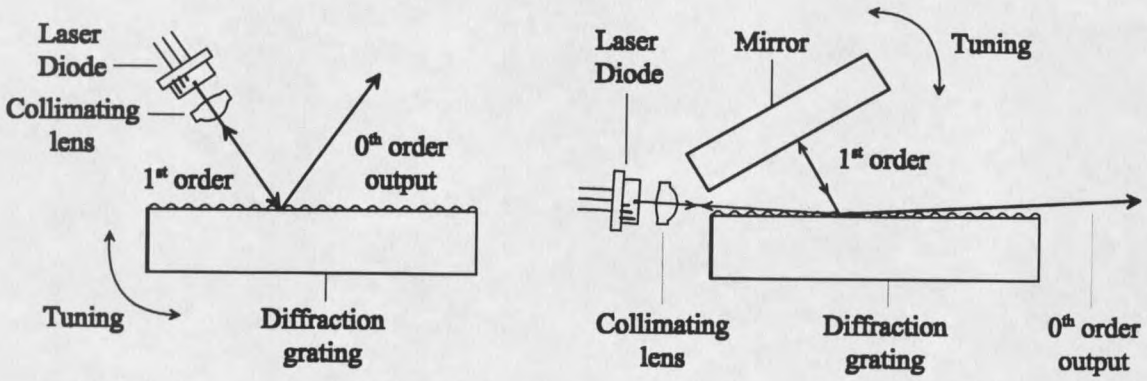


Figure 2.1.5. Littrow configuration on the left tunes the wavelength by tilting a diffraction grating while the Littman-Metcalf configuration on the right tunes the wavelength by tilting a mirror, leaving the angle of the output beam unchanged.

Originally, both the Littrow and Littman-Metcalf configurations were developed for use in dye lasers for wavelength tuning of the emission of the laser-pumped dye [19,20] Later it was discovered that a tiny laser diode could replace the dye cell and pump laser in either cavity. In both configurations the rear facet of the laser diode serves as one of the end mirrors of the cavity and usually receives a high reflective coating of $R \geq 0.95$. In either configuration, the diffraction grating separates the wavelengths spatially

allowing only one wavelength to be reflected back into the laser medium where it can be amplified. This reduces the loss at all wavelengths except the one chosen by the angle of the grating, or mirror in the Littman-Metcalf configuration. When the dip on the loss curve due to the grating overlaps with a facet mode of the laser diode, the output will be single mode with all other modes being suppressed (Fig. 2.1.6)

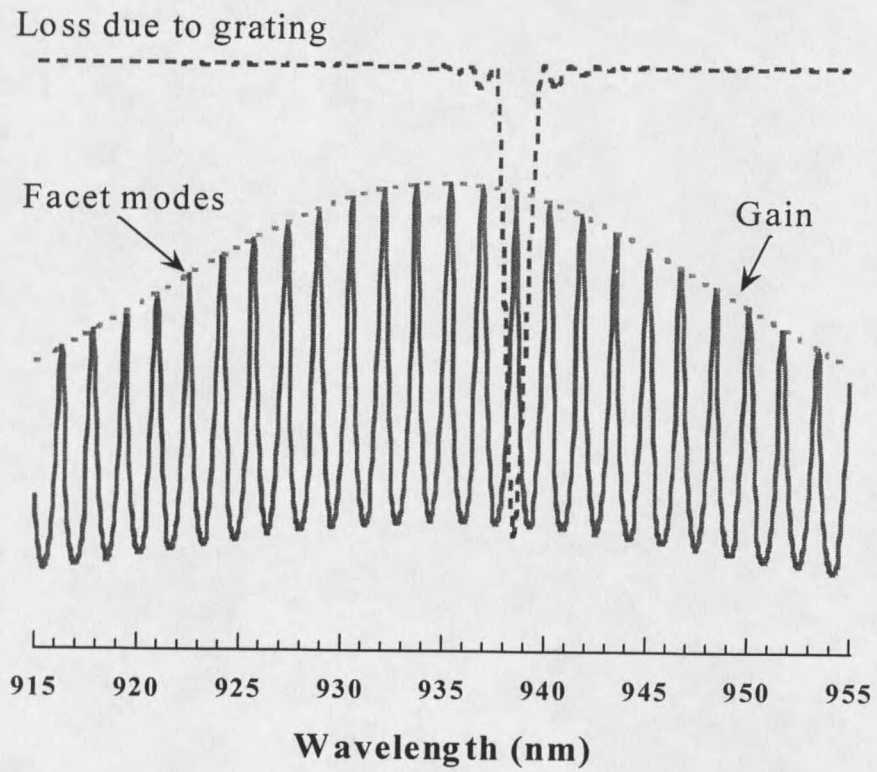


Figure 2.1.6. Interaction between the facet mode, gain and loss profiles. Actual facet modes spacing and linewidth of loss due to grating are much smaller than shown above.

Suppose the grating is tilted to a desired wavelength that doesn't happen to overlap one of the facet modes. The temperature of the diode can then be raised or lowered using a thermoelectric cooler to slide the facet mode profile over slightly. Changing the temperature, and to a less extent the injection current, will cause the length

between the facets to expand or contract, shifting the cavity resonances. In this way, an external cavity diode laser can be set to any wavelength within the gain bandwidth of the diode.

Below is an actual spectrum taken from the output from an external cavity diode laser on an optical spectrum analyzer (Fig. 2.1.7).

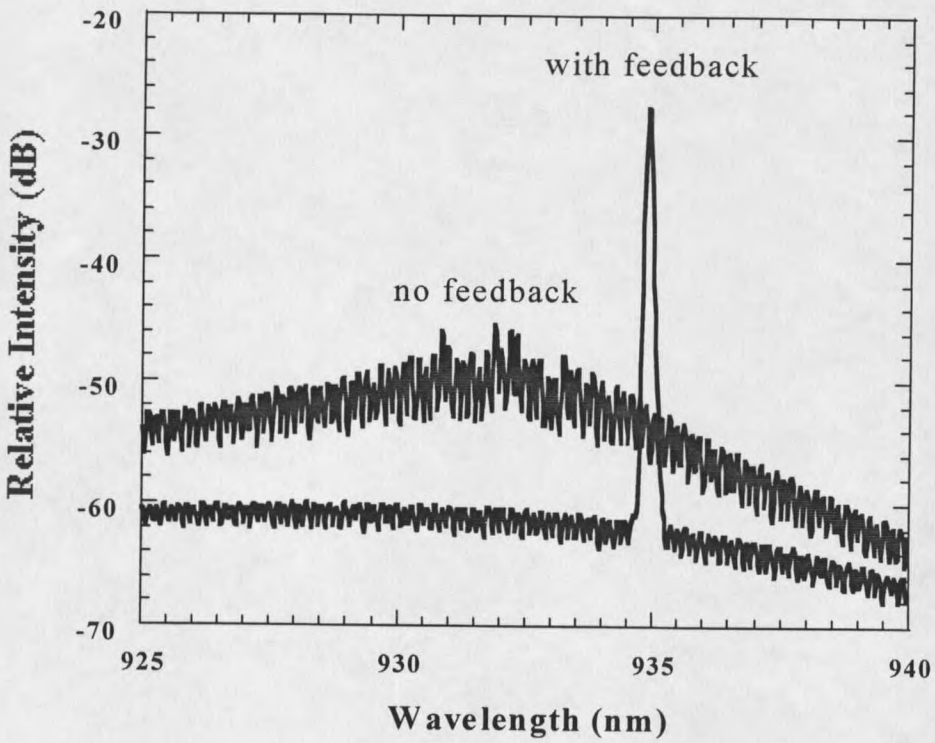


Figure 2.1.7. Spectral output of the 935nm Fabry-Perot laser diode with and without feedback from an external optical cavity.

The laser diode used to generate this spectrum has a rear facet reflectivity of 95% and a front facet reflectivity of 10%, which is standard for off-the-shelf commercial diodes. Notice how the other modes are suppressed when the optical feedback is provided by the diffraction grating. This is the basic information needed to understand how the output of

a semiconductor laser can be made single mode and its wavelength tunable by placing it in an external cavity. The next few sections will discuss the details of the design, construction, and performance of the 935nm external cavity diode laser used for the water vapor lidar transmitter for this project.

2.2 Theory of Laser Design and Construction

The output requirements for the CW, tunable external cavity diode laser (ECDL) to be used as the master oscillator for the proposed miniature water vapor lidar transmitter at 935nm are listed below:

Table 2.2.1. Output requirements of the external cavity diode laser.

Output parameter	Required Performance
CW Output Power	10mW
Wavelength	935.7nm
Continuous λ scan	30pm (10GHz)
Mode suppression ratio	30dB
Spectral linewidth	< 25MHz single mode
Beam profile	3:1 aspect ratio, $TEM_{0,0}$
Polarization	linear 100:1

The challenge was to develop a tunable, single-frequency, narrow-linewidth optical source from a commercially available semiconductor laser. Section 2.1 suggested a simple way of improving the output wavelength by providing optical feedback to the laser. Providing truly single mode, narrow linewidth output whose wavelength can be accurately and continuously tuned across a specific absorption line for spectroscopic applications is particularly demanding. Many issues involving the laser diode and the external optical cavity need to be carefully considered to achieve this goal and meet the requirements listed above. These issues will now be discussed in detail.

Optical Configuration of the External Cavity

The Littman-Metcalf configuration briefly introduced in section 2.1 was chosen for the design of the 935nm external cavity diode laser (Fig. 2.2.1).

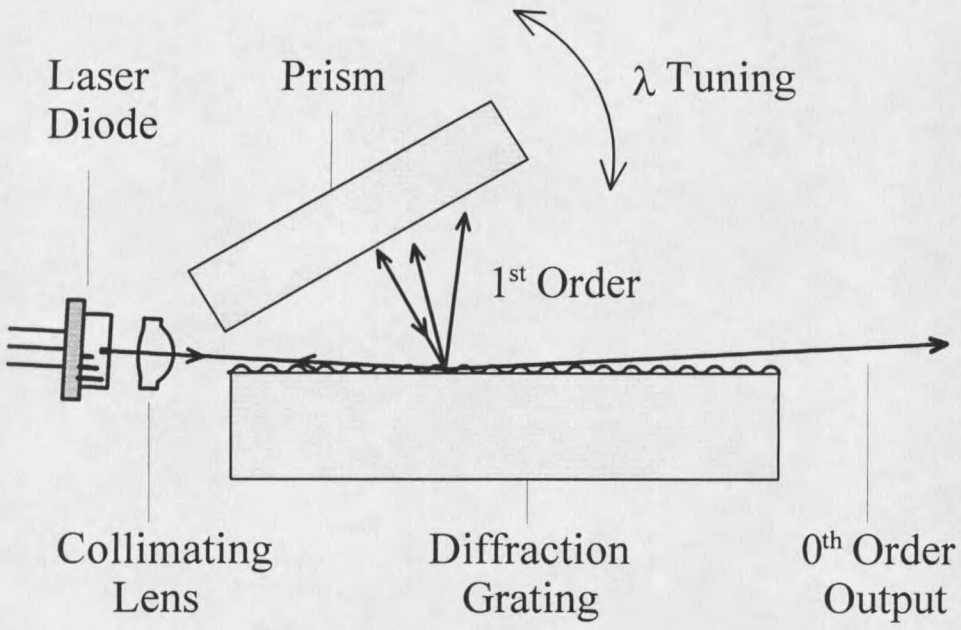


Figure 2.2.1. The Littman-Metcalf optical configuration of the 935mn ECDL.

The highly divergent light emitted from the small aperture of the laser diode is collimated using an aspheric collimating lens with a high numerical aperture. The collimated beam is projected onto a 1600 lines/mm holographic diffraction grating at a grazing incidence of 87^{o} from the grating normal. Approximately 35% of the beam intensity is diffracted off of the grating into the 1^{st} order separating the various wavelengths spatially by slightly different angles. A beam-folding prism held at a specific angle is used to select a particular wavelength of the 1^{st} order light and reflect it back towards the laser diode where it can be further amplified. All other wavelengths (shown by single-ended arrows) are quickly suppressed and only the selected wavelength (shown by the double-ended arrow) resonates inside the cavity. Approximately 50% of this single wavelength light is coupled out of the cavity by reflecting off of the grating into the 0^{th} order. The output wavelength can then be tuned by changing the angle of the prism in the plane of the

cavity. The remaining 15% of the intensity is lost to another 1st order diffraction from the beam reflected off the prism on its way back to the laser diode. This 1st order diffraction from the feedback beam exits the external cavity. Absorption of the aluminum coated holographic diffraction grating provides only a small percentage of the loss.

The Littman-Metcalf configuration has three important advantages over the Littrow configuration, also introduced in section 2.1. First, the output beam remains fixed as the wavelength is changed. In the Littrow configuration, the wavelength is changed by tilting the grating which changes the 0th order output beam as well. A fixed output beam is necessary for seeding the semiconductor power amplifier. Second, a prism can be used instead of a mirror in the Littman-Metcalf configuration so the beam can be retro-reflected back to the laser diode in the side-to-side direction, thus removing the need for a tilt adjustment. In contrast, the Littrow configuration requires a careful tilt adjustment of the diffraction grating. Finally, the light makes two passes off of the grating in the Littman-Metcalf configuration which doubles the wavelength selectivity over the Littrow cavity. Bringing the light in at grazing incidence further increases the wavelength selectivity by illuminating more lines of the grating with the beam. While the Littrow cavity is more simple to construct, the Littman-Metcalf configuration was chosen for these distinct advantages.

Facet Reflectivity of the Semiconductor Laser

The cleaved end facets of the laser diode naturally provide a reflectivity near 30% thanks to the large step in the index of refraction from the waveguide inside the diode to

air. The light generated inside the waveguide is tightly confined such that the light exits the front facet at normal incidence as it passes into the air. We can estimate the reflectivity by:

$$R = \left(\frac{n_{laser} - n_{air}}{n_{laser} + n_{air}} \right)^2 \qquad 2.2.1$$

In the case of the 935nm laser diode used in this project, $n_{laser} = 3.61$ and $n_{air} = 1.00$ for a facet reflectivity of R = 32.1%. Because the front and rear facets are cleaved along crystalline planes, they act as very parallel, partially reflecting mirrors. The facets form a miniature Fabry-Perot optical cavity causing longitudinal modes to form inside the waveguide. This generates an intensity modulation in the output spectrum (Fig. 2.2.2).



Figure 2.2.2. Parallel, reflective facets of the diode laser generates longitudinal facet modes in the output spectrum.

The physical length of the 935nm laser device was measured with an optical microscope to be L = 770μm and the index of refraction of the waveguide $n_{laser} = 3.61$ was provided by the manufacturer. The facet mode spacing is calculated to be $\Delta\nu = 54.0$GHz which corresponds to $\Delta\lambda = 0.156$nm at $\lambda = 930$nm using:

$$\frac{\Delta\lambda}{\lambda} = \frac{\Delta\nu}{\nu} \rightarrow \Delta\lambda = \frac{\lambda^2 \Delta\nu}{c} \qquad 2.2.2$$

This agrees well with $\Delta\nu = 52.1$GHz or $\Delta\lambda = 0.150$nm mode spacing measured from the output spectrum using an optical spectrum analyzer (HP71450B). These longitudinal "facet modes" of the laser diode can be problematic in an external cavity. For instance, any wavelength reflected back to the laser diode by the external cavity that is *not* resonant inside the Fabry-Perot laser is forbidden. This significantly reduces the wavelength tuning of the ECDL. The most desirable condition is to eliminate the Fabry-Perot cavity of the laser diode completely such that the device acts purely as a gain medium for the external cavity allowing the amplification of all wavelengths within its gain bandwidth. One method to approach this ideal condition is to evaporate a thin, anti-reflective (AR) coating onto the front facet of the laser diode. SiO_x with $1 < x < 2$ is a typical material used as the AR coating. The oxygen content is adjusted by varying the oxygen pressure during the evaporation of SiO onto the laser facet. The oxygen content is adjusted until the index of refraction of the SiO_x coating satisfies the following condition:

$$n_{AR} = \sqrt{n_{LD} \cdot n_{air}} \qquad 2.2.3$$

The thickness of the AR coating is an integral number of quarter wavelengths of the design wavelength. An error in the refractive index of the coating results in a nonzero reflectivity at the facet, while an error in the thickness of the coating shifts the wavelength of the minimum reflectivity [21]. Experience using AR coated laser diodes in various ECDL's built in the lab have shown that a reflectivity of $R \leq 10^{-4}$ is necessary

for satisfactory wavelength tuning. Recent progress using multi-layer AR coatings have reduced the front facet reflectivity to $R = 5 \times 10^{-5}$ [22]. The front facet refectivity can be further reduced to 2×10^{-5} by designing the layers to compensate for the non-uniform index of the output aperture at the "wings" of the output intensity profile [23]. The front facet of the 935nm laser diode used for this project received a custom AR coating of $R \sim 10^{-4}$ as a generous favor from the supplier of the laser [24]. The laser diode comes commercially available with an $R = 0.95$ highly reflective (HR) coating on the back facet and an $R = 0.1$ AR coating on the front facet to optimize power output. The 0.1 AR coating was etched off before receiving the 10^{-4} coating. The back facet of the diode maintained its $R = 0.95$ HR coating so that it could act as the end mirror of the external cavity. The output spectra of the laser diode with the standard $R = 0.1$ and the special $R = 10^{-4}$ AR coatings on the front facet are compared in figure 2.2.3.

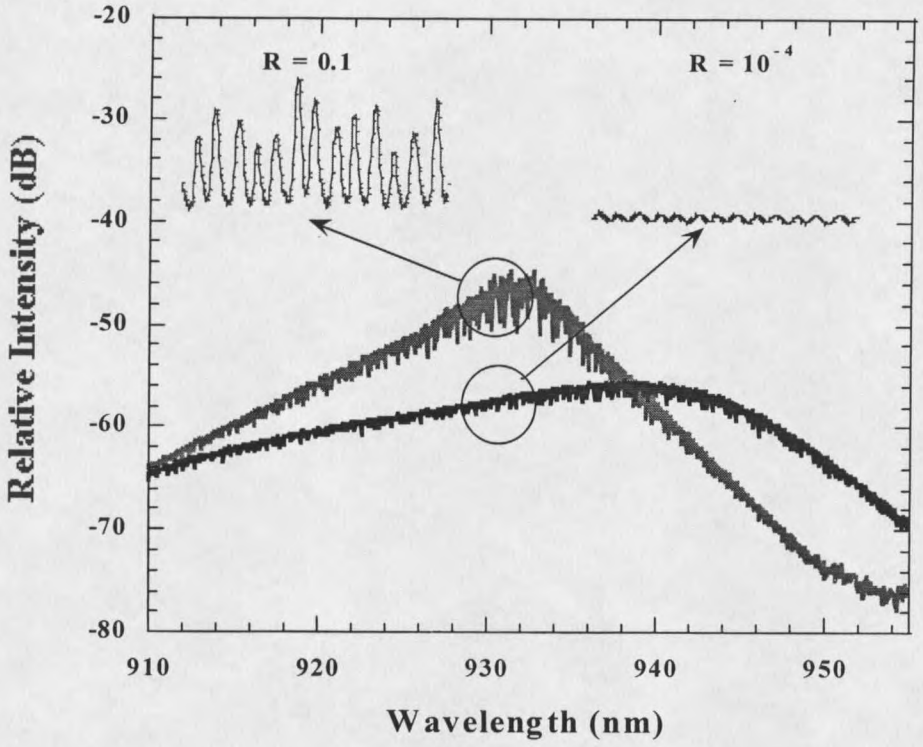


Figure 2.2.3. Spectral output of 935nm diode laser with standard R = 0.1 and R = 10^{-4} AR coating applied to its front facet. The rear facet remains at R = 0.95 for both cases.

The AR coating reduces the intensity modulation and provides a near-constant gain for all wavelengths in the gain bandwidth. Notice how the addition of the 10^{-4} AR coating shifts the center of the output spectrum to a longer wavelength. This is because the narrow-band AR coating is able to suppress the lasing at the design wavelength of 935nm and less at either longer or shorter wavelengths. Emission at longer wavelengths is preferred because there is a greater population of carriers in the lower levels of the energy bands of the optical transition.

Applying a very low reflective coating of $R < 10^{-4}$ is difficult, costly and there is some question as to their durability for flight or space use. As an alternative to AR coatings, the waveguide can be curved such that the light exits the front facet at an angle (Fig. 2.2.4)

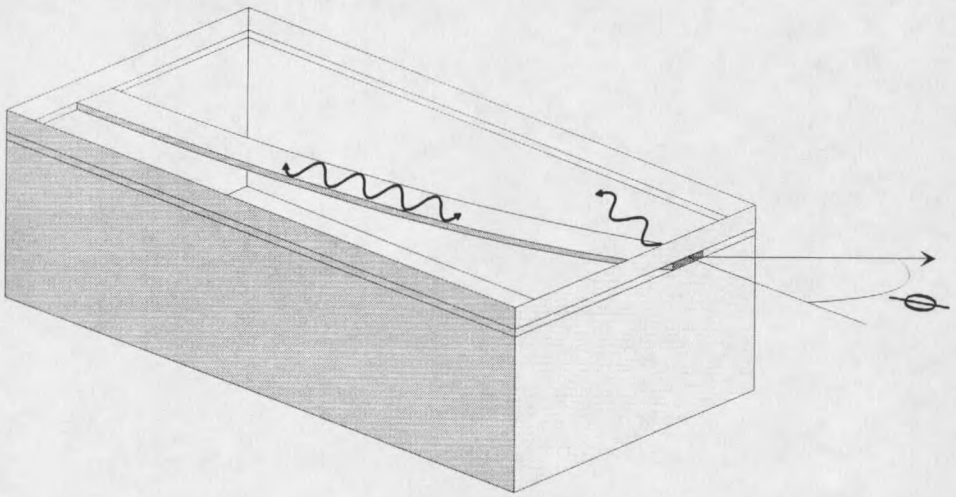


Figure 2.2.4. A Single Angled Facet (SAF) semiconductor laser. Photons which do not exit the front facet of the device are scattered into the substrate and absorbed instead of being reflected back into the waveguide where they can be amplified.

The waveguide is normal to the back facet and intersects the front facet at 7° relative to the facet normal. The remaining light will be reflected off the front facet back into the laser substrate away from the wavequide where it is absorbed. Very little light is scattered back into the waveguide resulting in an effective reflectivity as low as $R = 2 \times 10^{-5}$ with no AR coating! [25]. Typically, a standard AR coating of 5×10^{-2} is applied to the front facet to reduce the output loss. These devices exhibit unparalleled performance in an external cavity and are quickly replacing the Fabry-Perot type laser diodes in the 935nm ECDL and in the other ECDL's developed in the lab [26].

Longitudinal Modes of the External Cavity

Longitudinal modes arise from resonances of the external optical cavity defined by the highly reflective rear facet of the diode and the highly reflective prism (Fig. 2.2.5)

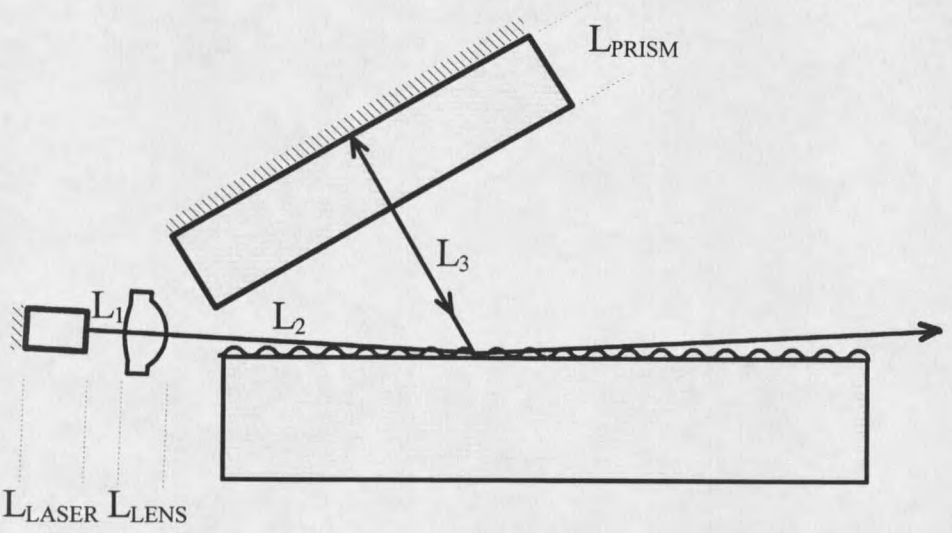


Figure 2.2.5. Adding up the optical path lengths of external cavity. Hatch marks at the back facet of the laser diode and the knife edge of the prism indicate the effective end mirrors of the optical resonator.

For simplicity, assume the front facet of the laser diode is AR coated so that R = 0 allowing us to neglect the longitudinal modes caused by the front and rear facets. In this ideal case, the semiconductor is used only as a gain medium with a rear reflector. We can model the external cavity as a Fabry-Perot resonator whose optical path length is defined by:

$$L_{ECDL} = n_{LASER}L_{LASER} + L_1 + n_{LENS}L_{LENS} + L_2 + L_3 + n_{PRISM}L_{PRISM} \qquad 2.2.4$$

The following table lists the various indices of refraction and path lengths for the 935nm ECDL designed and built for this project.

Table 2.2.2. Optical path length of the 935nm external cavity. The overall path length $L_{cavity} = 57.52mm$ when the prism angle is set to reflect $\lambda = 935nm$ light.

Actual Length (mm)	n(λ=935nm)	Optical Path Length (mm)	Description
$L_{LASER} = 0.770$	3.61	2.78	Length of Laser Diode
$L_1 = 2.59$	1.000	2.59	Laser Diode to Lens
$L_{LENS} = 2.94$	1.594	4.69	Lens Thickness
$L_2 = 25.06$	1.000	25.06	Lens to Diffraction Grating
$L_3 = 13.01$	1.000	13.01	Grating to Prism Face
$L_{PRISM} = 6.22$	1.508	9.39	Height of Prism, Face to Knife Edge

The spectral spacing of the longitudinal modes of the external cavity can be estimated from the net optical path length of $L_{cavity} = 57.52mm$ to be:

$$\Delta\nu_{cavity} = \frac{c}{2L_{cavity}} = 2.61GHz \qquad 2.2.5$$

For comparison, notice the external cavity mode spacing is much smaller than the facet mode spacing of 52GHz and significantly smaller than the 10dB gain bandwidth of 15THz.

The structure of the external cavity modes depends on the effective reflectivity of the end mirrors of the cavity. This largely depends on the diffraction and reflection efficiency of the diffraction grating at the chosen incident angle α and diffracted angle β. I chose to use a 1600 lines/mm aluminum coated holographic grating from Spectrogon for its excellent first order diffraction efficiency even for large incident angles. Figure 2.2.6 shows how the 1st order diffraction efficiency varies with wavelength for s and p-polarized light at a grazing angle of incidence of $\alpha = 85^\circ$ [27].

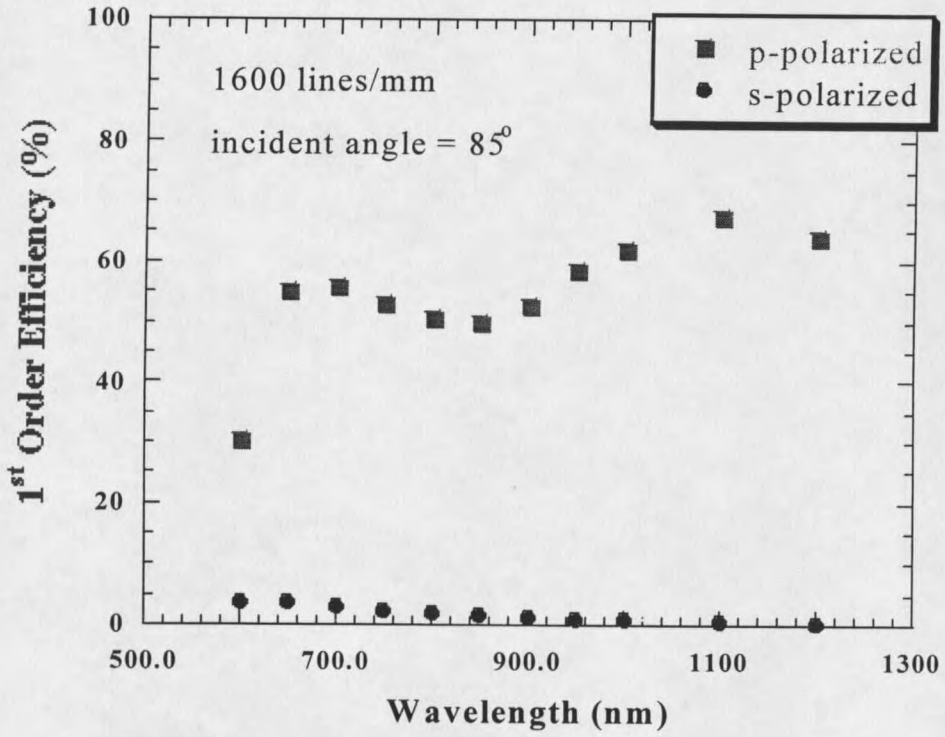


Figure 2.2.6. Predicted 1st order diffraction efficiency for 1600 lines/mm holographic grating. Actual efficiency at $\alpha = 87^{\circ}$ was less than that predicted at $\alpha = 85^{\circ}$.

The wavelength selectivity, or dispersion of the first order output from the grating, depends on the total number of lines N illuminated by the incident beam. For this reason, a large incident angle α is favorable so that it will spread the collimated beam from the laser diode out over a large number of grating lines. Therefore, in order to maximize the dispersion and still maintain a reasonably good diffraction efficiency, an incident angle of $\alpha = 87^{\circ}$ was chosen for this external cavity laser. The first order diffracted beam exits the 1600 lines/mm grating at an angle of β back towards the collimated laser diode according to the grating equation [28]

$$\lambda = d(\sin\alpha + \sin\beta) \qquad 2.2.6$$

d = 1mm/1600 lines and represents the spacing between the grating lines. The angles are defined by figure 2.2.7 below:

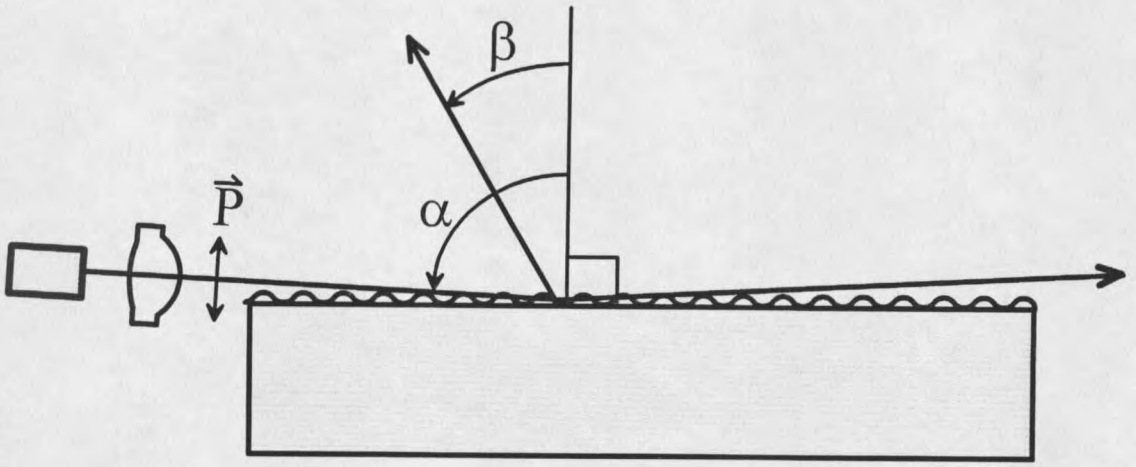


Figure 2.2.7. Incident and diffracted angles relative to the normal of the diffraction grating surface. Incident light is polarized parallel to the plane of incidence.

From the above grating equation, the diffracted angle $\beta = 30^{\circ}$ for an incident angle of $\alpha = 87^{\circ}$, $\lambda = 935$nm and $d = 0.625\mu$m. Choosing a diffraction grating such that the number of lines per mm provides a diffraction angle of roughly 30° as shown above seems to be optimal for ECDL designs. N>1600lines/mm generates angles greater than 30° which become mechanically impossible to reflect with the prism without bumping into the laser diode mount. N<1600lines/mm generates angles less than 30° which means the dispersion of the grating has been reduced and may even allow a second order diffracted beam. Any light lost to second order diffraction will not be reflected back to the diode greatly reducing the optical feedback. Table 2.2.3 below lists the reflectivity's of the optical surfaces of the external cavity.

Table 2.2.3. Reflectivity's of optical surfaces of the external cavity at λ=935nm.

Optical Surface	Reflectivity	Comments...
Back facet of laser diode	0.95	from manufacturer
Front facet of laser diode	10^{-4}	from manufacturer
AR coated collimating lens	0.05	measured in lab
Diffraction Grating	0.33	1st order diffraction, p-polarized, measured
	0.54	0th order reflection, p-polarized, measured
AR coated prism	0.99	normal incidence, measured

The rear facet of the laser diode acts as the back mirror of the external cavity with reflectivity of $R_1 = 0.95$. Assuming the AR coated front facet has negligible reflectivity, the path of light to the prism and back experiences a net reflectivity of:

$$R_2 = (1-.05)_{lens}(0.33)_{grating}(0.99)_{prism}(0.33)_{grating}(1-.05)_{lens} = 0.10 \qquad 2.2.7$$

The first order reflectivity off of the grating enters twice because the beam diffracts off of the grating in both the forward and return path to the diode. The beam also passes twice through the collimating lens. This effective reflectivity of the "front mirror" assumes the numerical aperture of the collimating lens is large enough to capture 100% of the light diverging from the front facet of the laser diode (see "Beam Profile" in section 2.3). It also assumes 100% of the return light is coupled back into the waveguide of the laser diode, which is usually not the case. Only 40-50% of the light can typically be coupled back into the small aperture of the laser because of sub-micron alignment tolerances [29]. We will stick with $R_2 = 0.10$ for the purpose of modeling the external cavity modes.

The optical path length of the external cavity and the effective reflectivity of its end mirrors is all that is needed to satisfy the parameters of the Fabry-Perot resonator. A cavity whose mirrors have different reflectivity of R_1 and R_2 will have the same spectral output if it were to have identical mirrors with a reflectivity $R = (R_1R_2)^{1/2}$. For our cavity

where $R_1 = 0.95$ and $R_2 = 0.10$, the net reflectivity is $R = 0.31$. The finesse or "Q" of the cavity is rather low because the net reflectivity is poor.[30]

$$F = \frac{\pi\sqrt{R}}{1-R} = 2.5 \qquad 2.2.8$$

The finesse can also be determined by dividing the full width at half maximum of a mode by the mode spacing. If light were to pass through this Fabry-Perot cavity, its intensity would vary with wavelength according to:

$$M(\lambda) = \left[1 + \left(\frac{2F}{\pi}\right)^2 \sin^2\left(\frac{2\pi L}{\lambda}\right)\right]^{-1} \qquad 2.2.9$$

The spectral profile of the external cavity modes modeled from this intensity is shown below in figure 2.2.8.

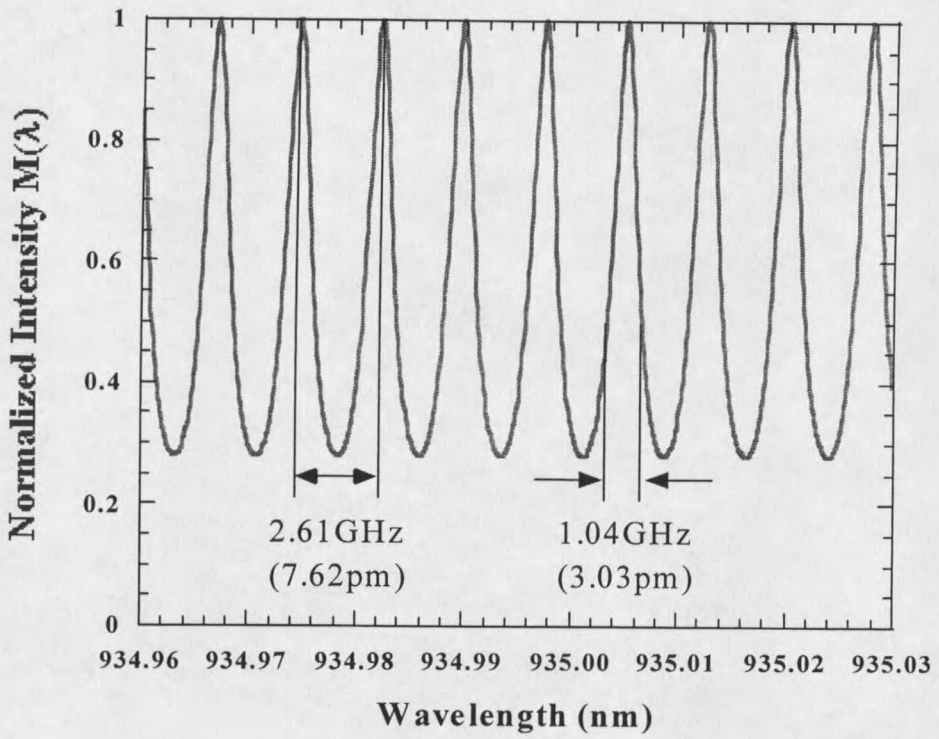


Figure 2.2.8. Calculated longitudinal modes of the external cavity. The low reflectivity of the "output mirror" provides a low finesse of 2.52.

In order for the output of the external cavity diode laser to be single mode, the diffraction grating must be able to pick out only one of the above external cavity modes and filter the rest of the modes out. This challenge will be discussed next.

Wavelength Selection by the Diffraction Grating

The diffraction grating is the wavelength selective element in the external cavity that will allow tuning of the output wavelength of the ECDL. In addition to tuning the wavelength, the grating will also provide single mode output through the careful selection of the grating and parameters of the optical configuration. The goal is to configure a particular diffraction grating whose dispersion (or wavelength selectivity) is narrow

enough to pick out only one external cavity mode to be amplified by the semiconductor laser. The normalized spectral intensity distribution describing the dispersion of the diffraction grating can be described by [31]

$$G(\lambda)=\left[\frac{\sin\left(\frac{N\pi d}{\lambda}(\sin\alpha+\sin\beta)\right)}{N\sin\left(\frac{\pi d}{\lambda}(\sin\alpha+\sin\beta)\right)}\right]^2 \qquad 2.2.10$$

The incident angle $\alpha = 87^\circ$ and diffracted angle $\beta = 30^\circ$ have been defined above in figure 2.2.7. The spacing between the lines of the grating is represented by d = 1 mm/1600 and N is the total number of lines illuminated by beam. N is determined by the beam diameter (twice the beam waist, ω) and the incident angle α using simple trigonometry:

$$N=2\frac{1}{d}\left(\frac{2\omega}{\cos\alpha}\right) \qquad 2.2.11$$

Recall that the laser diode is rotated so the polarization of the output beam is perpendicular to the lines of the grating. Therefore the narrow, less divergent axis of the beam is chosen to spread out over the grating. The factor of 2 is present because the beam diffracts twice off the grating during its round trip to the prism and back to the diode. This effectively doubles the dispersion of the grating, which is one of the strong advantages of the Littman-Metcalf configuration over the Littrow configuration. The spectral intensity distribution of the first order diffracted beam is plotted below for a incident beam with a waist of ω = 1.25mm at the narrow axis using a f = 4.5mm collimating lens (Fig 2.2.9).

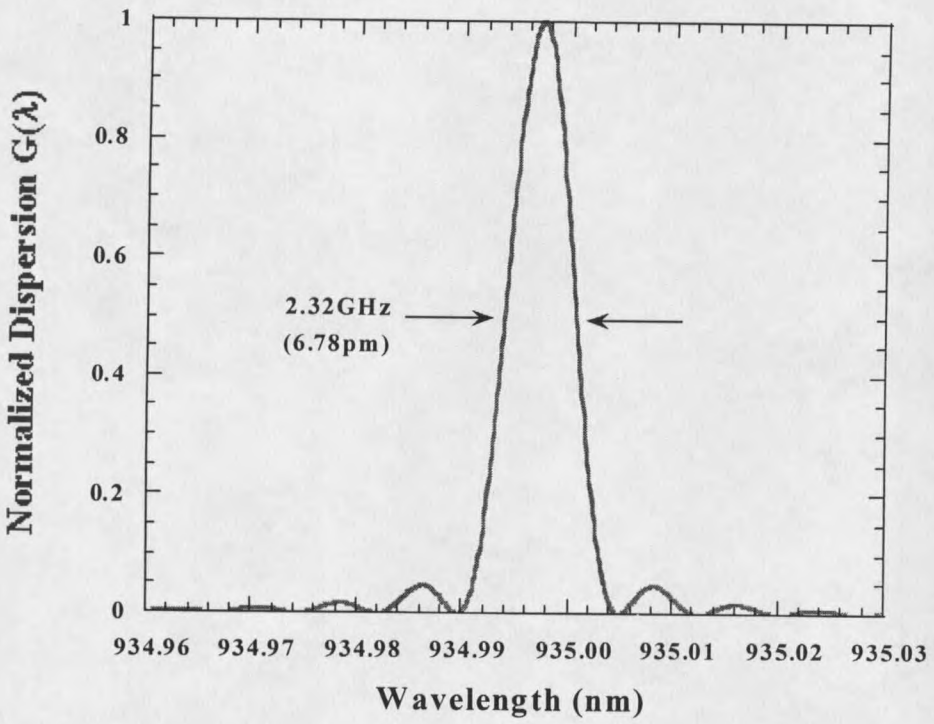


Figure 2.2.9. Spectral dispersion of 1600lines/mm grating used in the 935nm ECDL.

The narrow axis of the beam is spread out over 47.8mm of the grating, illuminating over 76,400 lines. This provides excellent dispersion with a FWHM linewidth as narrow as $\Delta\nu_{grating}$ = 2.32GHz; nearly equal to the external cavity mode spacing of 2.61GHz calculated earlier.

Conditions for Single Mode Operation

The objective is to adjust the length of the external cavity to fine tune the spacing between the external cavity modes such that the diffraction grating can select only one of the modes. This will ensure single mode operation of the ECDL. The optical configuration of the 1600lines/mm holographic grating allows for a narrow dispersion

linewidth of $\Delta\nu_{grating} = 2.32GHz$. It turns out that an optical path length of L = 57.5mm generates an external cavity mode spacing of $\Delta\nu_{cavity} = 2.61GHz$ which provides the optimum wavelength selection. This can be seen graphically by the overlapping the cavity mode profile with the dispersion profile of the diffraction grating (Fig. 2.2.10)

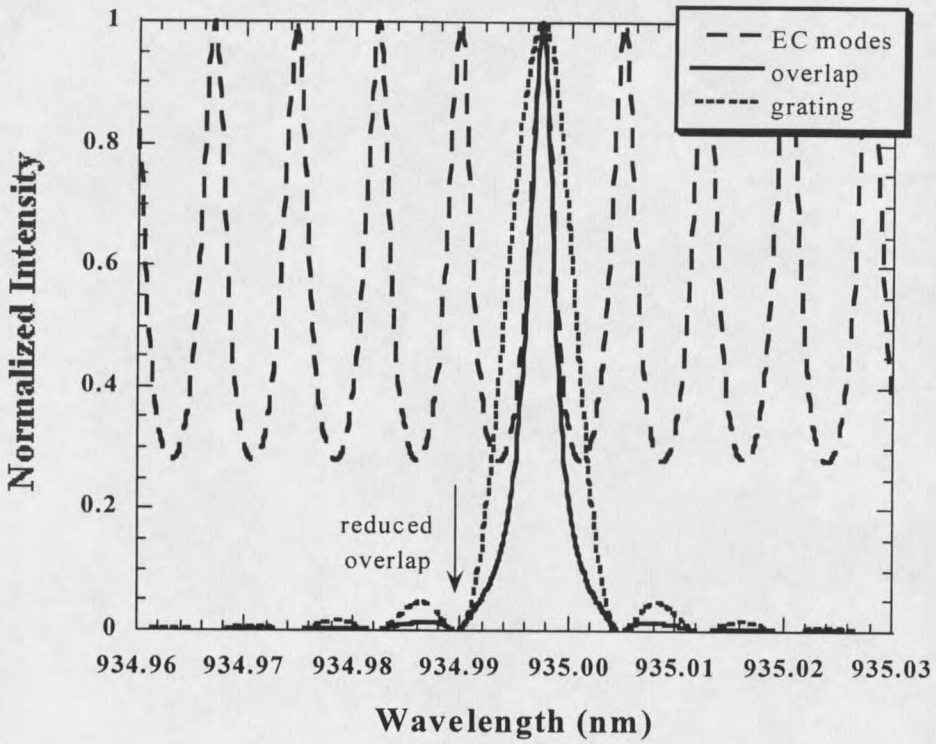


Figure 2.2.10. Spectral overlap of the external cavity modes with the dispersion profile of the diffraction grating. The spacing of the external cavity modes are optimized for single mode output of the ECDL.

Notice that the dispersion of the grating is narrow enough to allow only one external cavity mode under its profile. In addition, the spacing of the modes force their minima to overlap with the maxima of the 4% side lobes of the grating profile. This discourages these modes to be amplified by the laser diode. This reduced overlap condition will be met if the external cavity mode spacing is set equal to the spacing of the minima in the

grating profile. This is a convenient way to determine the number of lines N that need to be illuminated to satisfy the reduced overlap condition. The ratio of the external cavity mode spacing to the width of the dispersion profile of the grating that guarantees this single mode operation is:

$$\frac{\Delta\nu_{cavity}}{\Delta\nu_{grating}} = \frac{2.61GHz}{2.32GHz} \rightarrow 1.125 \qquad 2.2.12$$

When a design of any type of external cavity containing a wavelength selective element satisfies this criteria, it is guaranteed to provide single mode output. Other Littman-Metcalf lasers have been built in the lab at 795 and 1550nm that satisfy this condition and are indeed single mode.

Arriving at the ratio of 1.125 can be demonstrated graphically by varying the optical path length of the external cavity and looking at the overlap of the cavity modes with the dispersion profile of the grating. For instance, suppose the cavity length is decreased by 30%. The resulting overlap is shown below (Fig. 2.2.11)

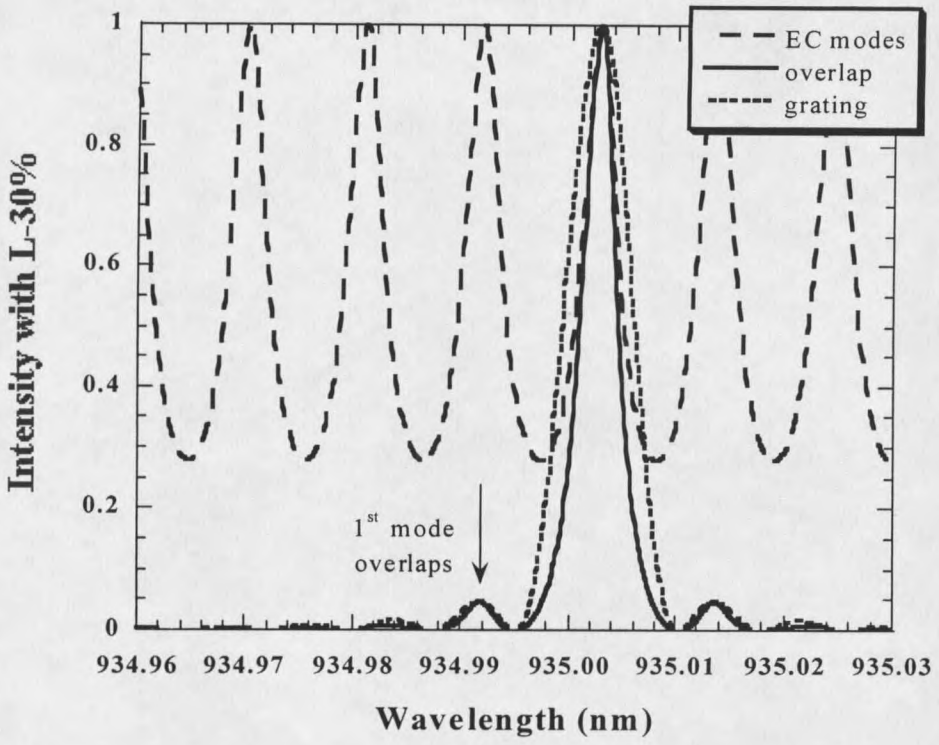


Figure 2.2.11. Spectral overlap of the cavity modes with the grating dispersion resulting from reducing the optical path length of the cavity by 30%.

While the dispersion of the grating is narrow enough to allow only one external cavity mode under its profile, it also allows the first neighboring modes to overlap nicely with the 4% lobes in the grating profile. Although seemingly small, allowing these first side modes to reflect back to the laser diode where they can be amplified nonlinearly can cause the ECDL output to be multimode. This is especially true if the central mode is out of phase with the cavity and the side modes are in phase. Now suppose the cavity length is increased by 30% causing the spacing between the cavity modes to decrease. The resulting overlap is shown below (Fig. 2.2.12)

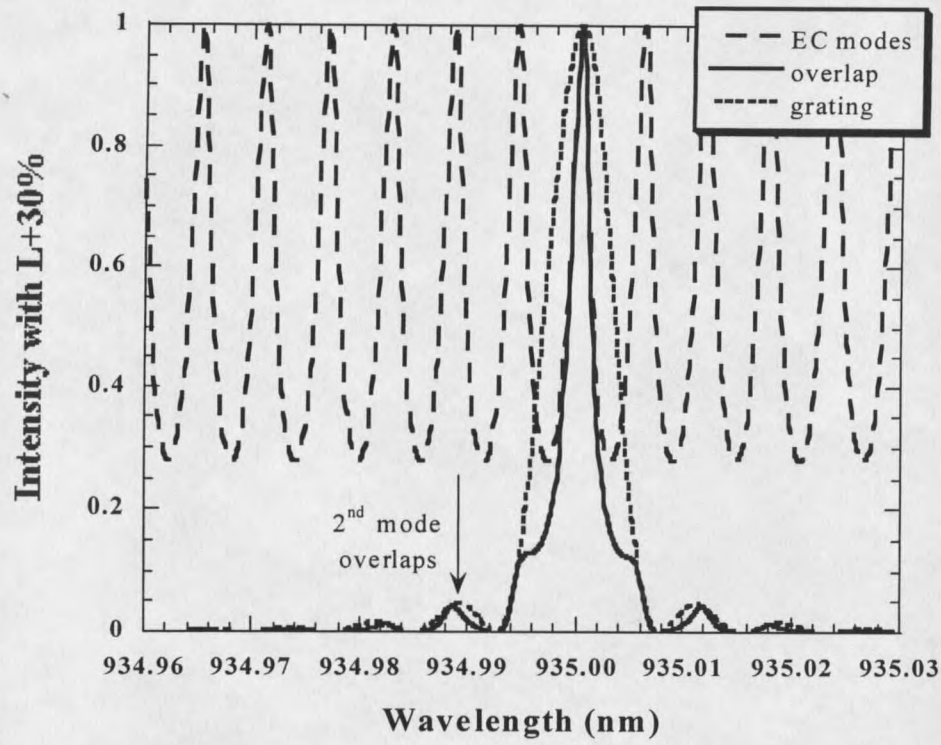


Figure 2.2.12. Spectral overlap of the cavity modes with the grating dispersion resulting from increasing the optical path length of the cavity by 30%.

In this case, the first neighboring modes are able to partially squeeze under the grating profile. In the event the center wavelength of the dispersion profile overlaps two cavity modes, both modes will fit under the grating profile at the same time with the same gain. This will cause the laser to hop from one mode to the other increasing the intensity noise and reducing the mode suppression ratio of the output [32]. Notice also that the second modes overlap well with the 4% lobes. Allowing these second side modes to reflect back to the laser diode can also cause multimode output.

The literature states that single mode operation of an ECDL can be achieved as long as the longitudinal mode spacing of the external cavity, $\Delta\nu_{cavity,}$ is approximately

equal to the FWHM linewidth of the dispersion of the grating, $\Delta\nu_{grating}$ [33,34]. However, the demonstration above suggests that this requirement is not strict enough. A more exact relationship between the cavity modes and the dispersion of the grating of $\Delta\nu_{cavity}/\Delta\nu_{grating} = 1.125$ guarantees the output of the ECDL will be single mode.

Pivot Point for Continuous Tuning

A condition for single mode operation of the ECDL was defined above. The challenge is to maintain this condition while tuning the wavelength of the laser. Wavelength tuning is accomplished by rotating the beam-folding prism in the plane of the external cavity. This reflects a particular wavelength that has been resolved and separated from all other wavelengths by angle by the first order diffraction of the grating. The narrow wavelength band of light will then be reflected back to the semiconductor laser where it can be amplified. Strictly rotating the prism without any translation will vary only the center wavelength of the reflected light without changing the position of the external cavity modes. This will cause the reflected light to hop from mode to mode as the wavelength is tuned (Fig. 2.2.13).

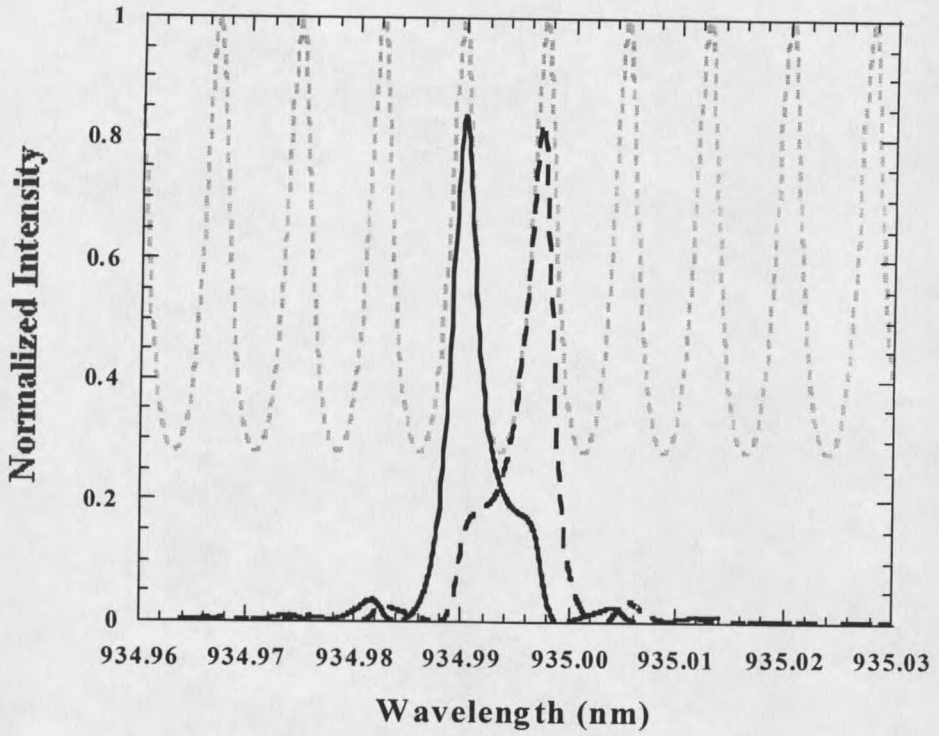


Figure 2.2.13. Overlap of external cavity modes with grating profile shows how a mode hop occurs when the wavelength tuning is not synchronized with the external cavity modes.

This causes steps in the wavelength tuning that are unacceptable for high resolution spectroscopy where continuous tuning of a single mode is needed. For instance, these mode hops were often the culprit for generating broad absorption lines or additional "mystery" lines when doing high resolution spectroscopy of acetylene gas at 1530nm [35]. Figure 2.2.14 shows a step in the wavelength caused by a mode hop while tuning the 935nm ECDL when the cavity length is not synchronized with the angle of the prism.

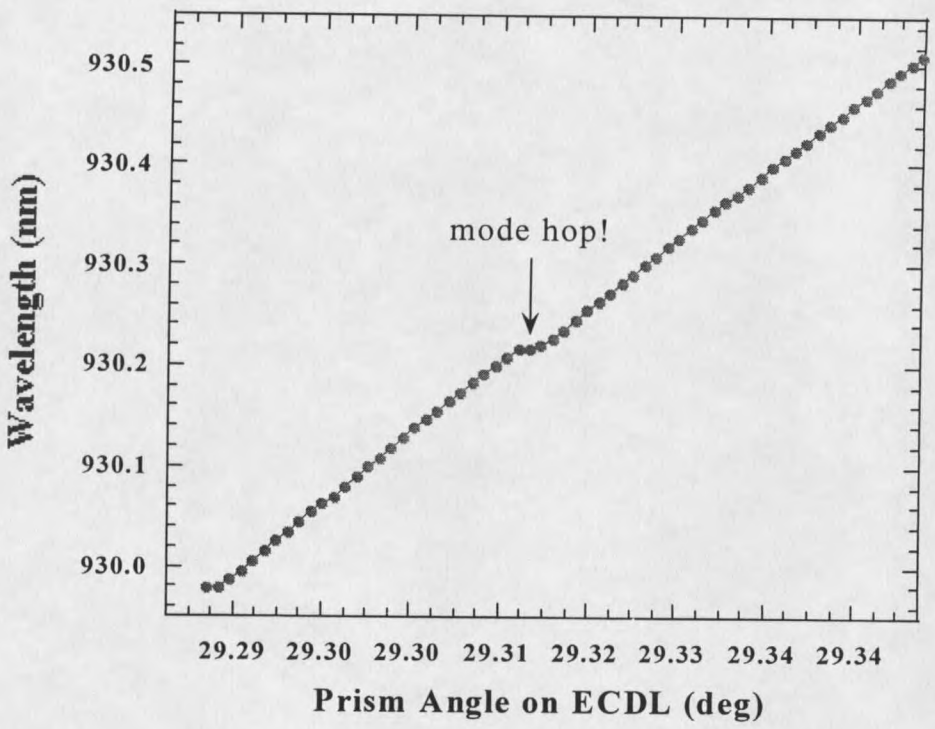


Figure 2.2.14. Mode hops cause a discontinuous step in the output wavelength as the prism angle is changed.

The position of the external cavity modes can be synchronized with the center wavelength of the grating profile by translating the prism as it is rotated. One method is to select a mechanical pivot point for the prism to rotate about such that the cavity length corresponds to the rotation of the prism allowing a single cavity mode to track with the center wavelength of the grating profile. The location of this pivot point can be determined by requiring the phase of the light resonant in the external cavity to remain constant while the cavity length changes with the rotation of the prism [19,20] Changing the cavity length will also change the frequency spacing between the modes but this is a small effect compared to the translation of the mode spectrum for a large number of modes, and can be ignored [see Appendix A]

The location of the mechanical pivot point can be determined as follows. Consider the three primary optical planes of the external cavity: one plane along the back facet of the laser diode, a second plane along the face of the diffraction grating, and a third plane along the knife-edge of the beam folding prism. The actual locations of these planes must account for the index if refraction of the optical components in the path of the beam. For instance, the prism plane actually lies $n_{PRISM}*L_{PRISM}$ above the knife edge of the prism. Similarly the diode plane lies $n_{LASER}*L_{LASER} + n_{LENS}*L_{LENS}$ behind the actual back facet of the laser diode. One possible location for a mechanical pivot point is at the intersection of all three planes, as suggested by Liu and Littman[19]. McNicholl and Metcalf suggested a less restrictive condition for the pivot point that allowed the ECDL to be significantly more compact, leading to better overall frequency stability[20]. They suggested the pivot point be placed on one of the planes, such as the plane of the grating, and the distance from the pivot point to the normal intersection of each of the other two planes be equal. These distances are labeled "a" and "b" in figure 2.2.15.

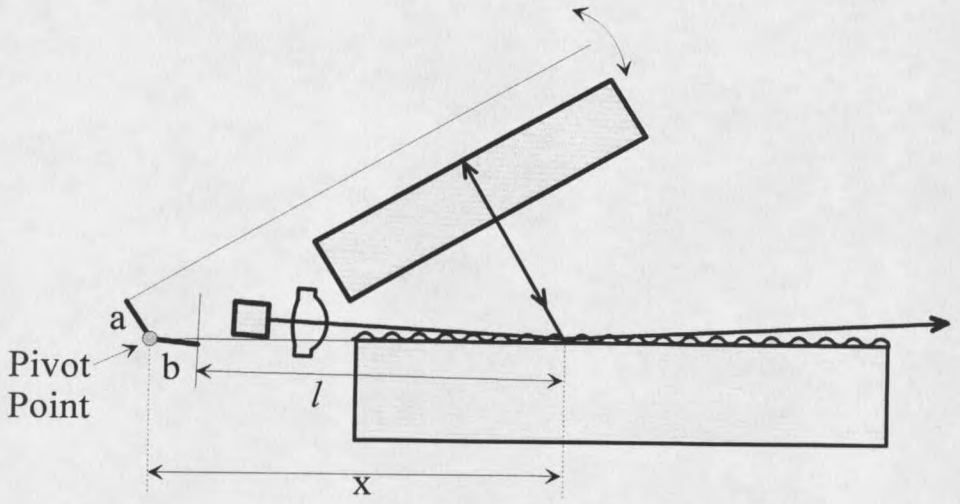


Figure 2.2.15. The three principle planes of the external cavity. The actual index of refraction of the optical components is compensated for by moving the positions of the laser diode plane and prism plane away from the center of the external cavity.

These authors were describing the construction for dye laser optical cavities which I found could be directly applied to external cavity diode lasers. Continuous tuning should result as long as the distances a and b from the pivot point are equal. This condition promises the round trip phase of the light remains constant during wavelength tuning allowing the m^{th} cavity mode to synchronously tune with the wavelength selected by the grating.

The degree of continuous tuning depends on how precisely the pivot point is positioned. It was necessary to understand how accurately this point needed to be located in order to design the cavity so it could be made to machining tolerances. McNicholl and Metcalf adopt a somewhat arbitrary but reasonable convention of $2\pi/10$ for tolerable phase variation for the light resonant in the cavity. The accrual of phase as a function of wavelength tuning can be monitored as the prism is rotated about the pivot point using a

simple spread sheet. The optical path length L of the cavity varies with the angle β as the prism is rotated about the pivot point.

$$L(\beta) = l + \Delta l + a + x\cos(90 - \beta) \qquad 2.2.13$$

In this expression, x is the distance between the pivot point and the grating along the plane of the grating, a is the distance from the pivot point and the normal to the prism plane, and $l = n_{LASER}L_{LASER} + L_1 + n_{LENS}L_{LENS} + L_2$ as defined earlier in table 2.2.2. The wavelength reflected by the grating depends on the diffracted angle β by the grating equation:

$$\lambda(\beta) = d(\sin\alpha + \sin\beta) \qquad 2.2.14$$

The incident angle $\alpha = 87^\circ$ is held constant and $d = .625\mu m$ is the spacing between the lines of the 1600 lines/mm grating. Suppose we choose to scan the wavelength of the ECDL 10nm from λ_i to λ_f. The number of external cavity modes resonant in the cavity at the beginning of the scan is:

$$m_i(\beta) = \frac{2L(\beta)}{\lambda_i(\beta)} \qquad 2.2.15$$

If the pivot point is positioned in exactly the right spot, the number of modes should remain constant throughout the entire scan such that $m_i = m_f$. Any difference in the number of calculated cavity modes implies the phase of the light has changed by:

$$\varphi(\beta) = \frac{\pi}{2}(m_o - m_i(\beta)) \qquad 2.2.16$$

The tolerance in the position of the pivot point can now be estimated by offsetting one of the principle planes until the maximum tolerable phase change of $2\pi/10$ radians $= 36^\circ$ has been accrued (Fig. 2.2.16)

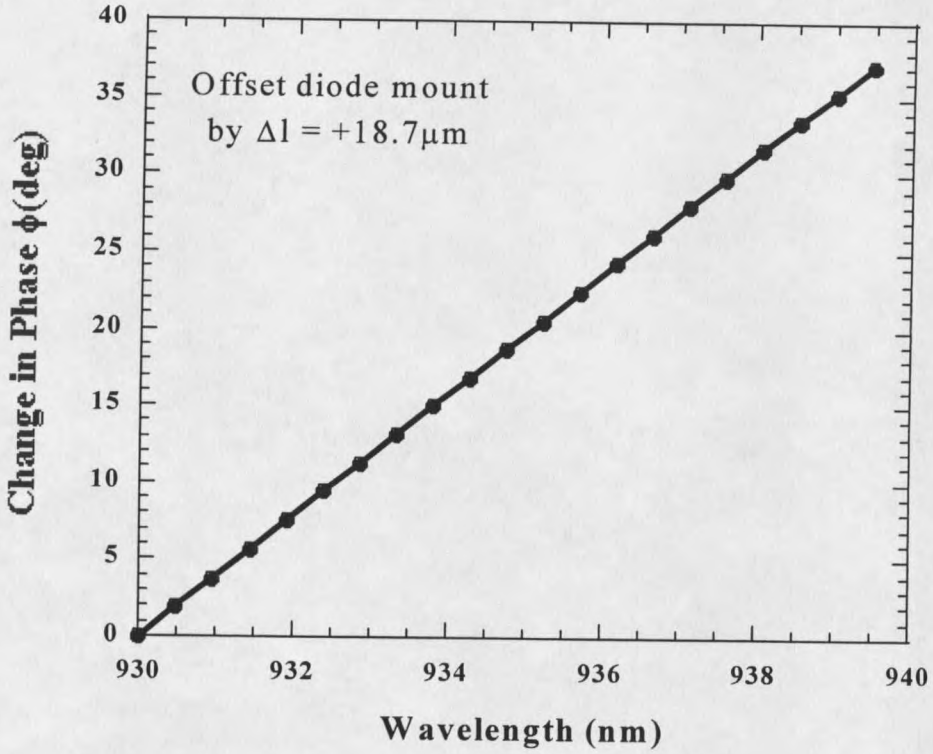


Figure 2.2.16. The location of the pivot point was displaced from its correct position by 18.7μm until 36° of phase was accrued during a 10nm scan.

An error in locating the pivot point by as little as 18.7μm along the axis of the grating is enough to cause the ECDL to mode hop over a 10nm tuning range! This is beyond machining tolerances, usually ± 50μm for any given part, especially for an assembly of parts that will define the actual location of the pivot point. One of the planes would have to be adjustable to μm type positioning after the cavity was assembled. I chose to adjust the plane corresponding to the back facet of the laser diode. This plane was adjustable by carefully sliding a mount holding the laser diode and collimating lens along the optical axis to the grating using a micrometer. The mount would have to be locked into place after determining the correct pivot point by demonstrating continuous

tuning. The actual mechanical construction of this mount and the rest of the ECDL will be discussed next.

Final Laser Design

All the physics concerning the cavity modes, dispersion of the grating and pivot point for continuous tuning was incorporated into the final mechanical design of the 935nm ECDL. Other considerations such as reducing the thermal mass, selection of materials, and fine adjustments for optical alignment were also engineered into the mechanical design. This section provides a tour of the laser design , discusses some of the highlights, and provides suggestions for future improvements. A mechanical drawing of the external cavity laser is shown below for reference (Fig. 2.2.17)

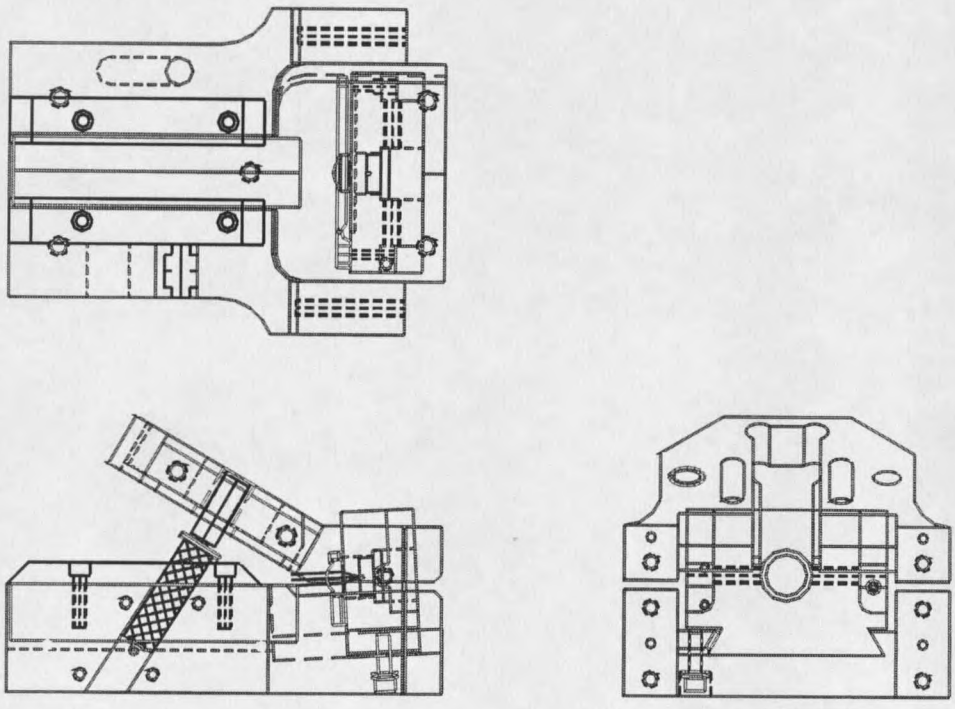


Figure 2.2.17. Mechanical drawing of 935nm ECDL.

The laser diode mount was machined from HF copper to remove heat as efficiently as possible from the laser diode providing good temperature control. The mount also holds a tiny aluminum mount for the f = 4.5mm collimating lens. The lens mount contains a flexure point with an adjustment that allows the collimation of the beam to be fine tuned while the laser is running, which proved to be necessary for maximizing the tuning range. 60 degree dovetails were milled into the bottom sides of the mount so that the laser diode and lens could move together as a unit, allowing the collimated source to slide along the axis of the incident beam. This adjustment moved the principle plane of the diode used to fine tune the location of the pivot point for continuous tuning. A corresponding dovetail was milled into one side of the pocket in the aluminum base plate to locate the diode mount. The other side of the pocket contained a 60° wedge that acted like a guide but could be locked down with a screw to secure the position the diode mount. A removable micrometer was temporarily attached to the rear of the base plate and used to push the diode mount forward until the pivot point was located. Long, thin sapphire rectangles lined the dovetails of the diode mount providing smooth stable adjustment of the diode. In fact, sliding the diode mount along these dovetails was stable enough for the 0^{th} order output beam to remain coupled into a single mode fiber while positioning the diode mount!

An aluminum plate is used to hold the beam folding prism. The plate is hinged to the base plate with two 0.020" thick plates of phosphor bronze shim stock. Phosphor bronze has excellent thermal conductivity so the temperature of the prism plate quickly comes to equilibrium with the rest of the temperature controlled cavity. The stiff material

is very "springy" and serves as an excellent hinge for the pivot point. The pivot area is restricted to a 0.062" region along the shim stock where it is attached to the base plate and prism plate with stainless steel dowel pins and #4x40 stainless steel cap screws. The slot for the prism in the prism plate was widened to position the prism directly over the beam. The prism could be locked down onto a narrow shelf using 4 cone-tipped nylon screws. This alignment tended to be more sensitive that predicted and future designs should include a way to finely adjust the side-to-side adjustment of the prism while keeping its axis aligned with the optical axis. No side-to-side tilting of the prism was necessary thanks to the retro-reflection capability of the prism along this degree of freedom. The prism plate contained a small 100 pitch ball-end screw that rested on top of a PZT stack held in the base plate. The screw provides coarse adjustment of the wavelength while the PZT provides the fine adjustment of the angle of the prism plate. The prism plate was made as light as possible to reduce its momentum so that the wavelength could be scanned as fast as possible using the PZT. Scan frequencies as high as 1kHz have been demonstrated.

The diffraction grating is held in a pocket milled into the base plate and is supported by 0.070" thick viton o-rings. Two delrin bars are used to compress the grating down 0.010" onto the o-rings until its surface is flush with the top surface of the base plate in order to locate the plane of the grating accurately. Teflon shims slide in between the walls of the pocket in the base plate and the sides of the grating to ensure the long axis of the grating is aligned along the optical axis (this aligns the lines of the grating perpendicular to the optical axis). The aluminum base plate of the cavity rests on

two, 15x30mm thermal electric coolers wired in series in order to temperature control the entire external cavity. A calibrated 10k-ohm thermistor is epoxied between the coolers in a 0.075" hole located in the bottom of the base plate. Strips of 0.002" Indium foil is used on the top and bottom of each cooler for good thermal contact. Nylon cap screws (not thermally conductive) were used to sandwich the coolers between the base plate and an aluminum heat sink plate. An LDC3722 laser diode controller from ILX Lightwave was used to supply current to the laser diode and to control the temperature of the cavity. The heat sink was bolted to a commercially available tilt stage which was highly modified to contain all the wires and connectors for the ECDL. This served as a solid base that could tilt and point the output beam of the laser as well. An black-anodized aluminum housing covered the ECDL and protected it from dust and air currents in the lab. The beam exited the cover through an AR coated window whose normal was held at 3° to the beam to avoid any stray back reflections back into the laser diode. The finished laser, with the cover removed, is shown below in figure 2.2.18.

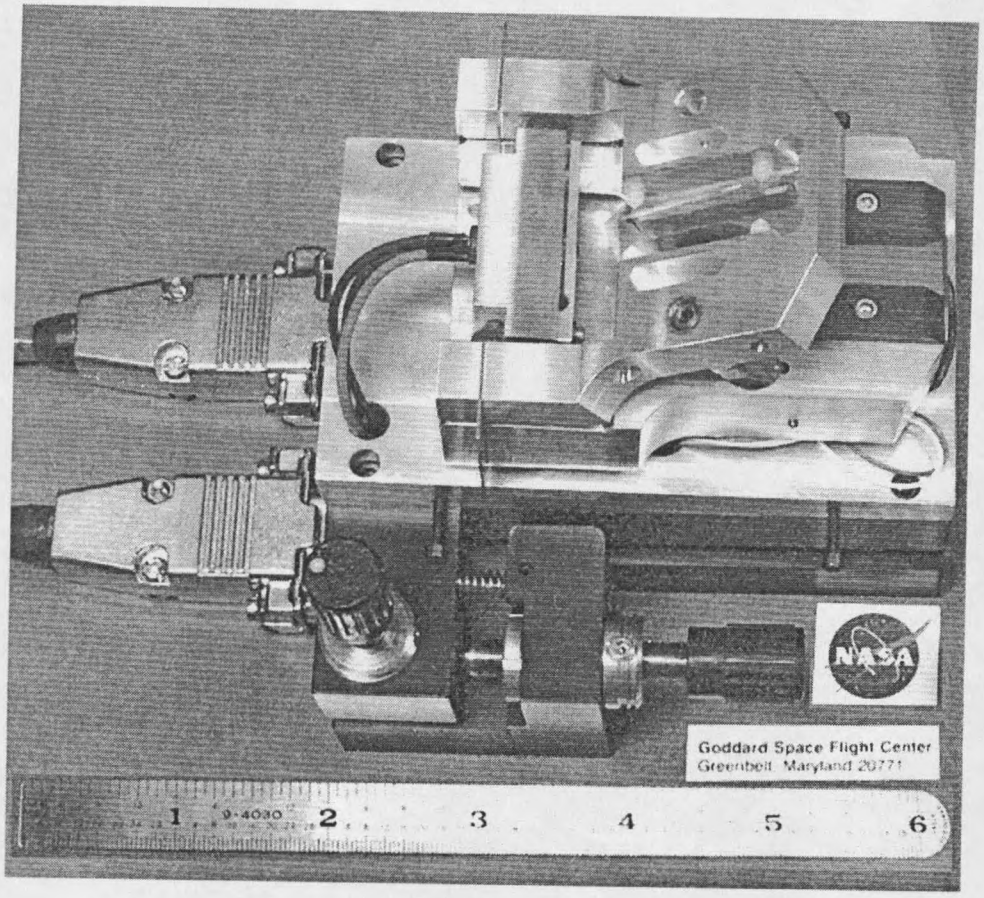


Figure 2.2.18. Photo of 935nm ECDL after assembly.

I am greatly indebted to Norman Williams, the machine shop supervisor of the MSU physics machine shop, for his patience in training me to machine the high precision parts needed for this project. Norman spent many hours helping me with the design of the mechanical parts so it was physically possible to machine them. Because of the tight tolerances of the mechanical components (±0.001"), I was granted permission to use the mill and lathe specifically reserved for Norman's projects. Norman's excellent instruction and strive for perfection has taught me valuable skills in both the design and

machining of high precision mechanical hardware that will continue to be important long past the completion of this project.

The table below list the optical components and the other specialty components used in the 935nm ECDL. The remaining components such as the lens mount, base plate, prism plate, heat sink, and cover were machined from 6061-T651 aluminum.

Table 2.2.4. Specialty components used in the 935nm ECDL.

Component	Part Number	Vendor
Fabry-Perot Laser Diode	SU 935 CD FP	Sensors Unlimited
AR coating for laser, R=10^{-4}	personal favor	Sarnoff Corp.
Collimating lens f = 4.5mm	350230-B	Geltech (for Thorlabs)
Holographic Grating	G1600 12x50x10 NIR	Spectrogon US Inc.
0.691"x0.070" viton o-rings	2015U88425	Air-Oil Products Corp.
Knife edge roof prism	BFP-1 custom	Continental Optic Crop.
AR coating for prism face, R<.5%	#A62 BBAR	OptoSigma Corp.
3/4" AR coated window for cover	W2-IF-0725-C-935-0	CVI Laser Crop.
Sapphire inserts on diode mount	SP103	Swiss Jewel Company
Sapphire disks on PZT, lens mount	8x1mm Sapphire	Scientific Materials
0.020" Phosphor Bronze flexure	9014K35	McMaster Carr
20mm PZT stack for tuning	AEO505D08	Thorlabs Inc.
3/16"x100 screw for tuning	F19SS-038	Thorlabs Inc.
15x30mm TEC's	CP 1.4-35-06L	Melcore Inc.
0.002 sheet In foil for TEC's	10101	Indium Corp. of America
10k-ohm calibrated thermistor	personal favor	ILX Lightwave
Current/Temperature controller	LDC3722	ILX Lightwave
Precision tilt stage	F-91TS	Newport Corp.

Summary of Laser Design

In designing a single mode, tunable external cavity diode laser, it is important to achieve a unique balance between the external cavity mode spacing and the dispersion of the diffraction grating. The following "recipe" was developed while designing the 935nm ECDL for the miniature water vapor lidar system. First, a laser diode must be

chosen whose center wavelength matches the wavelength region of interest. For continuous wavelength tuning, it is also important to apply a very good anti-reflective coating of 10^{-4} to the front facet of the semiconductor device if it is a Fabry-Perot type laser diode. Select a diffraction grating such that its first order diffraction occurs at an angle β such that $25^{\circ}<\beta<35^{\circ}$ toward the laser diode from the grating normal if the incident beam enters the grating at an angle α such that $83^{\circ}<\alpha<87^{\circ}$. This will allow the maximum number of lines to be illuminated by the grating, providing the narrowest possible dispersion. This will fix the number of lines of the grating and the relative angles of the external cavity. Next, choose a collimating lens with a focal length $3mm<f<5mm$ and has a high numerical aperture $NA>0.5$ in order to capture all of the light from the divergent beam from the laser diode. The short focal length keeps the overall cavity length minimized while providing a beam width that will fill most of the diffraction grating. Finally, when modeling the cavity, reduce the optical path length of the external cavity from the back facet of the laser diode to the knife edge of the prism until $\Delta\nu_{cavity}/\Delta\nu_{grating} = 1.125$ is satisfied. This will ensure single mode operation of the output of the laser. In order to achieve continuous tuning of this single mode output is to ensure the phase remains constant of the light resonant inside the cavity while the wavelength is being changed. A mechanical pivot point can be selected whose location will allow the angle of the prism to also adjust the path length of the cavity such that the same cavity mode can remain resonant as the wavelength is tuned. It is important to build in a fine adjustment into the laser design so that this pivot point can be accurately

set. This recipe has proven successful in designing similar ECDL's at other wavelengths including 795nm and 1550nm.

2.3 Laser Performance

Complete characterization of the output of the external cavity diode laser was necessary in order to determine if it would satisfy the strict requirements needed for the master oscillator for the mini-lidar water vapor system. This section discusses the laser linewidth, wavelength tuning, side mode suppression ratio, power and wavelength stability and beam quality. It is exciting that the only small, compact, and power efficient laser that could meet, and in many cases surpass, these requirements was the 935nm ECDL developed here.

Single Mode, Narrow Linewidth Output

It is especially important that the linewidth of the laser be much narrower than the water vapor absorption line in order to probe the line accurately. The 935.68nm water vapor absorption line has a Doppler broadened linewidth of slightly less than 1GHz at low pressures similar to what we expect to find in the atmosphere on Mars. Therefore, the laser linewidth should be roughly 1MHz in order to accurately measure the absorption line without having to deconvolute the two lines. As a first check, the output of the laser was measured using an optical spectrum analyzer (OSA). This diffraction grating-based instrument provides valuable, broad wavelength information. Unfortunately it has a resolution limited to just under 35GHz (0.1nm) which is not sufficient to measure the laser linewidth. In order to quickly and easily measure an upper limit of the linewidth of the laser at a higher resolution, a scanning fiber Fabry-Perot interferometer was used instead of the OSA [36]. This fiber coupled device is an ideal spectrometer for

measuring the relative frequency of the ECDL because it has a free spectral range of 17GHz and a resolution of about 25MHz. The free spectral range is wide enough to see any external cavity modes that might appear at 2.6GHz intervals. Figure 2.3.1 shows the optical setup for measuring the laser linewidth using the fiber Fabry-Perot.

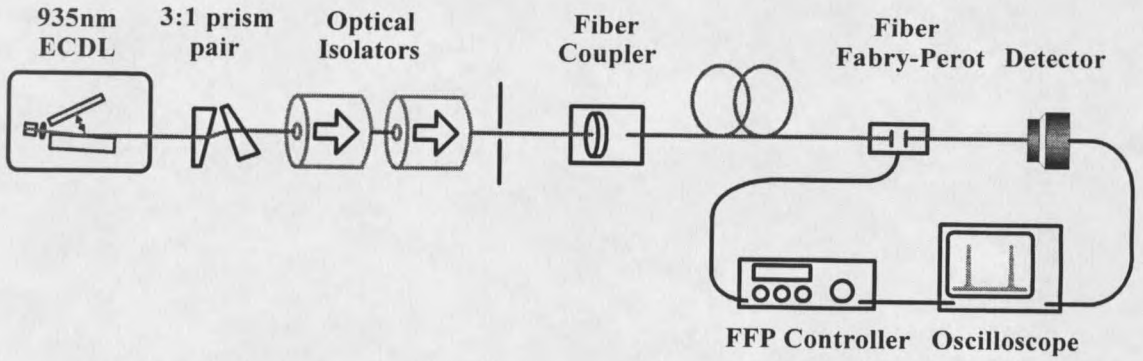


Figure 2.3.1. Experimental setup for measuring linewidth of ECDL using a scanning fiber Fabry-Perot interferometer.

The 3:1 oval output beam of the laser was reduced to a more circular beam as it passed through an anamorphic prism pair. The beam then propagates through a pair of optical isolators which eliminates back reflections from the fiber Fabry-Perot to a level of 75dB. The isolators use the principle of Faraday rotation in order to rotate the polarization of the return beam and block it using polarizers. The light passes through an alignment aperture and is then coupled into a single mode fiber using an f = 15.36mm, AR coated aspheric lens. The Fabry-Perot interferometer consists of two cleaved fiber ends, each with a high reflective coating, separated by a short intermediate length of fiber to contain the beam. The mirrored ends of the fiber are scanned back and forth using a PZT driven by a sawtooth ramp from the FFP controller. An amplified silicon detector

monitors the transmission of the fiber interferometer. Figure 2.3.2 shows a full width at half maximum linewidth of 21.5MHz measured using the fiber interferometer, which is at the limit of its resolution. Notice that no external cavity modes are present in the spectrum.

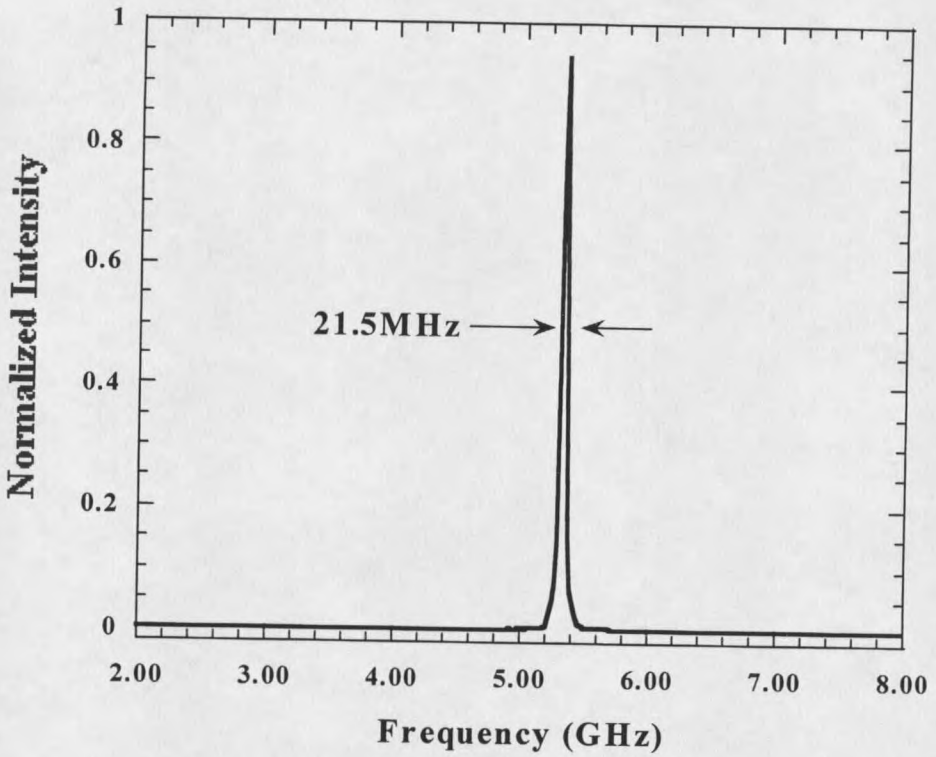


Figure 2.3.2 21.5MHz full width at half maximum linewidth of 935nm ECDL under CW operation as measured using a scanning fiber Fabry-Perot interferometer. This linewidth is at the resolution limit of the interferometer.

A more sensitive measurement of the laser linewidth is to overlap the optical frequencies of two identical lasers and measure the beat frequency using a radio frequency (RF) spectrum analyzer. This heterodyne method brings the optical frequency down to MHz frequencies where we can take advantage of RF spectrum analyzers with Hz-level resolution. The second laser ECDL source, known as "Herb", was actually the

predecessor to the current 935nm ECDL, also known as "Kelly". Herb was designed, built, and used at Goddard Space Flight Center for the early stages of this NASA project. Its source was a single angled facet (SAF) laser diode centered at $\lambda = 990$nm and was used to successfully characterize over 70 water vapor lines between 960 and 980nm. Unfortunately Herb was designed using a 1200 lines/mm diffraction grating and its output would occasionally be multi-mode (this is what actually prompted a more careful study of the ECDL design!). The SAF device in Herb was replaced with a 935nm Fabry Perot laser diode identical to the one used in Kelly with the exception of the anti-reflective coating applied to the front facet. Still, the laser was willing to operate single mode at a few wavelengths of its choice and provided a stable source very similar to Kelly, the ECDL developed for this project. The experimental setup to measure the heterodyne linewidth is shown below (Fig. 2.3.3).

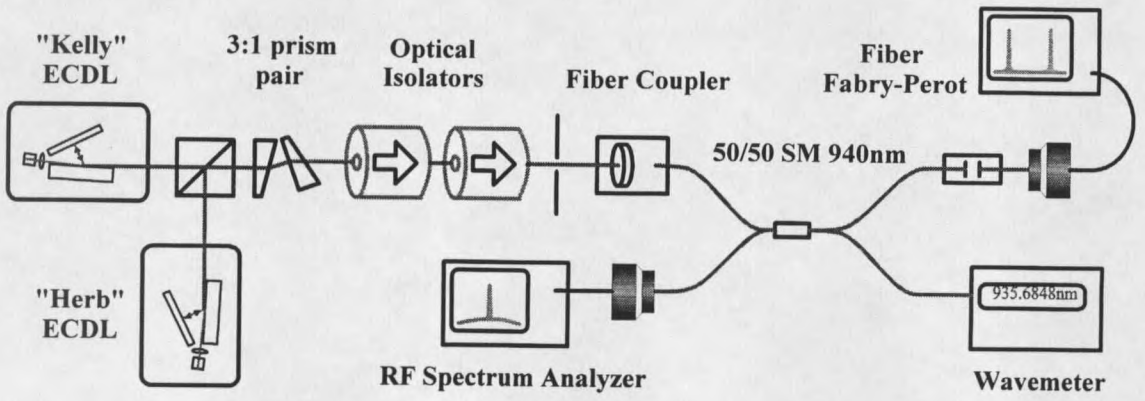


Figure 2.3.3. Setup for a heterodyne linewidth measurement by beating the optical output of two very similar ECDL's known as "Kelly" and "Herb".

The output of the two lasers were combined using a 50/50 beam splitter and passed through the same anamorphic prism pair and optical isolators as before in figure

2.3.1. Both beams were then launched into a 2x2 single mode fiber beam splitter using an f = 15.36mm AR coated aspheric lens. The single mode fiber provided excellent spatial overlap of the beams and conveniently delivered the light to the equipment for analysis. Kelly's wavelength was carefully overlapped with Herbs at 935.472nm by monitoring both the fiber Fabry-Perot interferometer and the wavelength measured on the wavemeter. A DC to 125MHz silicon detector from New Focus, Inc. was used to collect the beat frequency and deliver it to the RF spectrum analyzer. The single shot heterodyne laser linewidth for the convolution of the two lasers is shown in figure 2.3.4 below.

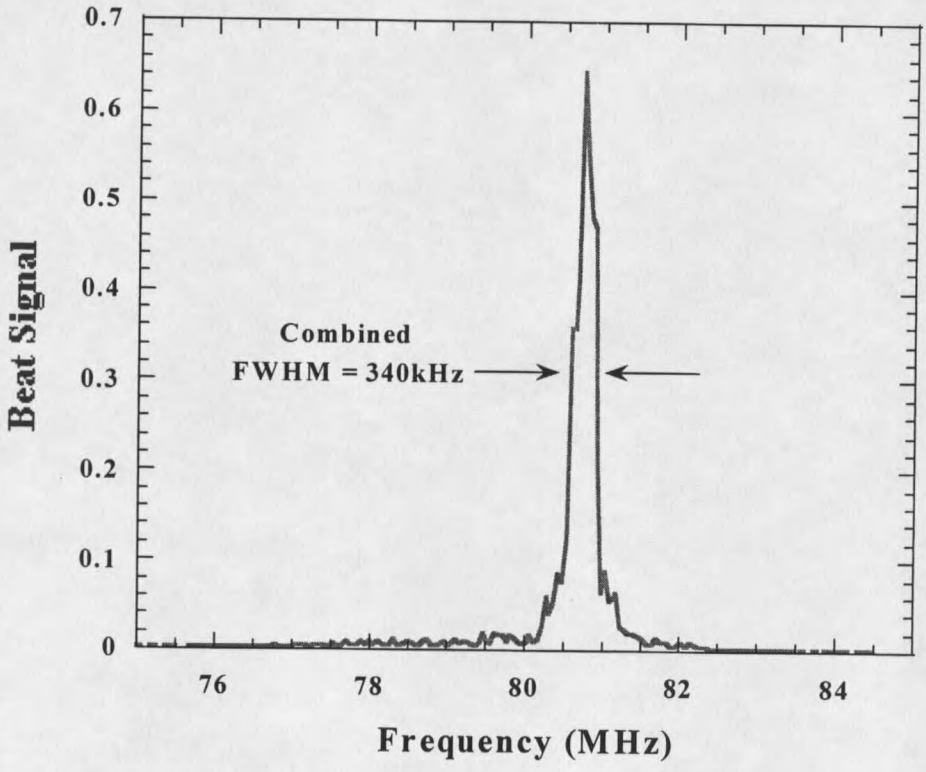


Figure 2.3.4. A combined linewidth of two ECDL's at 935nm measured using a heterodyne method. The linewidth of each laser must then be approximately 170kHz (over a 100ms time interval).

Since the combined linewidth of two identical Lorentzian line shapes is twice that of each individual linewidth, the actual linewidth of each 935nm ECDL is 170kHz over a 100ms interval. The frequency difference in the linewidth is approximately 2 parts per billion of the optical frequency! As a measure of the frequency stability of the laser, a 100 shot average linewidth was measured over 10s resulting in a 2.4MHz FWHM linewidth for each laser. This linewidth is actually much more practical to use since the water vapor absorption line will be measured over sweep times of 10ms to 3 minutes. The important conclusion to draw from these measurements is that the linewidth of the laser is significantly smaller than the 1GHz linewidth of the water vapor absorption line so that no deconvolution of the two lines will be necessary for the lidar system. Below is a photograph of the two lasers used to measure the heterodyne linewidth (Fig. 2.3.5).

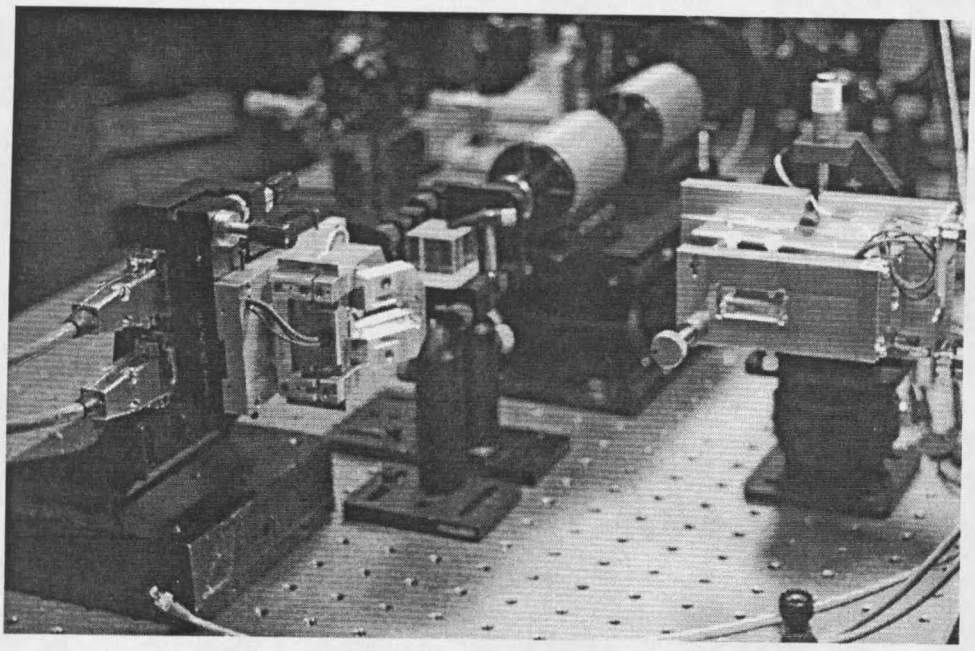


Figure 2.3.5. Photograph showing the overlap of the output beams of the two ECDL's used to measure the heterodyne linewidth. "Kelly" is on the left, "Herb" is on the right and the beam splitter and optical isolators are in the background.

Broad Wavelength Tuning Range

Thanks to the large gain bandwidth of the semiconductor laser, the 935nm ECDL is able to tune its narrow linewidth over a broad range of wavelengths. This coarse tuning is done manually by turning the fine-pitched screw in the prism plate with a 5/64" ball driver. One full rotation of the screw clockwise increases the wavelength by 3.71nm. The unique ability to tune the wavelength over 40nm is a distinct and important advantage ECDL's have over other lasers. For instance, a single batch of laser diodes can be used in identical external cavities to generate an array of stable, narrow linewidth sources at various wavelength within a 20-100nm range, depending on the center wavelength [37]. This saves time and is more cost effective than hand picking laser diodes, such as single mode distributive feedback laser diodes, that happen to emit at the

desired wavelength. It was only important for this project that the ECDL could be tuned to the strong water vapor absorption line at 935.68nm. The laser easily meet this requirement as shown below in figure 2.3.6.

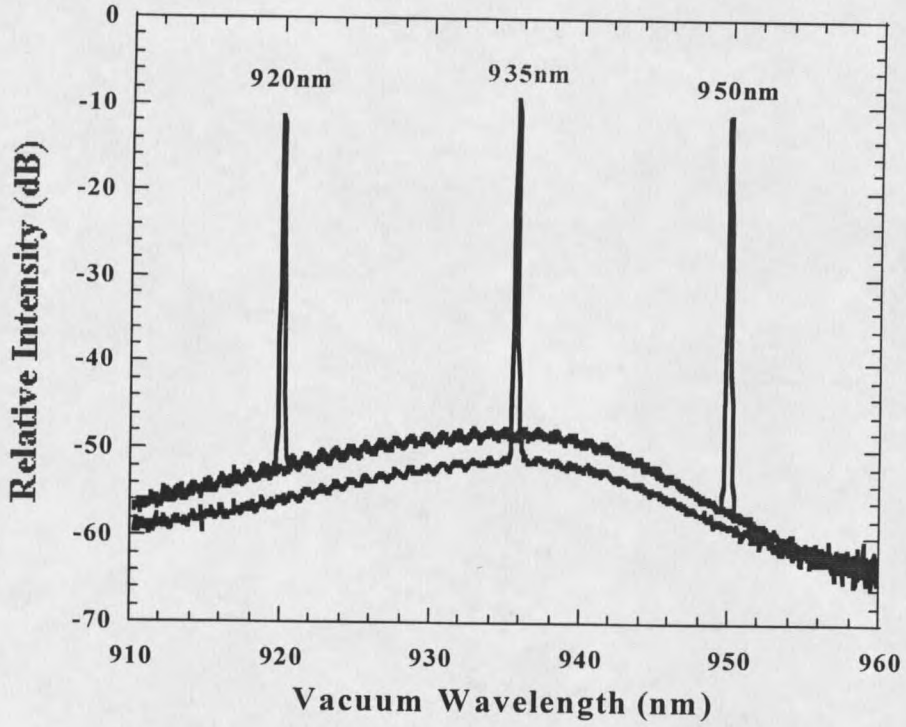


Figure 2.3.6. Measuring a few points of the broad wavelength tuning range using an optical spectrum analyzer. The ECDL produced 5.5mW of output power at I = 30mA and T = 20°C and is settable to any wavelength between 915 and 955nm.

The laser was not continuously tunable over this broad of a wavelength range. However the laser could be set to operate at any wavelength by slightly adjusting the temperature of the ECDL. This has the effect of adjusting the cavity length slightly so that the resonant wavelength is in phase in the external cavity. The temperature of the ECDL stabilizes quickly (<30s for a 1°C temperature change) owing to the reduced thermal mass of the cavity and powerful, 3A thermoelectric coolers. Notice that the

background curve drops when the laser is tuned to 935nm. The homogeneous characteristics of the gain medium in the laser allow the center of the energy band to attract carriers that will contribute to the stimulated emission more efficiently at the center wavelength than at the edges of the energy band. The "side-mode suppression ratio" is defined as the ratio of the optical power at the highest intensity mode relative to the next highest intensity mode. This important ratio is a good measure of how well the laser is performing. For instance the side-mode suppression ratio (SMSR) measures 45dB at 935nm and drops to 35dB at 920 and 40dB at 950nm. The SMSR drops even more the further the laser is tuned from its center wavelength until the gain bandwidth is exceeded, as will be discussed in a later section. In either case, the ECDL exceeds the side-mode suppression ratio required for the lidar system of 30dB.

Continuous Wavelength Tuning

The 935nm ECDL was designed to provide continuous wavelength tuning over a 10nm range by synchronizing the angle of the prism with a change in optical path length to the prism. This can be done mechanically by tilting the prism about a particular pivot point. It was calculated in section 2.2 that the pivot point must be located to within 18.7μm in order to get truly continuous, mode-hop free wavelength tuning over 10nm. By carefully adjusting the location of the diode laser in the external cavity, I was able to approach near continuous tuning as shown below in figure 2.3.7.

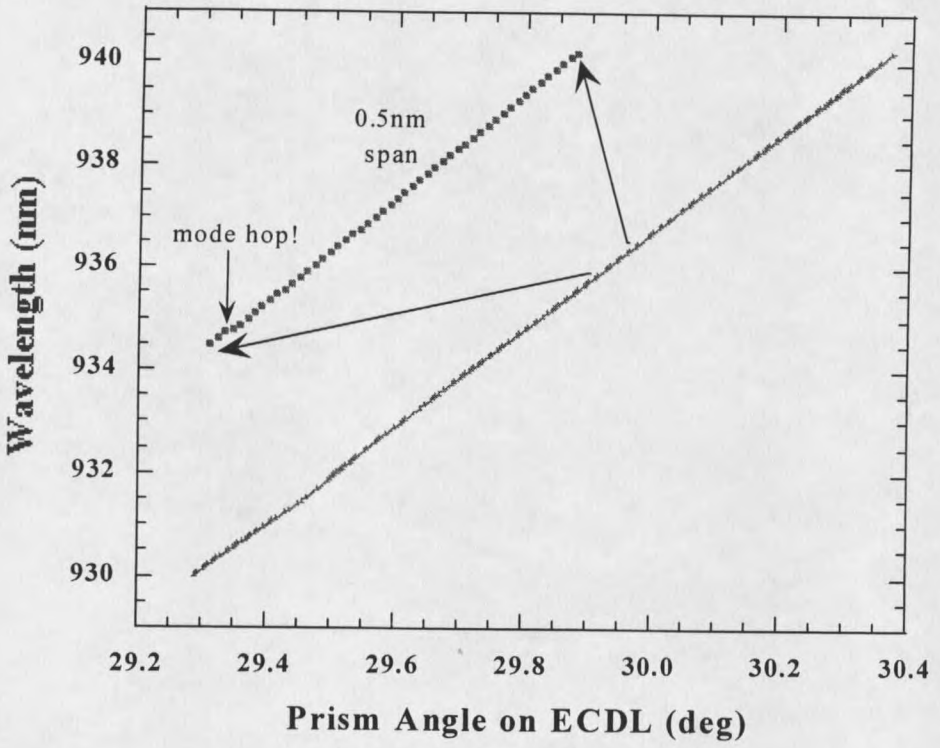


Figure 2.3.7. Near continuous wavelength tuning of the 935nm ECDL over 10nm.

In order to document the wavelength tuning over this large range to this accuracy, a computer driven stepper motor was used to advance the 3/16"x100 screw used to increase the angle of the prism plate while a WA1500 wavemeter from Burleigh Instruments recorded the wavelength. The motor was able to increase the wavelength 9.7pm per step generating over 1000 steps in the above scan!

Unfortunately, close inspection of the above scan reveals several mode hops. These hops appear as small discontinuities in the scan whose shift in wavelength is only 7.6pm (2.6GHz) as shown in the expanded section in figure 2.3.7. Mode hops remained present regardless of how carefully the pivot point was matched by micron adjustments to the position of the laser diode mount. The reason for these mode hops in the scan is still

under investigation. One explanation is that many of the mode hops are really just the excitation of a second spatial mode along the wide axis of the laser diode. The origin of the spatial modes is discussed in Appendix B. As the wavelength of the external cavity is tuned, "spatial mode hops" tend to drift in then drift right back out, returning the primary mode to its appropriate wavelength. In fact, it is possible to get both spatial modes to operate at the same time and be stable. One of the modes can be filtered out by blocking part of the prism with a card along its long axis. In contrast, actual longitudinal mode hops occur in discrete jumps from one cavity mode to another. The two modes never operate simultaneously and blocking the prism has no effect. The difference in these types of mode hops is shown below in figure 2.3.8.

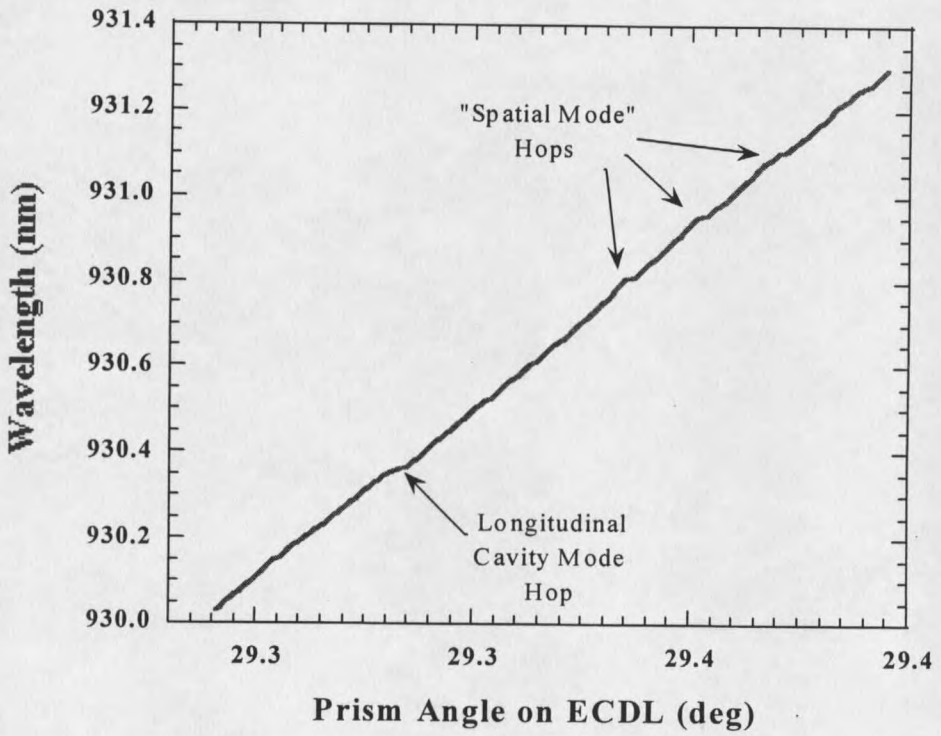


Figure 2.3.8. Identifying "spatial mode hops" from longitudinal mode hops during a wavelength scan.

The 935nm scanning Fiber Fabry-Perot interferometer was used to verify the difference between the mode hops. The "spatial mode hops" could be eliminated by narrowing the waveguide of the laser diode until it would only allow a single spatial mode. This would remove a majority of the mode hops seen in figure 2.3.7, eliminating the confusion of these hops, and might allow further tuning of the pivot point. As a source for the lidar transmitter, the laser has demonstrated its capability to tune continuously over hundreds of picometers which is more than necessary to scan across water vapor absorption lines.

Fine Wavelength Tuning Range

Once the ECDL is set to the desired wavelength such as 935.68nm, it can be fine tuned or even scanned electronically about 70pm (24GHz) using the PZT positioned under the fine-pitched screw used for coarse tuning. A function generator or computer driven programmable voltage supply can be amplified 15 times by the PZT driver used to operate the low voltage PZT stack. The 20mm stack is advertised to stretch 17μm over an applied potential of 150V. This provides about 1.7pm/volt of continuous wavelength tuning as shown below in figure 2.3.9.

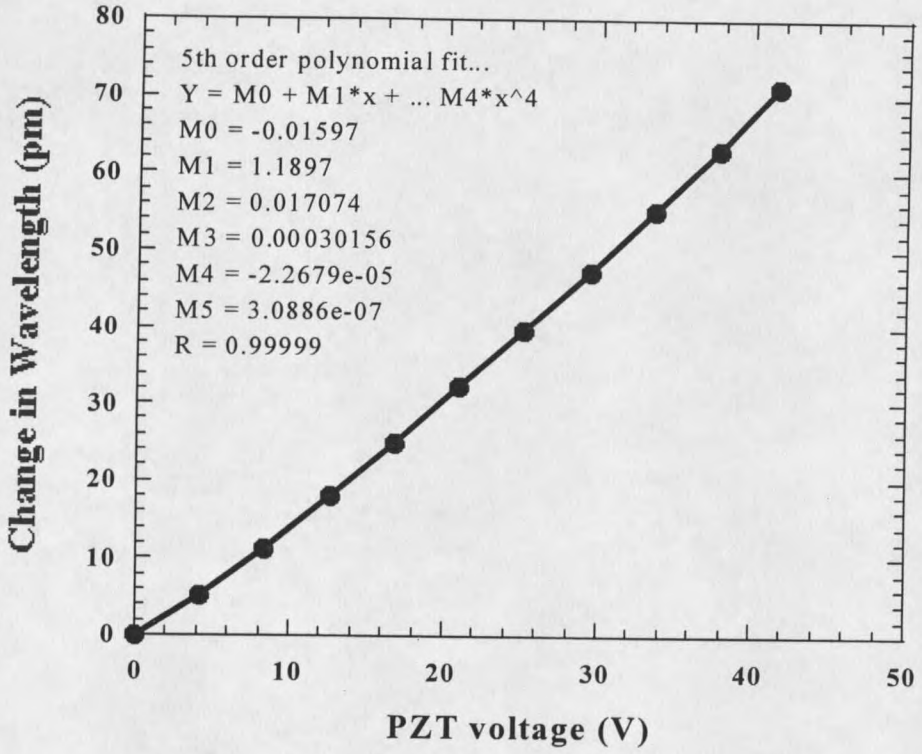


Figure 2.3.9.. The wavelength changes by approximately 1.7pm/volt applied to the PZT located under the prism plate on the ECDL. The laser was operated at I = 23mA at T = 22.8°C starting at λ = 935.6530nm.

The ECDL is able to scan up to 100pm (34GHz) continuously, single mode without a mode hop using the PZT. Only 80pm was needed to completely scan the widest pressure broadened line at 935 and an even smaller scan of 50pm was needed at low pressures. A fifth order polynomial is used to fit the near-linear curve in order to calibrate the change in wavelength with the PZT voltage. This fit agrees with the actual measured wavelength of the scan to within the accuracy of the WA1500 Burleigh Wavemeter of $\pm$ 0.2pm [38]. Once a start wavelength is measured, the fit can be used to calculate the rest of the wavelengths in the scan so that each wavelength does not have to be measured with the wavemeter. This allows the laser to scan quickly offering a

"frequency window" that can be used to search for absorption lines in real-time, for instance. This type of wavelength calibration was successfully used for all of the scans of the 935.68nm water vapor absorption line. In addition, the center wavelength of the scan can be precisely adjusted using a DC bias on the PZT driver.

Side-Mode Suppression Ratio

The "side-mode suppression ratio" is defined as the ratio of the optical power at the highest intensity mode relative to the next highest intensity mode. A reduction in the side mode suppression ratio occurs when the side modes begin competing with the main mode for more gain. This mode competition can become increasingly fierce if the main mode experiences any additional loss from the external cavity or the wavelength of the main mode is forced to the edge of the gain curve. As a result, this important ratio is a good measure of how well the laser is performing. For instance, misalignment of the beam folding prism or poor collimation of the beam will increase the loss to the main mode (by reducing the amount of feedback) and will often reduce the SMSR by 10dB or more.

The SMSR tends to drop as the laser is tuned farther from the center wavelength of the laser diode's gain curve. It becomes more and more difficult to attract carriers from the center of the energy bands to the outer edges of the energy bands where the stimulated emission generates the chosen wavelength. A plot showing the dependence of the SMSR on the set wavelength appears below (Fig. 2.3.10).

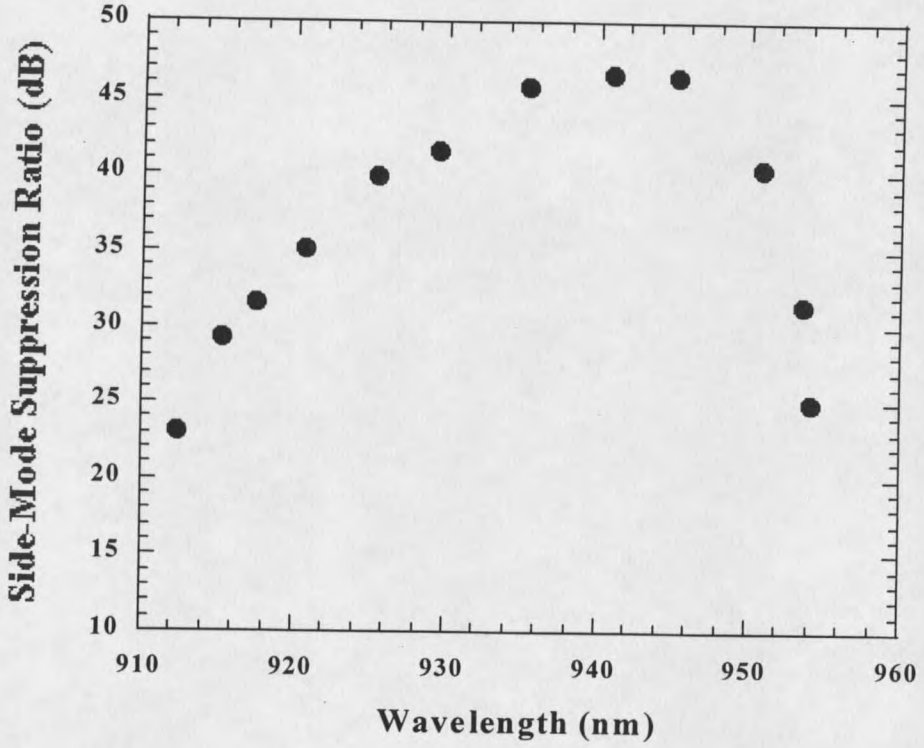


Figure 2.3.10. Dependence of the side-mode suppression ratio on the set wavelength of the ECDL. The laser was operated at I = 25mA at T = 24°C.

It is necessary for a laser transmitter to have a SMSR $\geq$ 30dB to make accurate lidar measurements. This ensures the single, narrow linewidth, wavelength probe is 1000 times more intense than any background radiation emitted from the laser. Therefore the on line/off line measurements of the water vapor absorption line can theoretically be accurate to one part in 1000. The output from the 935nm ECDL has a SMSR $\geq$ 40dB over 10nm centered at 935nm which exceeds the 30dB requirement.

Power and Wavelength Stability

The long term power and wavelength stability of the output of the ECDL is also very important to characterize. For instance, a change in output power as the laser is scanned back and forth over the water vapor absorption line may erroneously appear as a change in the overall water vapor concentration. It was required that the total output power of the ECDL reach 10mW in order to saturate the gain of tapered semiconductor amplifier that was to be seeded by the laser. Once again the laser exceeded its expectation delivering over 11mW at 935.68nm! The output power of the ECDL depends strongly on the DC current injected into the laser diode. It also depends on the effective reflectivity of the output mirror, or optical feedback, which is a function of the design of the cavity and how well it is aligned. For this reason, a power versus current (PI) curve is an informative way to check the health of the ECDL (Fig. 2.3.11).

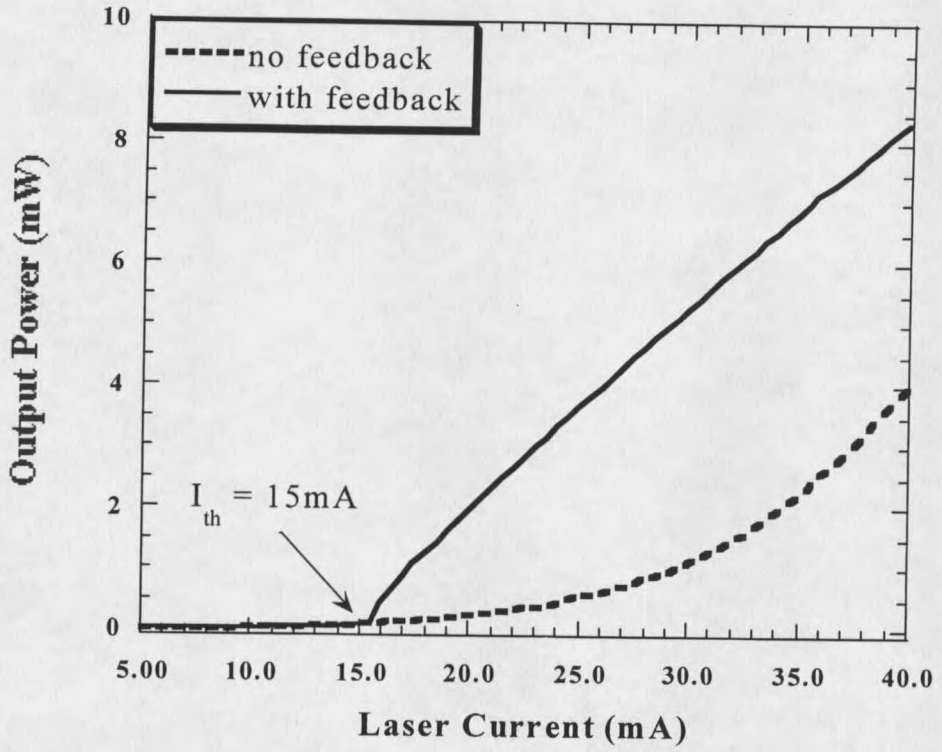


Figure 2.3.11. Power versus current curve for the 935nm ECDL. Lasing begins at an injection current of 15mA, defining the threshold current for the laser.

With sufficient feedback, the lasing suddenly begins at a characteristic current know as the "threshold current." The optical alignment of the external cavity is optimized when the threshold current is minimized. Notice that when the feedback from the external cavity is removed (by blocking the prism) the power gradually increases with the current resulting in a less obvious threshold current. This is an indication that a low reflective AR coating has been applied to the front facet of the laser diode.

With adequate wavelength stability, we can avoid locking the frequency of the laser to the center or edge of the water vapor absorption line which will simplify the lidar transmitter. Frequency locking the laser to the absorption line is not necessary if the

wavelength drifts less than one part in 100 of the low pressure (0.007atm) absorption linewidth, or about 10MHz at over a several minute integration time for the lidar system. A test of the power and wavelength stability was done on the ECDL under real lidar transmitter conditions. The PZT was continuously scanning its wavelength at 25Hz over the 935.68nm water vapor absorption line while the output power was detected and recorded by the computer at the on and off line points. A DC current of 23mA powered the laser diode and the temperature of the ECDL was controlled to 23.1°C for the 10hour, overnight test. The wavelength was measured at the beginning and ending of the 10 hour test and is known to follow the power fluctuations from previous tests. The results are plotted below (Fig. 2.3.12).

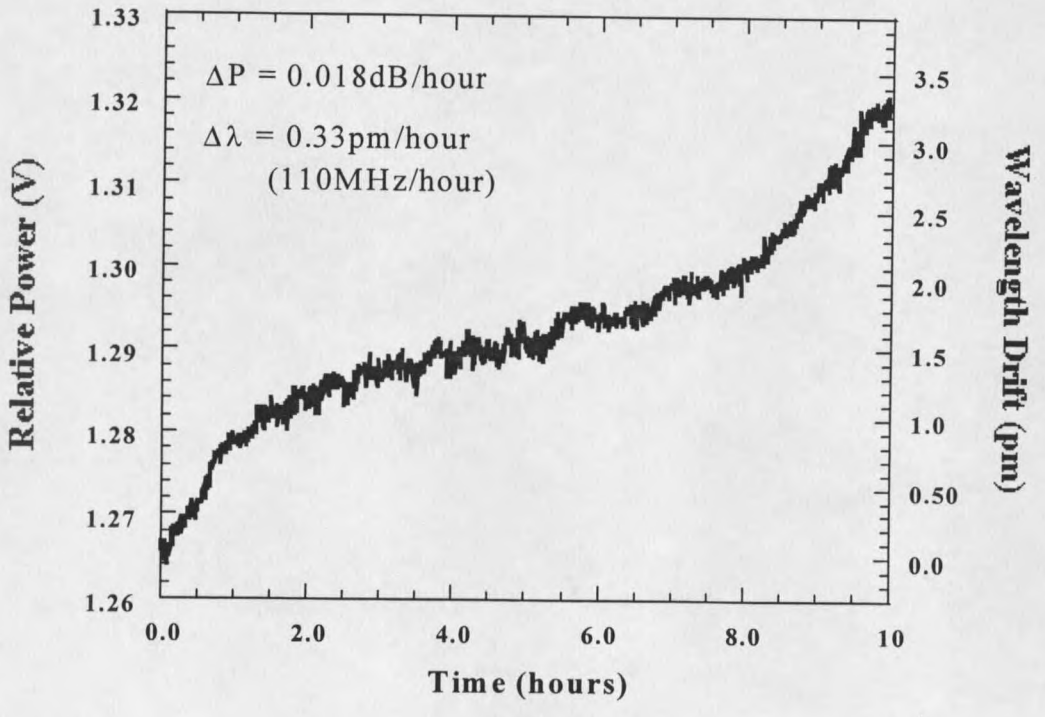


Figure 2.3.12. Power and wavelength stability of the 935nm ECDL over 10 hours under real lidar transmitter conditions.

The total power drifted about 4% over 10hours, or only a fraction of a percent over one hour. Under the atmospheric conditions on Mars, we expect to see around 50% absorption of the lidar return and hope to resolve the absorption to within $\pm$ 1%. Therefore the power stability of the ECDL is more than adequate. The wavelength drifts about 110MHz/hour or less than 2MHz/minute. The drift can be attributed to "creep" or deformation in the PZT from being operated at an average potential of 52V and small thermal variations of the aluminum parts of the external cavity. This drift allows the lidar system to integrate its return signal for up to 10 minutes before the center wavelength of the scan will begin to drift off the peak of the absorption line. This wavelength stability is certainly acceptable for a bread-board lidar system where the center wavelength can be monitored and adjusted by the user. However it will be necessary to stabilize the actual 935nm source to the water vapor absorption line for a remote instrument intended to operate on the surface of Mars for long time periods.

Beam Profile

It is important to characterize the output beam profile and its polarization in order to match the input parameters for seeding the tapered, semiconductor amplifier and optimizing the coupling efficiency. The output of the laser diode is highly divergent and asymmetric as it exits the small 0.5 x 3μm aperture (recall figure 2.1.1). The beam is so divergent that a special instrument was developed in the lab that could measure the beam profile. Traditional methods, such as CCD cameras, could not capture the entire beam [39,40]. The computer controlled device scans a detector across the horizontal axis of the

beam at a radius of 76mm from the laser output and records the intensity creating a far field profile. The scan head can then be rotated 90° to measure the vertical profile of the beam. The far field profile of the 935nm laser diode is shown below in figure 2.3.13.

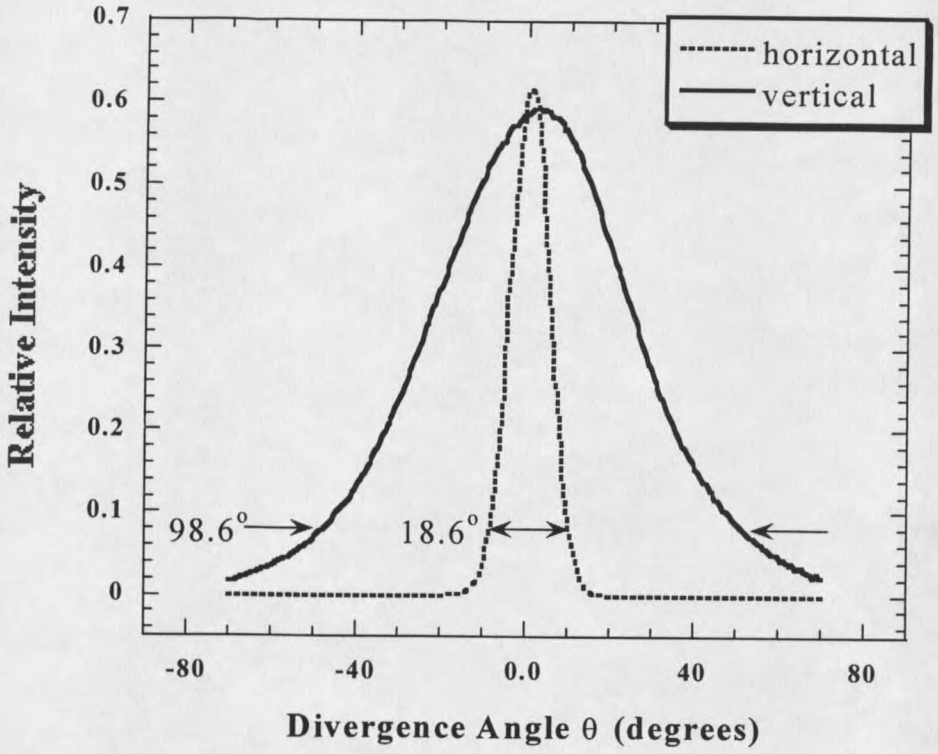


Figure 2.3.13. Far field beam profile of 935nm Fabry-Perot laser diode. The laser diode was driven with a DC current of 30mA (twice its threshold current) and temperature controlled to 20°C. The horizontal direction scans along the wide 3μm axis of the laser waveguide.

The laser diode was positioned such that the wide, 3μm dimension of the aperture lies horizontal. Notice that this "slow" axis of the beam is much less divergent than the vertical, "fast" axis of the beam. This will give rise to an oval shaped beam once it is collimated. The half angle at $1/e^2$ intensity points along the fast angle is $\theta_{max} = 98.6°/2$ which can be completely captured by a lens whose numerical aperture is:

$$NA_{fast} = \sin(\theta_{\max}) \rightarrow 0.76 \qquad 2.3.1$$

This numerical aperture is very large and it is difficult to find a lens that will completely accept 100% of the vertical axis of the beam. The f = 4.5mm aspheric lens was chosen primarily because an identical lens was used to couple light into the tapered semiconductor amplifier. The 4.5mm lens has NA = 0.55 which will accept most of the fast (vertical) axis and all of the slow (horizontal) axis of the laser diode output. This lens was later replaced with a f = 3.1mm, NA = 0.68 lens which successfully gathered more light and provided better optical feedback from the diode. A photo of the collimated output beam from the 935nm ECDL was captured on a CCD camera 30cm from the laser using the f = 4.5mm, 0.55NA collimating lens (Fig. 2.3.14).

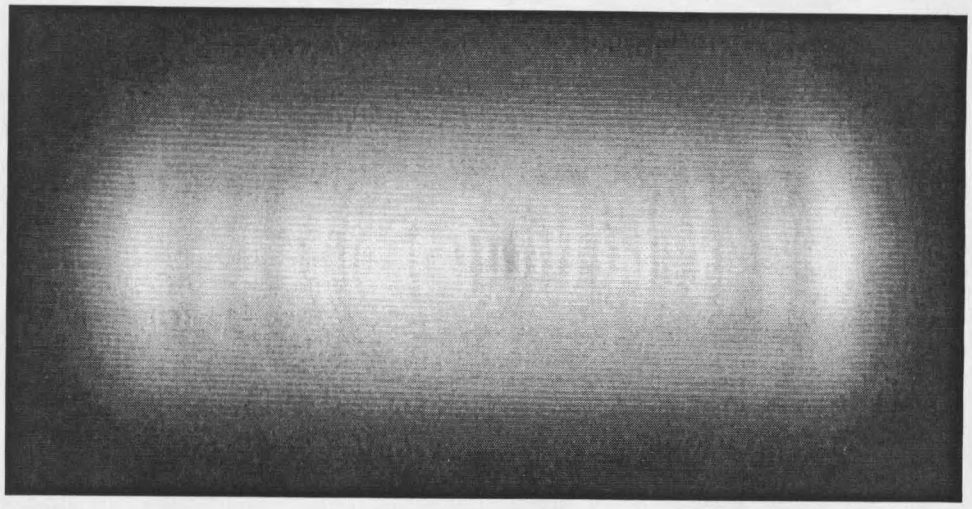


Figure 2.3.14. Photo of collimated beam using the f = 4.5mm, 0.55NA aspheric lens captured on a CCD camera. The beam has an aspect ratio of 3.16:1.

The beam measures 5.05 x 1.60mm at the $1/e^2$ intensity levels resulting in an aspect ration of 3.16:1. This aspect ratio matches the input of the tapered semiconductor amplifier and should provide optimal coupling. Notice that a few vertical fringes appear

at the left and right edges of the beam. These fringes are caused by the vignetting of the beam on the aperture of the lens since the numerical aperture is not large enough to capture the entire axis of the beam.

The beam profiles in figure 2.3.12 also shows that each axis is a lowest order spatial mode with a gaussian profile. This should provide a nice collimated beam along either axis. Unfortunately, the virtual source point along the slow, horizontal axis lies slightly behind the front facet of the laser inside the waveguide. In contrast, the virtual source point for the vertical, fast axis of the beam lies on the front facet. This offset in the virtual source points for each axis results in a slight astigmatism that allows only one of the axis to be truly collimated using only a single element lens. I found that by adjusting the f = 4.5mm collimating lens until the width of the fast axis is reduced by a factor of 2 at 3m from the laser diode, the slow axis becomes well collimated. This setting led to the best performance of the ECDL for two reasons. First, by slightly focusing the fast axis, the optical feedback has a slightly reduced spot sized as it reenters the front facet, improving chances for better coupling efficiency. Second, by collimating the slow axis, the optical feedback approaches the front facet with flat phase fronts. Flat phase fronts have less opportunity to stimulate higher order spatial modes that my be supported by the wide axis of the waveguide [see Appendix B]. Troublesome, higher order spatial modes can generate a spectral output that is multimode and confusing. Additional fine tuning the beam collimation is done by making small adjustments to the lens as the laser is running and maximizing the SMSR of the output.

It is also important to measure the polarization of the output beam of the ECDL in order to match its orientation to that preferred by the tapered semiconductor amplifier. In general, semiconductor devices tend to select TM polarized light along the wide axis of their waveguide because it is less confined than the narrow axis of the waveguide. Therefore the polarization of the input beam to the tapered amplifier must lie along the wide axis of its waveguide for optimal amplification. To measure the polarization, the output beam of the ECDL was passed through a Glan-Thompson polarizer with a polarization selection ratio greater than 2000:1. The transmitted optical power was measured using a power meter as the prism was rotated from 0 to 90° (Fig. 2.3.15).

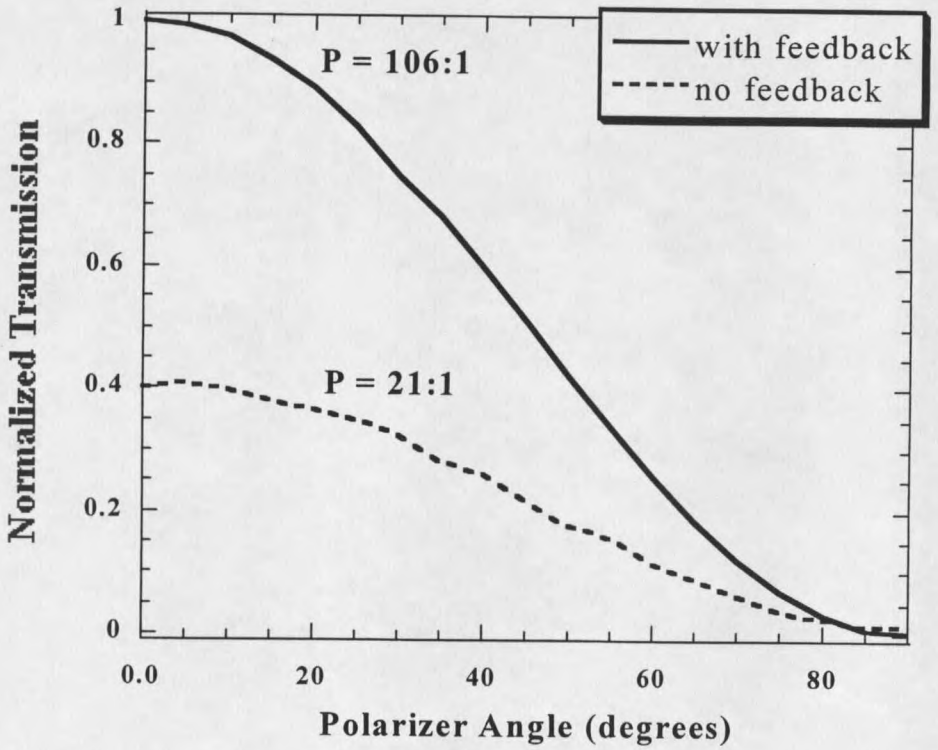


Figure 2.3.15. Output polarization of the 935nm ECDL.

With optical feedback from the external cavity, the output is linear polarized with a polarization ratio of 106:1 along the slow, less divergent axis of the beam (refer to figure 2.1.1). That is, the polarization is vertical and lies along the short dimension of the beam in figure 2.3.14. Notice that the output seems to be less polarized when the optical feedback from the external cavity is removed. Recall from figure 2.2.6 that the grating is very efficient at diffracting the p-polarized light into first order where it is lost when the prism is blocked. This will reduce the polarization ratio of the p to s-polarized light measured at the zeroth order output. By unblocking the prism, the p-polarized light is reflected back to the laser diode where it can be amplified. In this sense, the external cavity helps select the output polarization of the ECDL. Incidentally, these results agree very well with the expected transmission of polarized light through a polarizer rotated from 0 to 90°.

$$T(\theta) = \cos^2(\theta) \qquad 2.3.2$$

This $\cos^2(\theta)$ dependence of the transmission of polarized light through a polarizer was first discovered by Etienne Malus in 1809! [28]

Summary of Laser Performance

A detailed characterization of the output of the 935nm ECDL reveals that its performance meets or exceeds all the requirements needed to be the master oscillator for the proposed miniature water vapor lidar transmitter. A list of the requirements and actual measured performance of the laser is listed below in table 2.3.1.

Table 2.3.1 Summary of laser requirements and actual performance.

Output Parameter	Required Performance	Actual Performance
CW Output Power	10mW	11mW
Wavelength	935.7nm	920-950 nm
Continuous λ scan	30pm (10GHz)	70pm (25GHz)
Mode suppression ratio	30dB	> 40 dB
Spectral linewidth	< 25MHz single mode	170 kHz single mode
Beam profile	3:1 aspect ratio, $TEM_{0,0}$	3:1 aspect ratio, $TEM_{0,0}$
Polarization	linear 100:1	linear 106:1

Although it is unlikely this particular laser would be flown on the next mission to Mars, it will be extremely useful in characterizing the 935.68nm water vapor line and demonstrating a breadboard laser transmitter whose output would be suitable to measure the water vapor in the Martian atmosphere. It will help pave the way for a miniature water vapor lidar system that will be used on a future Mars Lander mission.

CHAPTER 3

WATER VAPOR LIDAR TRANSMITTER USING THE EXTERNAL CAVITY DIODE LASER

3.1 Introduction and Motivation

The 935nm ECDL met or exceeded all of its output requirements for a stable, single, narrow linewidth tunable seed laser to be used as the master oscillator of the water vapor lidar transmitter. Now its low power, CW output must be amplified and pulsed in order for the lidar receiver to measure the range-resolved return signal scattered from the atmosphere up to several kilometers of altitude. Like the ECDL, the amplifier must be small, lightweight and power efficient to be considered as an instrument for the Mars Lander. This chapter focuses on the development of the pulsed power amplifier of the proposed lidar transmitter; the flared semiconductor amplifier.

Why the ECDL Alone is Not Enough

We expect only 1 out of every 10,000 photons emitted from the laser transmitter to be scattered back to the lidar receiver by the Martian atmosphere. To make matters worse, the optical power drops off with distance r as $1/r^2$ and the number of available particles that can back scatter the light quickly decreases with altitude as the atmosphere

becomes less dense. Until very recently, only large, high power pulsed lasers were considered capable of transmitting enough power (10-1000mJ per pulse) for atmospheric lidar. However, with the development of high quantum efficiency, photon counting, semiconductor detectors and very narrow band filters to filter out all but the transmitter wavelength, less optical power from the transmitter is needed. The "lidar equation" (section 5.2) reveals that roughly 1 photoelectron count for every 20mW of optical power from the transmitter will be detected from an altitude of 5km per second. This level of detection follows random point processes and a meaningful signal must be inferred from Poisson statistics. To avoid this complication, we will try to record a minimum of 10^4 photoelectrons per range bin. The receiver would have to integrate over 2 hours and 45 minutes before it would sum up 10^4 photoelectrons for a 20mW pulsed transmitter! This would limit the instrument to measuring only the long term fluctuations of the water vapor in the atmosphere. By raising the transmitter peak pulse power to 200mW, the receiver would only have to integrate for about 17 minutes allowing us to measure the important short term dynamics of the atmospheric water vapor. For this reason the output of the ECDL must be amplified a minimum of 10 to 100 times.

The output must also be pulsed so that each return photon can be sorted into a range bin determined by its time of flight from the transmitter to the receiver. A common method to generate the pulses is to use an electro-optic modulator [41]. This not only adds another component to the lidar transmitter and usually operates at high voltages, but it also throws away light instead of amplifying it. A second alternative is to simply pulse

the current to the ECDL. Unfortunately this generates a frequency chirp in the laser output causing the multimode spectral output shown below in figure 3.1.1.

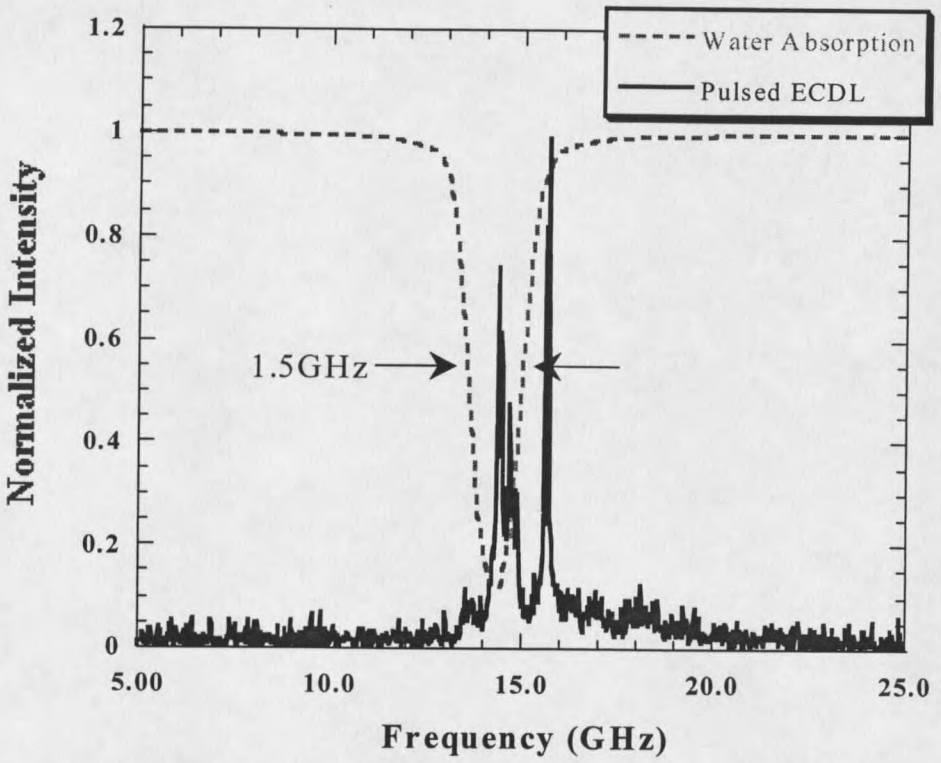


Figure 3.1.1. Pulsing the laser drive current to the ECDL causes frequency chirp and multimode operation in the output. The low pressure 935.68nm water vapor absorption line is also shown to demonstrate the severity of the chirp.

The current was driven from the laser's 15mA threshold current to a peak current of 32.7mA over a 1μs pulse width at a repetition rate of 3.9kHz. These are the pulse conditions needed for the actual lidar system. As the current is modulated from threshold current to 32.7mA, the carrier density increases causing a decrease in the index of refraction inside the waveguide of the laser diode. This changes the overall net cavity length causing the resonant frequency to vary. The result is a chirped, multimode output shown above. The frequency chirp is on the order of the absorption linewidth which is

unacceptable as a narrow, single line probe for the atmospheric lidar transmitter. The third alternative is to inject the CW output from the ECDL into a flared semiconductor amplifier. This amplifier can both amplify the injected beam, duplicating the single narrow linewidth wavelength of the ECDL, and pulse its output with no measurable frequency chirp.

3.2 Amplify and Pulse Using a Flared Semiconductor Amplifier

The most energy efficient way to boost the optical power and pulse the output from the laser transmitter is to inject the ECDL beam into a flared semiconductor amplifier [42]. The collimated beam from the ECDL is focused into the rear facet of the amplifier using an f = 4.5mm aspheric lens, just like the one used to collimate the laser diode in the external cavity (Fig. 3.2.1.)

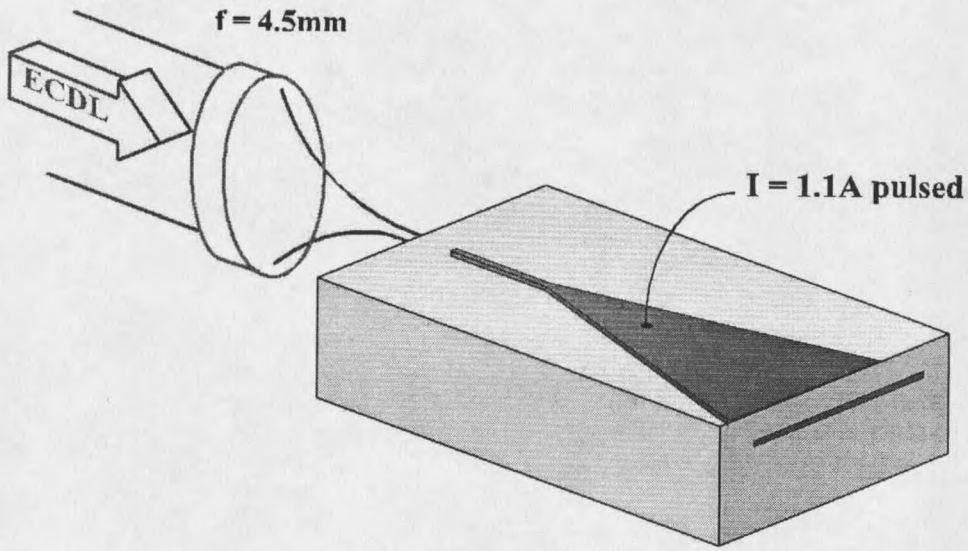


Figure 3.2.1. Light from the 935nm ECDL is injected into a flared semiconductor amplifier where it can be amplified and its output pulsed.

The active region of the amplifier is a single quantum well of InGaAs imbedded in an AlGaAs heterostructure similar that of the laser diode in the ECDL. By using these materials for the growth of the device, the gain of the amplifier was centered about 933nm and had a 10dB gain bandwidth of roughly 18nm at a pulsed drive current of 1.1A. Both facets receive an AR coating of $R < 10^{-3}$ so the devices does not lase on its own. This allows us to use the device as a single pass amplifier for the injected beam

from the 935nm ECDL. The waveguide travels the full 1.2mm length of the device and is less than 1μm tall. The input aperture of the waveguide measures 4μm wide along the lateral axis and flares to 130μm at the output aperture. The unique flared waveguide allows the device to emit a high power, diffraction limited output beam. Light from the 935nm ECDL is injected into the 4μm aperture of the device and is amplified as it propagates down the waveguide, when a large current is injected into the device. The expanding waveguide allows the energy density of the beam to remain constant as it is amplified while traveling towards the wide output aperture. This provides a constant gain for the light along the length of the waveguide so "hot spots" or "cool spots" appear and reduce the optimum amplification. The wide output aperture of allows the high power beam to exit without damaging the facet. The flared design also allows many more electronic carriers to participate in the stimulated emission process by dispersing them over the large area of the waveguide. Although the device I used in this project reached output powers in excess of 0.5W, similar devices have emitted greater than 5W CW optical power! [43] The angle of the flared waveguide is specially designed so that the beam leaving the 4μm wide index guided region is allowed to freely diffract along the length of the power amplifier. This feature, along with the effective constant gain of the waveguide, allows the output beam to be diffraction limited. This is especially important for collimating the output beam as precisely as possible so that it suffers the least possible divergence as it is pointed into the atmosphere. The power amplifier was soldered to a standard C-mount and attached to an aluminum heat sink specially designed for this project (Fig. 3.2.2).

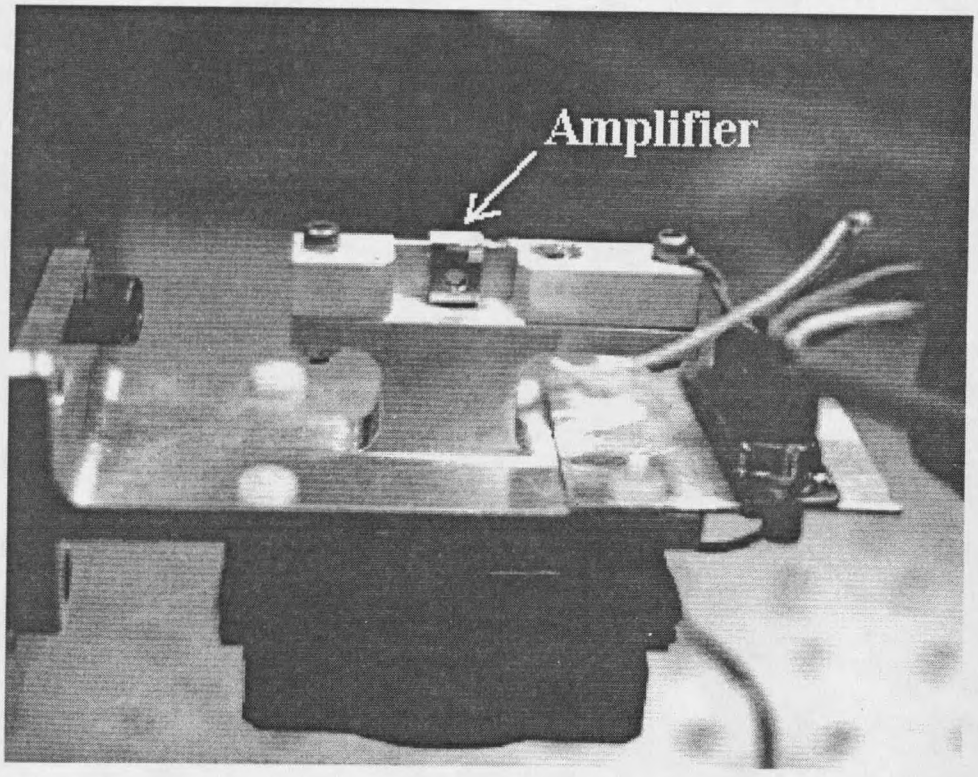


Figure 3.2.2. Photo of the flared semiconductor amplifier mounted to its temperature controlled aluminum heat sink.

Coupling Light Into and Out of the Amplifier

The 1 x 4μm input aperture of the semiconductor amplifier made coupling the light from the 935nm ECDL into the device even more challenging than coupling light into a single mode optical fiber. A single f = 4.5mm, 0.55 numerical aperture, AR coated aspheric lens was used to couple the light into the rear facet of the amplifier. This lens was chosen for its high numerical aperture that closely matched that of the narrow, 1μm axis of the input aperture. The output optics are slightly more complicated. The lateral axis of the beam appears to have originated from a virtual point source that lies deep inside the wide axis of the flared waveguide, well behind the output facet. The vertical

axis of the beam exiting the very narrow 1μm dimension of the output aperture has a virtual point source that appears to originate from the surface of the facet. The variation in the lateral and vertical virtual point sources causes a large astigmatism in the output beam. This can be corrected using an f = 150mm cylindrical lens as shown below in figure 3.2.3.

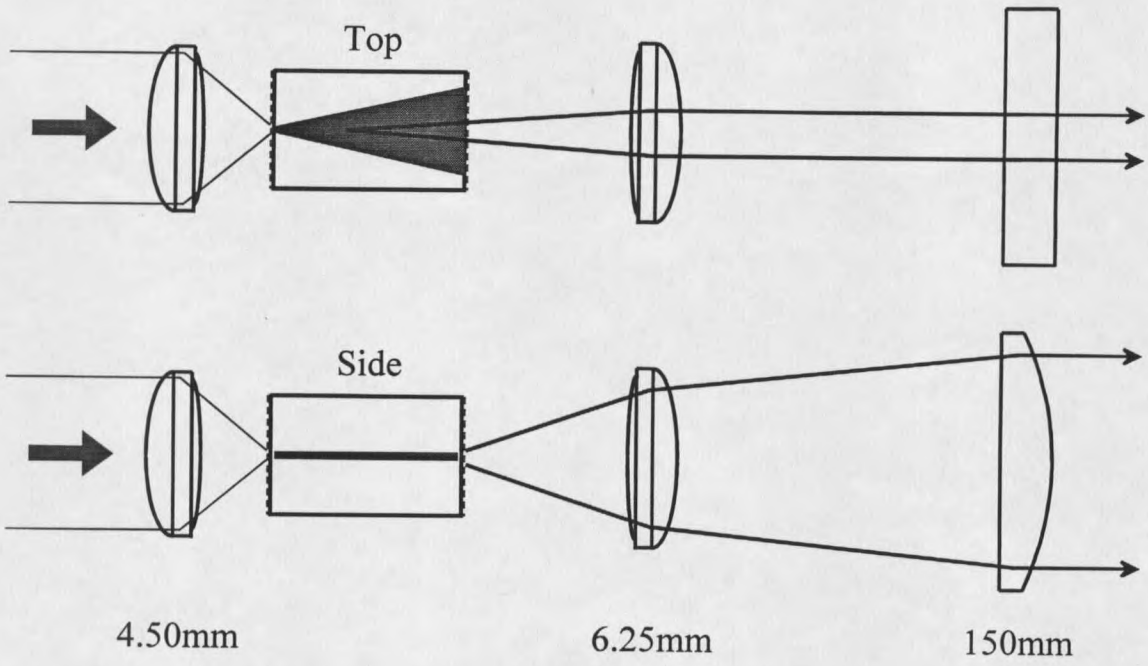


Figure 3.2.3. Optical schematic for the flared semiconductor amplifier. Light is injected from the left from the 935nm ECDL and its output is collimated in both the lateral (top view) and vertical (side view) using a spherical and cylindrical lens.

In this optical setup, an f = 6.25mm, AR coated aspheric lens was used to collimate the slowly diverging, lateral axis of the beam. An f = 150mm AR coated cylindrical lens is used to complete the collimation of the fast diverging, vertical axis of the beam while unaffecting the collimation of the slow axis of the beam [44]. For the actual lidar transmitter, the thin lateral axis of the beam would be expanded to match the beam

diameter of the tall vertical axis of the beam using an anamorphic prism pair. Both axes of the beam would then be equally expanded to minimize the divergence of the transmitter beam. However, the tall, thin profile of the collimated output beam would work fine for water vapor measurements made in the lab. The optical setup for injecting light into the flared amplifier is shown below (Fig. 3.2.4).

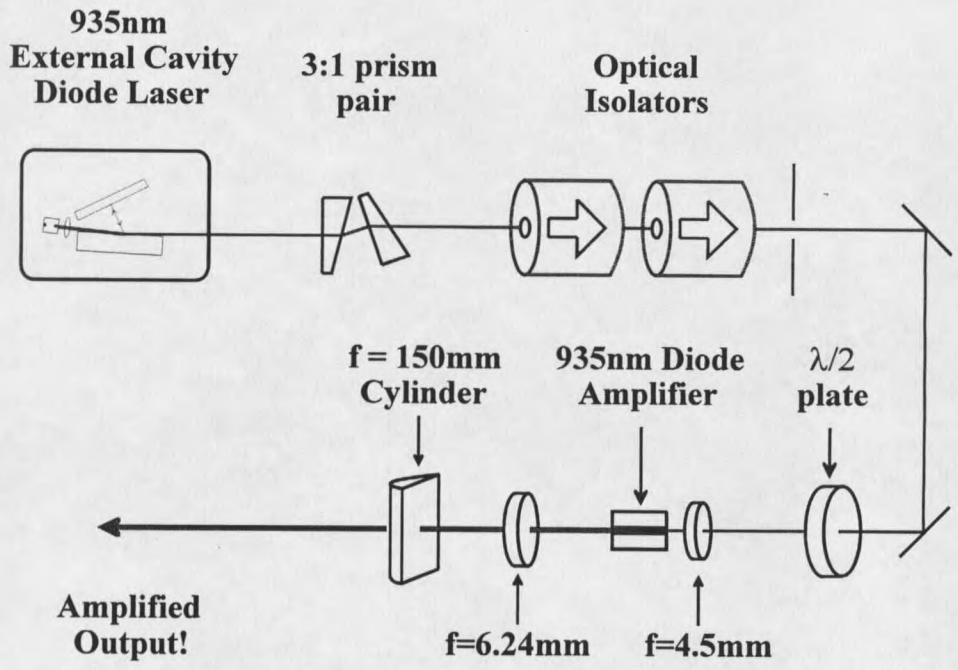


Figure 3.2.4. Schematic for seeding the optical amplifier with the 935nm ECDL.

A 3:1 anamorphic prism pair is used to reduce the tall axis of output beam from the ECDL in order for the beam to pass through the 5mm aperture of the optical isolators. The isolators are necessary to block any light emitted from the input facet of the amplifier, back into the ECDL, affecting its stability. As the beam from the ECDL propagates through the pair of isolators, its polarization is rotated 90°. This polarization is then rotated another 90° using a half wave plate in order to align the polarization along

the lateral axis of the flared amplifier. All optics were designed to reduce the transmission or reflection loss at 935nm in order to deliver as much light from the ECDL as possible to the flared amplifier. A 78% transmission was obtained through the network of optics between the ECDL and amplifier.

The percentage of light from the ECDL that was coupled into the semiconductor amplifier was measured using the amplifier as a optical detector. Instead of applying a current, a 100.9 ohm resistor was placed across the connections to the amplifier. Light coupled into the waveguide would generate a photocurrent that would pass through the resistor and could be detected by a precision voltmeter. The injected power can be determined from the measured photocurrent by [45]:

$$P_{injected} = \frac{h\nu}{e\eta_{qe}} i_{pc} \qquad 3.2.1$$

The photon energy $h\nu$ = 1.33eV is based on the ECDL wavelength of 935nm and e = 1.602×10^{-19} represents the charge of an electron in coulombs. A quantum efficiency of $\eta_{qe} = 1$ implies that every photon generates a photoelectron that can be measured. This will provide the most conservative estimate of the injected power from the measured photocurrent. The photocurrent, i_{pc} is actually determined from Ohms law by measuring the voltage drop across the 100.9 ohm resistor. Typical coupling efficiencies of 40% were achieved resulting in over 3mW of power injected into the flared amplifier.

CW Operation

The CW and pulsed performance of the flared amplifier was characterized by measuring the amplified output of the experimental setup shown above in figure 3.2.4.

An optical spectrum analyzer was used to measure the output spectrum of the amplifier with and without being seeded by the external cavity laser (Fig. 3.2.5).

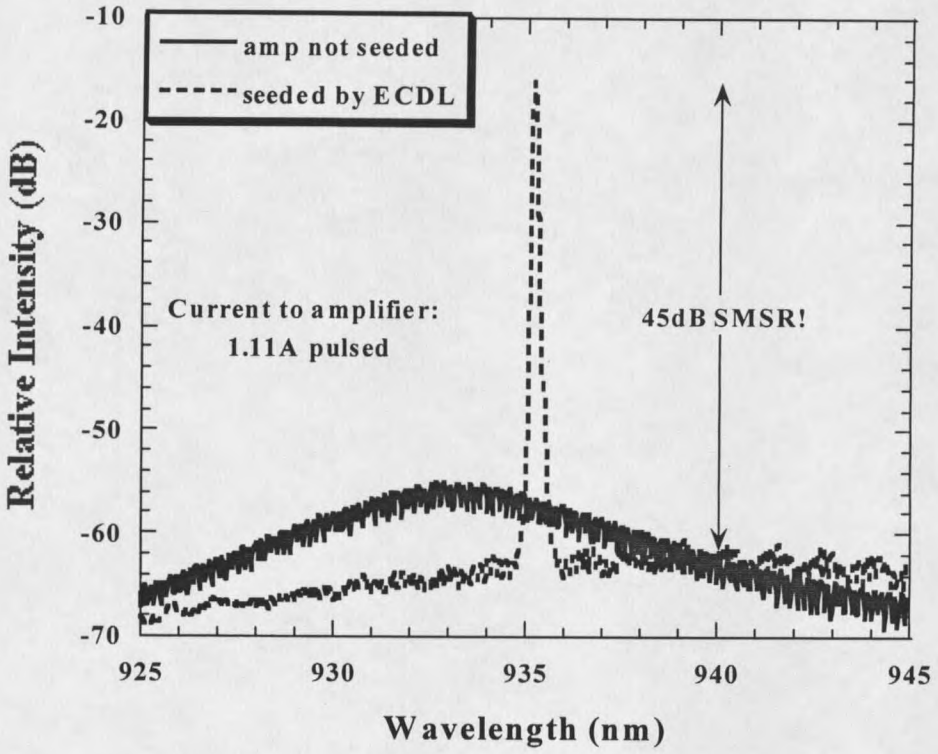


Figure 3.2.5. The spectral output of amplifier narrows to a single wavelength which matches that of the injected light when seeded by the ECDL. A side mode suppression ratio of 45dB was measured.

The amplifier provides a smooth, broad, 10dB gain bandwidth of 18nm when it is not being seeded by the ECDL. This indicates the AR coating on the facets of the flared amplifier are good enough to keep it from lasing on its own. The gain bandwidth is centered at 933nm, but is broad enough to amplify an injected wavelength from 926nm to 944nm. When the amplifier is seeded by the ECDL, it matches the seed laser's wavelength exactly and provides an excellent side mode suppression ratio of 45dB.

To quantify the single pass gain of the flared amplifier, a PI curve similar to figure 2.3.11 was measured for the seeded amplifier. The amplified output power was monitored as the input power was increased. The input power was increased by simply increasing the DC drive current to the laser diode in the ECDL. The resulting PI curves are shown below in figure 3.2.6.

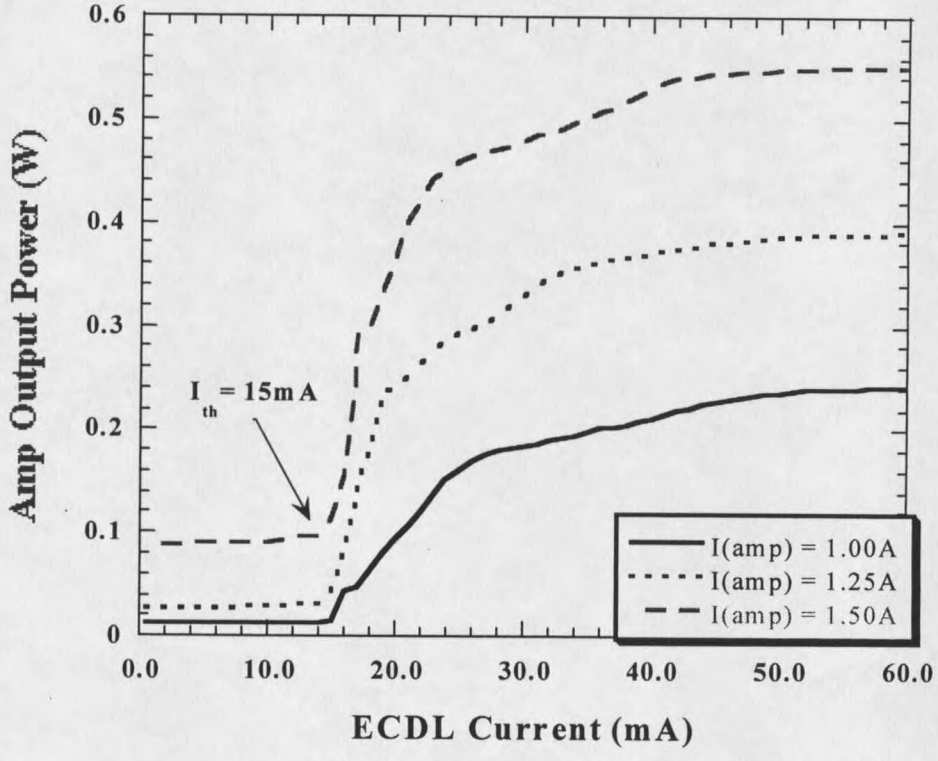


Figure 3.2.6. PI curve of the lidar transmitter. The output power of the amplifier at 3 different injection currents was measured as the DC drive current to the ECDL was increased.

The output power of the semiconductor amplifier reached an amazing 576mW CW at 1.5A! A 40% coupling efficiency in the light from the ECDL into the amplifier was maintained during each PI curve. Notice that the sudden increase in optical power occurs at the 15mA threshold current of the ECDL. The curves flatten out above 35mA

indicating the injected light is saturating the gain of the amplifier. The direct relationship between the drive current to the ECDL and its output power allows us to convert the above PI curves to more useful gain curves for the optical amplifier. The amplifier gain in decibels is determined by the logarithmic ratio of the output power P_{out} of the amplifier to the injected power P_{inj} from the ECDL.

$$Gain = 10 \cdot \log\left(\frac{P_{out}}{P_{inj}}\right) \qquad 3.2.2$$

The injected power is determined by the output power of the ECDL at a given current, measured just before the amplifier, and multiplied by a 40% coupling efficiency into the amplifier. The resulting gain curves for each drive current to the flared amplifier is shown below (Fig. 3.2.7).

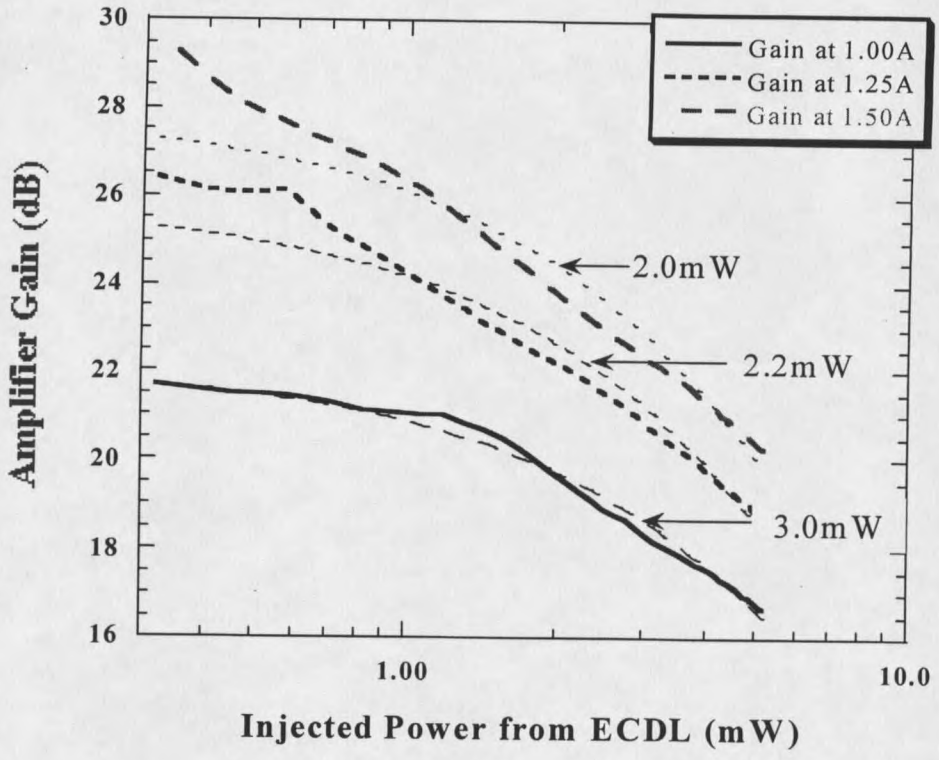


Figure 3.2.7. Single pass gain curves for the flared amplifier as a function of injected optical power from the ECDL at $\lambda = 935$nm. Injection powers needed to saturate the gain of the amplifier at the 3dB level are labeled by each curve.

The semiconductor amplifier provided impressive single pass, small signal gains greater than 21.5dB. We expect the intensity of the injected beam to increase exponentially as it travels down the length L_{amp} of the waveguide inside the flared amplifier [46].

$$I(L_{amp}) = I(0)e^{(\beta-\alpha_l)L_{amp}} \qquad 3.2.3$$

β represents the small signal gain and α_l represents the loss per unit distance due to scattering and absorption. Since the gain of the device is just the ratio of the intensities, $I(L_{amp})/I(0)$, exponential curves were fitted to each gain curve in figure 3.2.7. These fits were used to determine the injected powers where the gain of the amplifier saturates at the 3dB level down from the initial small signal gain.

It is important that the gain of the amplifier is saturated by the injected from the ECDL for a couple of reasons. First, the saturated amplifier will remove small intensity variations of the seed laser during its scan across the water vapor absorption line, providing an even more accurate on line/off line absorption measurement. Second, the density of the electronic carriers responsible for the stimulated emission become constant, which will clamp the index of refraction of the waveguide to a particular n. This will keep the amplifier from frequency chirping the output. This holds true even under pulsed conditions where the pulse length is greater than the time it takes a photon to pass through the amplifier, or > 0.02ns. Since the transmitter is intended to emit 1.28μs long pulses, we do not expect to see any frequency chirp caused by pulsing the current to the flared semiconductor amplifier.

Notice that the 3dB saturation input powers are less than 3mW. That requires the original output power of the 935nm ECDL to be greater than 3mW by 40%, for the coupling efficiency, times 78%, for the transmission through the optics between the ECDL and the amplifier, or 9.6mW. The 935nm ECDL meets this requirement, which allows the seed laser to saturate the gain of the amplifier.

Pulsed Operation

In order for the lidar instrument to measure range-resolved information about the water vapor concentration of the atmosphere, the transmitter must emit a short pulse of light. The departure time of the pulse is synchronized with the receiver so that the receiver can measure the time of flight of the return photons emitted from that pulse

scattered from the atmosphere at various altitudes. A pulse width of $\Delta t = 1.28\mu s$ was chosen to provide a range resolution, or "range bin", of

$$\Delta r = \frac{c \cdot \Delta t}{2} = 192m \qquad 3.2.4$$

The factor of ½ accounts for the round trip distance the scattered light makes per range bin. The time between pulses is set to $\tau = 256\mu s$ which corresponds to a round trip distance of approximately 38km. We expect to see very few photons back scattered to the receiver above an altitude of 10km, so all the range information will be accumulated well before the next pulse leaves the laser transmitter.

A custom designed high-current laser modulator was used to pulse the drive current to the amplifier [47]. The driver is able to deliver a 1.5A pulse with a rise and fall time of 100nsec. A TTL input from a pulse generator supplied the pulse width and repetition rate to the current driver. A amplitude of the current pulse was regulated by adjusting the supply voltage to the array of driver chips in the current driver [45]. The large physical size of the tapered amplifier, relative to typical semiconductor lasers, results in a large parasitic capacitance and inductance that limits the rise and fall time of the optical output pulse. The 1.28μs output pulses have typical rise and fall times of 450ns and 175ns respectively when the amplifier is seeded by the ECDL, as shown below (Fig. 3.2.8.)

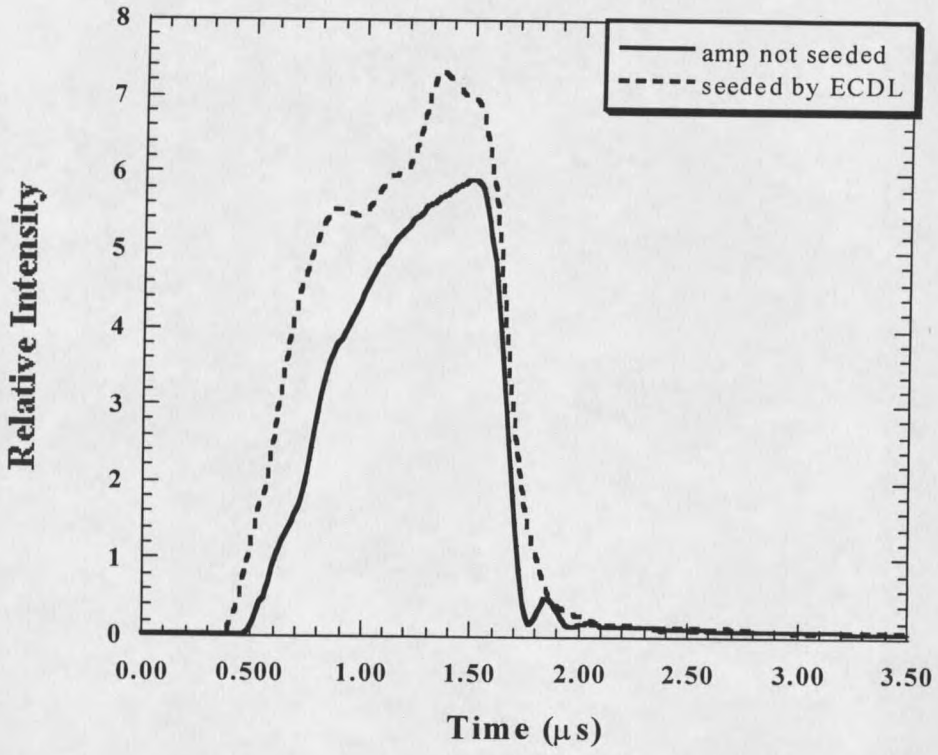


Figure 3.2.8. Output pulse from the semiconductor amplifier driven by a 1.28μs wide, 1.5A current pulse.

Notice that the pulse amplitude of the tapered amplifier with no injected light is nearly as large as when it is seeded by the ECDL. However, this is only a measure of the pulse power and, when seeded, all of that power is concentrated at a single wavelength and not distributed over the entire frequency bandwidth of the amplifier. We expect the rise and fall times to be faster when the amplifier is seeded because the injected photons begin the stimulated emission process immediately. Curiously, the seeded pulse takes on an unexpected structure. It is believed that the anti-reflective coatings on the facets of this particular amplifier had been compromised during previous use, allowing the amplifier to partially lase on its own when operated at drive currents above 1A. This can

cause the gain to be largely dependent on wavelength as indicated by the pulsed spectrum of the device in the absence of the CW seed laser input (Fig. 3.2.9).

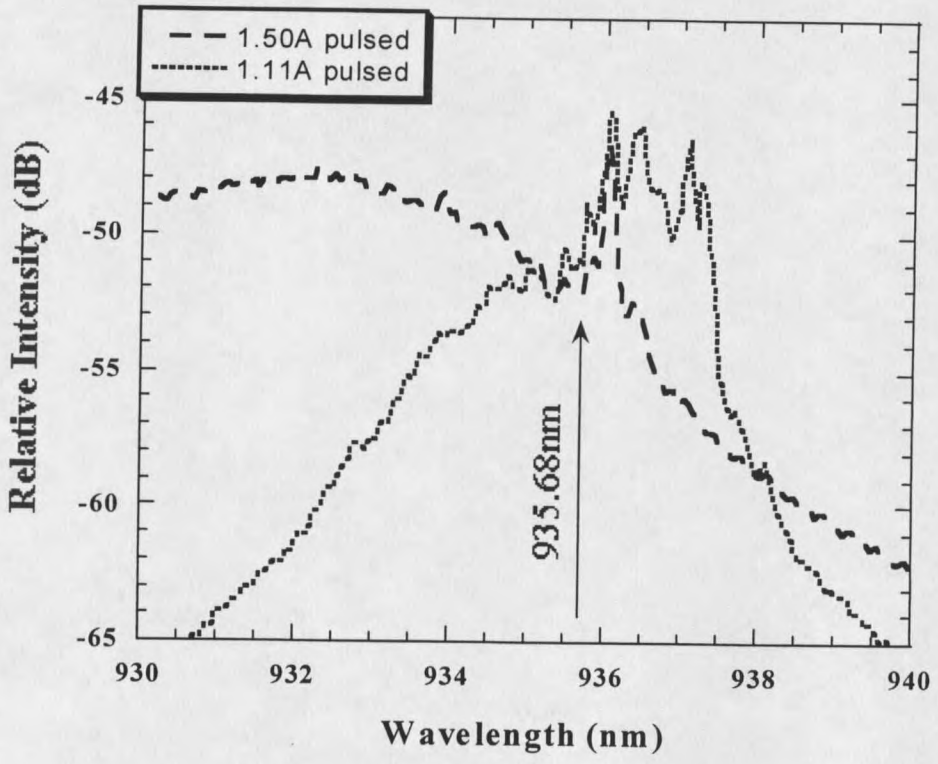


Figure 3.2.9. Pulsed output spectrum of the flared amplifier with no seed laser.

This allows some wavelengths to "turn on" faster than other wavelengths, affecting the shape of the output pulse.

A spectrum of the pulsed amplifier was taken using the fiber Fabry-Perot interferometer with a 25MHz resolution in attempt to verify the chirp in the output. It was not possible to uses the interferometer in its normal scanning mode because the input was pulsed and not CW. Instead, the detector monitoring the transmission of the Fabry-Perot was triggered to record the peak amplitude of the each pulse as the mirror spacing of the interferometer was stepped through a free spectral range [48]. Figure 2.3.10 below

shows that the spectrum of the pulsed output does not seem to be chirped, at least to within the resolution of the fiber Fabry-Perot.

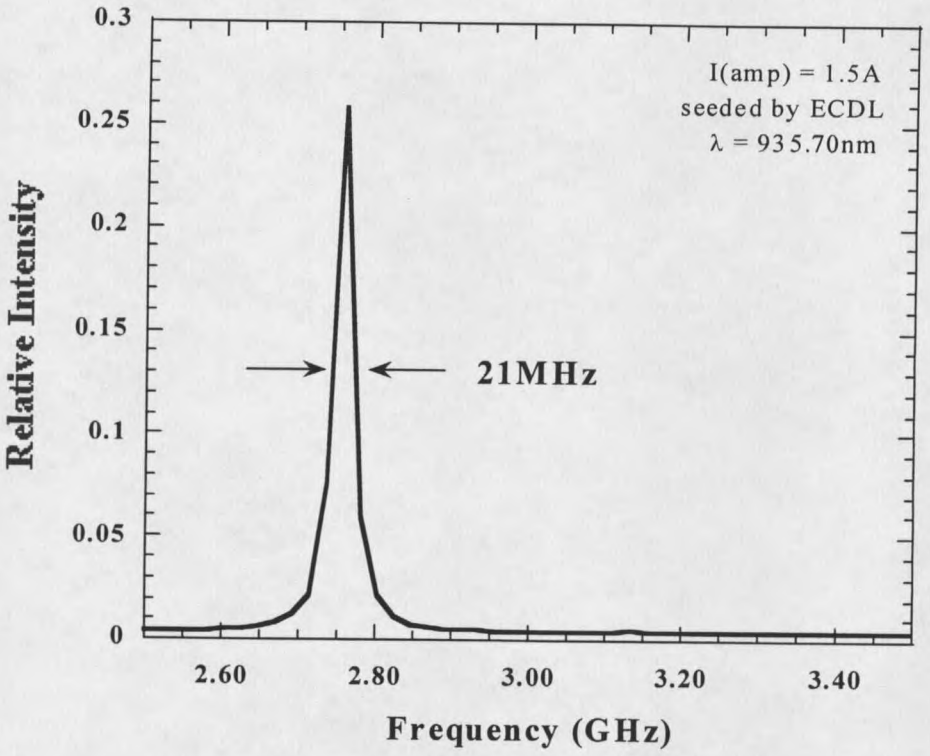


Figure 3.2.10. Spectrum of pulsed, flared amplifier injected with 4.34mW CW beam from the ECDL at 935.70nm shows a chirp-free linewidth of 21MHz. This is at the resolution limit of the fiber Fabry-Perot interferometer.

A second test was performed in order to determine if the output of the pulsed amplifier was chirped or not. I accidentally discovered this while scanning the strong 935.68nm water vapor absorption line with the output from the pulsed laser transmitter system. The output of the pulsed amplifier, seeded to gain saturation by the ECDL, was passed through a multi-pass optical cell that contained 10Torr of pure water vapor. This set up will be discussed in detail in section 4.3. The path length of the cell is adjustable and was set to its longest path length of 10m. At this pressure and temperature, 100% of

the light from the laser transmitter should be absorbed when its wavelength is tuned to the center of the absorption line at $\lambda = 935.68$nm. This provides a narrow absorption filter that should attenuate the entire pulse if its frequency is free from chirp. A detector was used to monitor the transmission of the pulse through the water vapor cell. Even though all of the pulse should be absorbed by the water vapor absorption line, a fraction of the pulse managed to slip through! (Fig. 3.2.11)

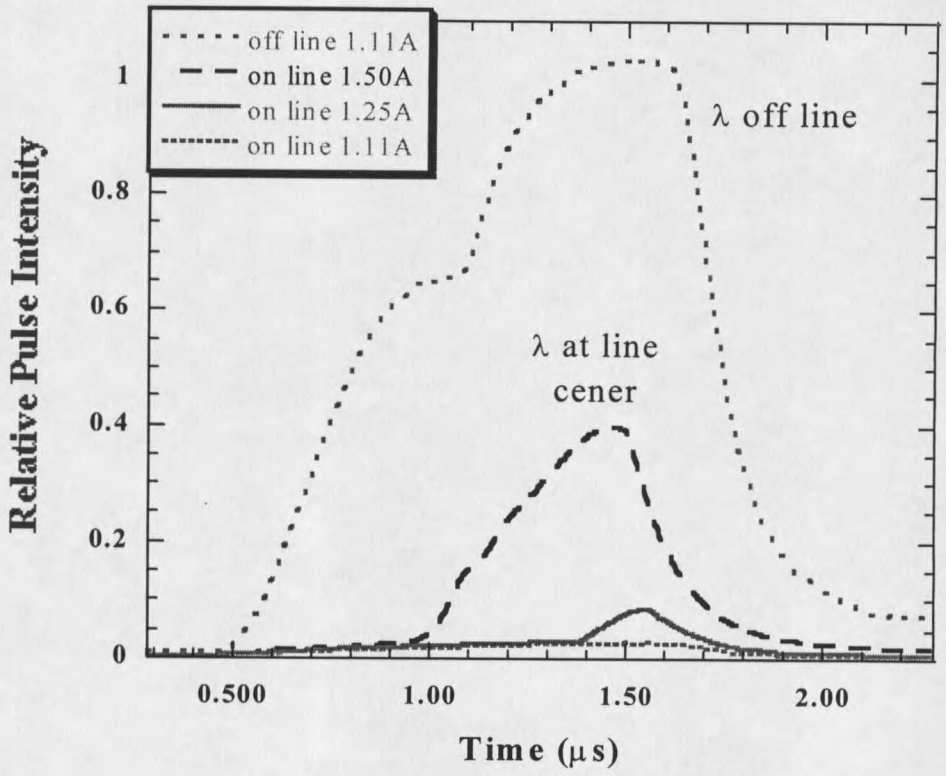


Figure 3.2.11. Verification of frequency chirp by monitoring the pulse transmission through the 935.68nm water vapor absorption line. The water vapor line should absorb all of the pulse only if it is single frequency and at line center.

This can only happen if the output frequency of the pulsed amplifier is chirped or broadened, generating wavelengths other than those at 935.68nm which are not totally absorbed by the water vapor. Figure 3.2.11 above compares the transmitted pulse at the

center of the absorption line with an off line pulse. Notice that a portion of the pulse still exists even when the wavelength of the laser transmitter is tuned to the center of the absorption line. Current to the amplifier was reduced until the frequency chirp was eliminated, identified by the disappearance of the transmitted pulse. Therefore, 1.11A was the maximum current that could drive the amplifier before it would suffer frequency chirp. This current limits the peak power of the laser transmitter to 285mW. This corresponds to a pulse energy of 0.36μJ for a 1.28μs pulse width. This was a sure method used to set the maximum pulse current to the amplifier, which, in the end, determined the maximum output power of the laser transmitter.

3.3 Overall Laser Transmitter Performance

The laser transmitter consists of the 935nm ECDL whose single frequency, tunable wavelength, CW output is used to seed a flared semiconductor amplifier that both amplifies and pulses the output that will be sent into the atmosphere. This laser system was specifically designed to scan across the water vapor absorption line at 935.68nm. Although far from being flight ready, this bread board transmitter was valuable in determining its output parameters and its ability to measure the 935.68nm water vapor absorption line. We believe this to be the first, all-semiconductor, master oscillator (ECDL), power amplifier (flared amplifier) laser transmitter for a miniature 935nm water vapor lidar system [49]. The performance of the laser lidar transmitter is summarized in table 3.3.1 below.

Table 3.3.1. Performance summary of the 935nm laser transmitter developed for the water vapor lidar system.

Parameter	**Laser Performance**
Peak Output Power	285mW
Pulse Width	1.28μs, adjustable
Pulse Energy	0.36μJ
Repetition Rate	3.906kHz, adjustable
Wavelength	926-944nm
Continuous λ scan	70pm (25GHz)
Wavelength Stability	110MHz/hour
Mode suppression ratio	> 40 dB
Spectral linewidth	< 21MHz, chirp free
Total Electrical Power	<0.5W

CHAPTER 4

MEASURING WATER VAPOR AT 935nm

4.1 Spectroscopy of the Optimal Water Vapor Absorption Line

Water vapor, like other atmospheric gasses, absorbs specific wavelengths of light. Light interacts with the natural, vibration-rotation resonant frequencies of the H_2O molecule generating a series of narrow absorption lines that is unique to this particular molecule in its gaseous state. The center wavelength of the absorption lines are relatively insensitive to temperature and pressure variations making them ideal targets to study dynamical processes of the atmosphere. The degree to which a particular resonance absorbs a specific frequency of light depends on the oscillator strength and the number of absorbing molecules that are present. This makes it possible to infer the concentration of atmospheric water vapor molecules by measuring its absorption of a specific frequency of light. Figure 4.1.1 below shows a broad absorption spectra of water vapor in the Earth's atmosphere at a pressure of 1 atmosphere (760Torr) and 23°C over a path length of 50m predicted by HiTran '96 atmospheric database [50].

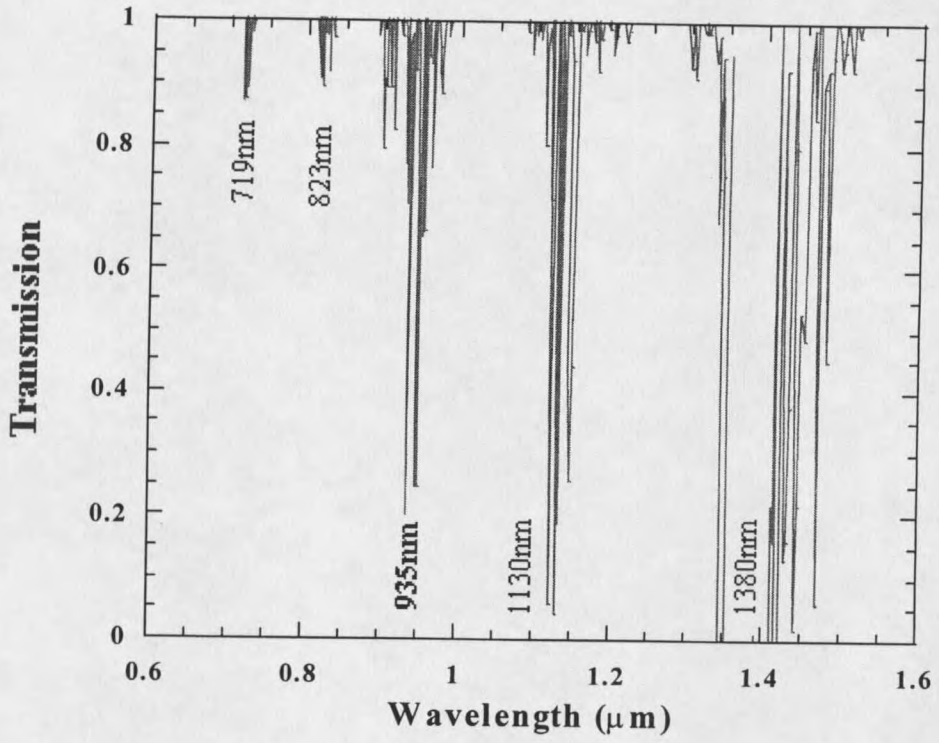


Figure 4.1.1. Absorption spectra of atmospheric water vapor at 1atm, 23°C over a path length of 50m.

HiTran '96 atmospheric data base is an accumulation of absorption and transmission parameters of atmospheric gasses carefully measured and documented by researchers over many years. Originally, these parameters were incorporated into a database developed by the Air Force Geophysics Laboratory. This database has been converted to a random access format at the University of South Florida and Ontar offers a simple user interface that can access the database using a personal computer. Although there are gaps of missing absorption lines and it is difficult to know how accurate the parameters are for the existing absorption lines, the database has been accepted by the scientific community as the standard source for modeling atmospheric absorption and transmission.

Figure 4.1.1 predicts several absorption bands exist for water vapor in the near infrared spectrum. Because there is very little water vapor in the Martian atmosphere, the strong absorption lines at 1130nm and 1380nm are attractive because they would provide the strongest possible absorption signals. However, silicon-based avalanche photodiodes are used to measure the back scattered photons in the lidar receiver which are the most sensitive, low voltage, photon counting detectors available. Unfortunately the silicon detectors only response to lower wavelength radiation of $500nm < \lambda < 1050nm$. As a compromise, the strongest absorption band that can be detected by the silicon photodiodes lies in the 935nm region. Figure 4.1.2 below shows a higher resolution plot containing the stronger absorption lines in the 935nm region.

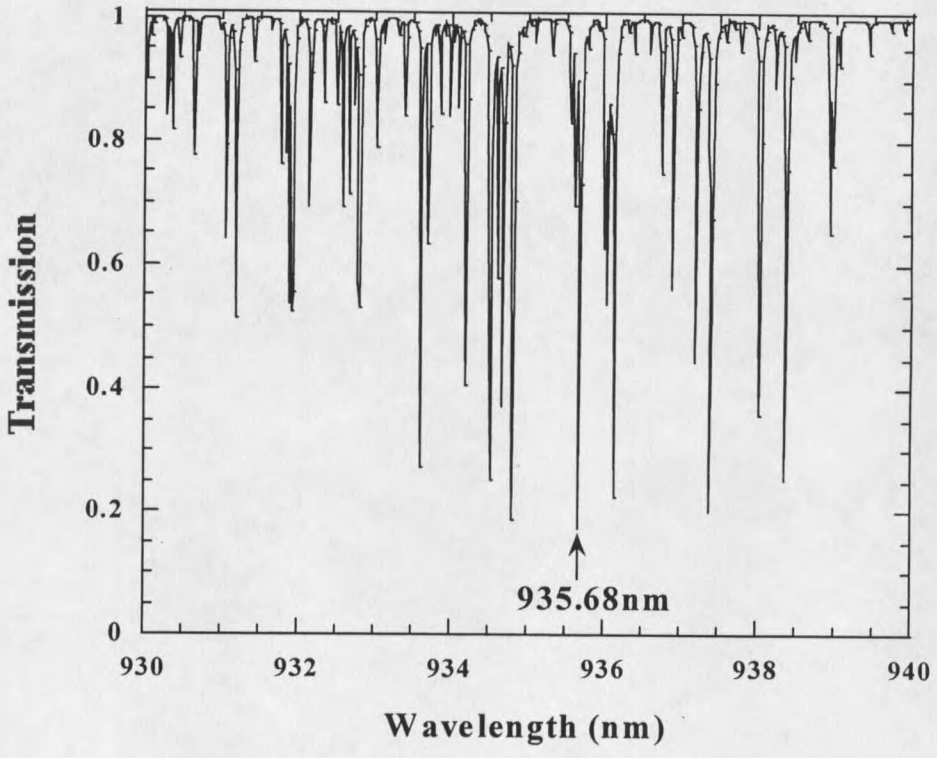


Figure 4.1.2. HiTran '96 prediction of the absorption spectrum of the 935nm region at a pressure of 1atm, 23°C over a path length of 50m.

The parameters for each absorption line can be used to narrow down the choice for the optimum line that will be used by the lidar system. For instance, a line intensity S has been measured for each absorption line and is directly related to the oscillator strength at a particular frequency. $S = 5.419 \times 10^{-22}$ $cm^{-1}/(molecules\ cm^{-2})$ for the line at 935.68nm which is the largest value in this absorption band making it the strongest absorber. The lower energy level for this absorption line lies at $E'' = 136.8cm^{-1}$ which is less than $kT \simeq 160cm^{-1}$ at a Mars-like temperature of 230K (-43^0C) which will minimize the temperature sensitivity of the absorption [41]. Based on this criteria, the 935.68nm absorption line was chosen because of its strong line intensity and temperature insensitivity. This is the water vapor absorption line that our lidar system will be designed to measure.

The absorption line parameters are the same regardless of where we measure the water vapor; on Earth or on Mars. However, an atmospheric absorption line measured on Mars would appear much narrower and weaker than if the same line were to be measured on Earth because Mars has a thin, low pressure atmosphere. Knowing the line parameters, we can predict what the 935.68nm water vapor absorption line would look like if we could measure its absorption over a 1km horizontal path length through the Martian atmosphere (Fig. 4.1.3).

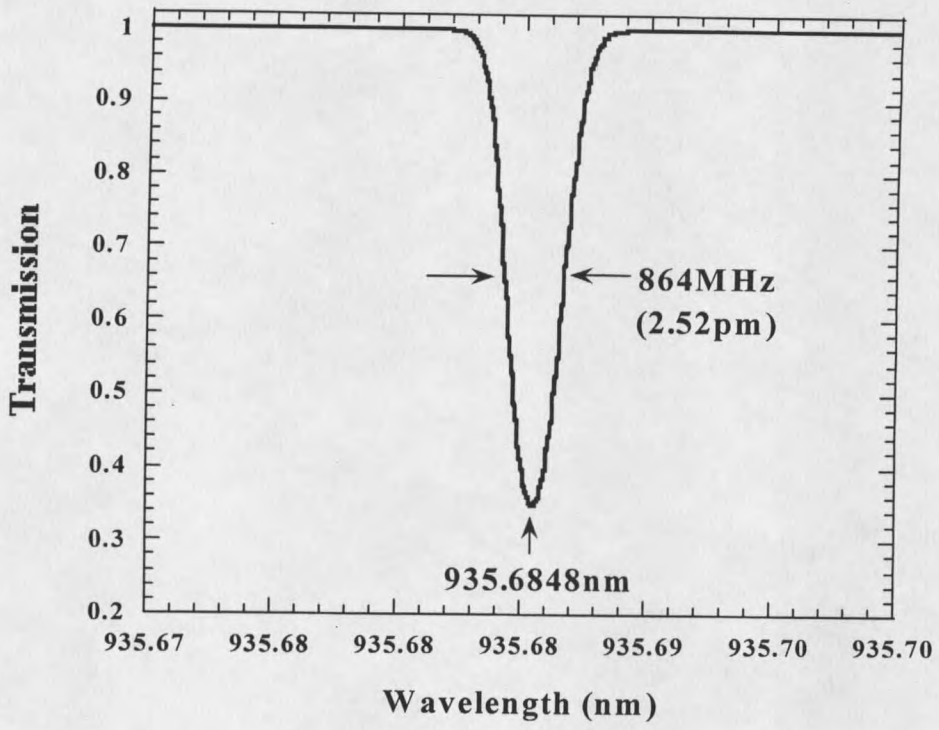


Figure 4.1.3. Prediction of the 935.68nm absorption line. The line was calculated for an atmospheric temperature and pressure of 4.56Torr and -30°C respectively, similar to the atmospheric conditions on Mars, over a 1km horizontal path length.

This chapter discusses the measurements of the 935.68nm water vapor absorption line using the laser transmitter developed for this project. The line was measured at both atmospheric pressures and at low, Mars-like pressures. In both cases, the experimental measurements were compared to theoretical predictions of the absorption line in order to estimate what the accuracy of an actual water vapor lidar system would be.

4.2 Measuring Water Vapor at One Atmosphere using the ECDL

In this section, we get to actually measure the water vapor absorption line using the external cavity diode laser we developed for the lidar system! First, the 935.68nm absorption line is modeled using the parameters from HiTran '96, then the ECDL is used to measure the absorption profile and see how well it fits the model. The air in the lab contains enough water vapor to see a 50% absorption by passing the output from the ECDL around the lab over a 16m path, so it conveniently served as the "test atmosphere" for these experiments. Finally, the ECDL was used to monitor the relative humidity of the lab over 3 hours under continuous scanning conditions, simulating actual lidar operation.

Model the Absorption Line using HiTran Parameters

In order to infer the concentration of the atmospheric water vapor molecules from the absorption of the lidar signal, it is necessary to understand exactly how the concentration affects the measured absorption. This can be done by developing a mathematical model that uses the line parameters from the HiTran '96 atmospheric database which can accurately describe the profile of the absorption line.

Not surprisingly, the atmosphere contains a mixture of different gasses, not just water vapor. The concentration of each gas is directly related to its partial pressure, and the sum of the partial pressures of each gas adds up to the total pressure of the atmosphere. The partial pressure, in atmospheres, of water vapor depends on the relative humidity and temperature (in Celsius) of the atmosphere according to [51]:

$$P_{H_2O} = RH \times \left(6.11 \times 10^{\frac{aT}{b+T}} \right) \times \frac{1}{1013.25} \qquad 4.2.1$$

RH represents the relative humidity defined as the fraction of the atmosphere which is saturated with water vapor. Constants a = 7.5 and b = 237.3 apply to saturated vapor with respect to liquid water. These constants have slightly different values if ice produces the vapor. The factor of 1/1013.25 converts the result of the partial pressure from millibars to atmospheres. For instance, on Tuesday, April 7, 1998, the following atmospheric conditions were recorded inside the lab at NASA/GSFC in Greenbelt, MD:

Table 4.2.1. Atmospheric conditions inside the lab at NASA/GSFC during a measurement of the 935.68nm water vapor absorption line.

Temperature, T	24.0°C = 297K
Pressure, P_T	755Torr = 0.993atm
Relative Humidity, RH	0.43

The partial pressure of the water vapor P_{H2O} = 0.01267atm was calculated for these particular conditions of our "test atmosphere". Notice that the water vapor makes up just a little over 1% of the total pressure of the atmosphere. The partial pressure can be used to determine the halfwidth of the absorption line, γ_P in cm^{-1} [52].

$$\gamma_P = \left(\frac{296}{T+273} \right)^n \times \left(gs \cdot P_{H_2O} + ga(P_T - P_{H_2O}) \right) \qquad 4.2.2$$

The constants n, gs, and ga are parameters for the 935.68nm water line whose values are contained in the HiTran database, and the temperature T is in Celsius. For the 935.68nm line, n = 0.61, gs = 0.5, and ga = 0.0912 cm^{-1}/atm. A halfwidth of γ_P = 0.096cm^{-1} was

calculated for a temperature of 24°C and the partial pressure P_{H2O} = 0.01267atm determined above.

Gasses exposed to total pressures greater than a few Torr (may not be a problem on Mars!) have a pressure-broadened, Lorentzian absorption profile. This familiar function, $g(\nu-\nu_o)$ in cm, depends on the absorption halfwidth.

$$g(\nu-\nu_o)=\frac{1}{\pi}\frac{\gamma_P}{(\nu-\nu_o)^2+\gamma_P{}^2} \qquad 4.2.3$$

Assuming the water vapor in the atmosphere acts like an ideal gas, the number of molecules of the absorbing gas varies with temperature T in Celsius by:

$$N=N_L\cdot\frac{296}{T+273} \qquad 4.2.4$$

$N_L = 2.479 \times 10^{19}$ molecules/cm^3 atm represents Loschmidts' number which is the molecular density of a gas for a standard atmosphere. Finally, recall the line intensity S = 5.419×10^{-22} cm^{-1}/molecules cm^{-2} describes the oscillator strength of the water molecule at this particular frequency. With the help of the HiTran line parameters, these functions can be used to predict the frequency dependent transmission of light through the water vapor over a path length L [52]

$$T(\nu)=\exp\left[-S\cdot g(\nu-\nu_o)\cdot N\cdot P_{H_2O}\cdot L\right] \qquad 4.2.5$$

In the above expression, S $g(\nu-\nu_o)$ represents the absorption cross section per molecule (cm^2/molecule) and N P_{H2O} represents the absolute density of the absorbing molecules (molecules/cm^3). The overall goal of our lidar system is to determine the absolute density of the water vapor molecules, N P_{H2O}, per range bin of length L = 192m by measuring the absorption (1 - transmission) of the return signal!

Measure the Absorption Line Using the ECDL

The 935nm ECDL was used to measure the profile of the absorption line calculated above under the same atmospheric conditions. The low power, CW beam provided plenty of light to bounce across the lab and back over a 15.66m path length in the air, so the pulsed amplifier was not needed. The measurement were performed primarily to test the performance of the ECDL as the master oscillator under real, scanning lidar conditions. The following experimental set up was used to measure the water line by scanning the air in the lab (Fig. 4.2.1)

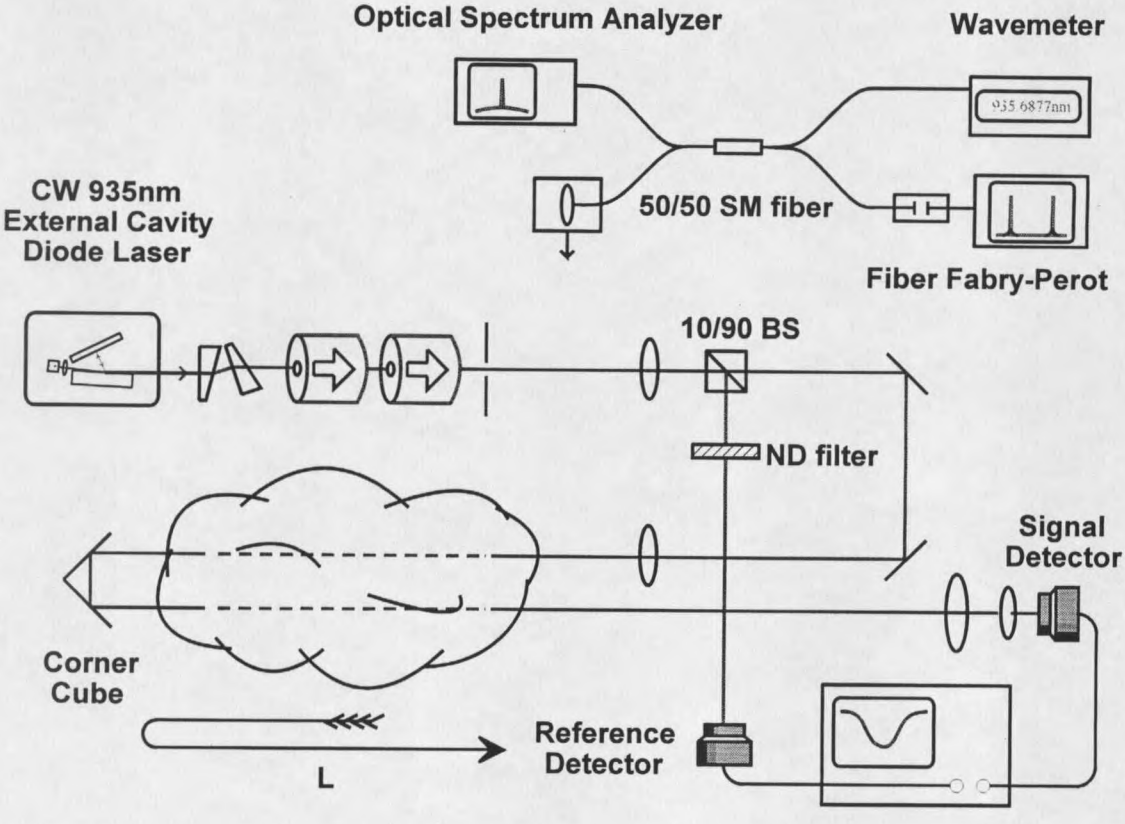


Figure 4.2.1. Experimental set up used to measure the 935.68nm water vapor absorption line using the air in the lab as the "test atmosphere".

Light from the ECDL passes through an anamorphic prism pair and two optical isolators to protect the laser from feedback, similar to the linewidth experiments discussed in section 2.3. A fiber launch can be slid in and out of the beam which couples light into a 2x2 single mode fiber. The fiber delivers the light to various instruments used to monitor the laser ensuring its output is single mode and tuning continuously while scanning. The fiber launch is removed from the beam while measuring the water vapor. 10% of the beam is reflected to a reference detector using a beam splitter. The remaining beam passes through the beam splitter, across the lab to a 6" portable corner cube, and reflected back to the lab bench where it is focused onto a signal detector. The voltage output from the signal detector is divided by the reference detector to remove any intensity fluctuations caused by the ECDL as it scans across its wavelength range. A neutral density filter in the beam path to the reference detector is used to match the strength of the two signals when the wavelength is tuned off the center of the absorption line.

An arbitrary waveform generator (Tektronix AWG2021) supplied a saw-tooth waveform (with rounded corners to protect the PZT from a fast turn around) to the PZT driver. The PZT driver amplified the signal 15 times and stretched the PZT on the ECDL, scanning its wavelength over 75pm at a rate of 25Hz. The detector outputs were sent to a digitizing oscilloscope triggered by the waveform generator so the absorption line and the background curve of the scanning laser could be monitored in real time. The wavelength was calibrated by measuring the wavelength of the laser output on the wavemeter (Burleigh WA1500) for several DC offsets from the waveform generator,

before scanning. A curve was fitted to this data and used to calibrate the wavelength axis of the scan. The absorption line below was measured for a path length of 15.66m through the air in the lab (Fig 4.2.2).

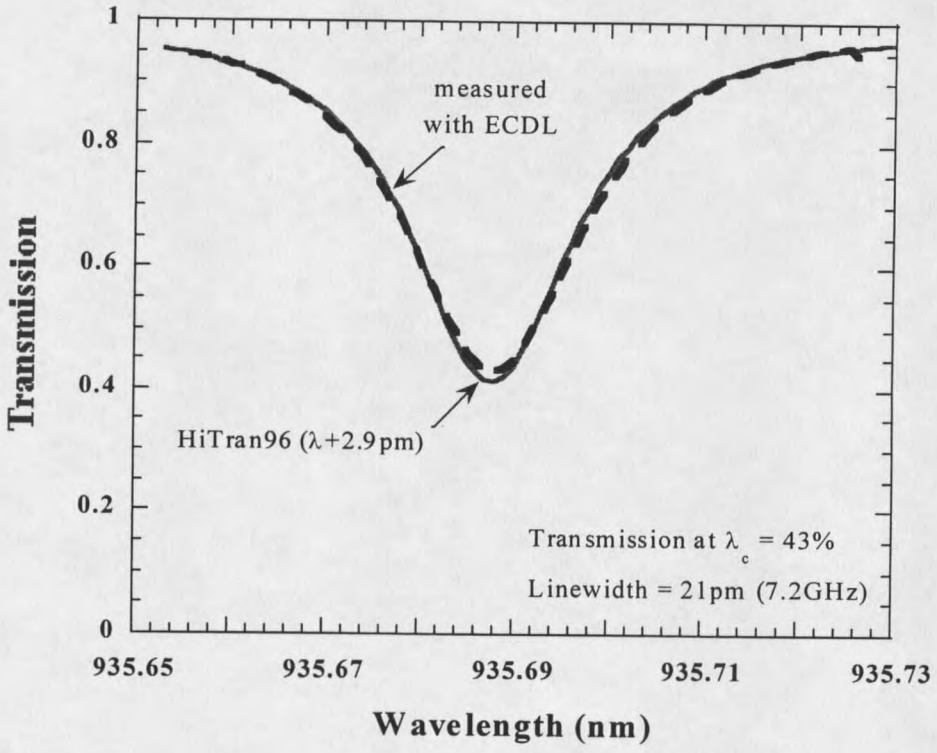


Figure 4.2.2. Comparison of the 935.68nm water vapor absorption line measured in air using the ECDL (dashed line) with that theoretically predicted by HiTran '96 (solid line). The center wavelength of the calculated line had to be shifted over by 2.9pm because the theoretical prediction did not include the pressure shift in the line from vacuum to 755Torr.

The measured absorption line agrees well with that predicted by the model using the line parameters from HiTran '96. The linewidth of the two profiles are nearly identical indicating that the output from the ECDL must be single mode and mode hop free through the entire scan. Four more scans of the water line were made at various path lengths from 6.65m to 18.66m which also provided excellent agreement between the

predicted profile the measured scan. There is a 2% difference in the transmission of the two lines at their center wavelength. This is within the ±3% range for possible systematic error. Table 4.2.2 list the possible sources for error and their largest values which, in the worst case, could all add yielding the largest possible difference in the center transmission.

Table 4.2.2 Sources for experimental error and their worse-case values.

Experimental parameter	**Possible error in measuring parameter**	**Effect on transmission at line center**
Path length, L	±0.02m	±0.0004
Total Pressure, P_T	±2Torr	±0.0009
Air Temperature, T	±1K	±0.0202
Relative Humidity, RH	±0.01	±0.0080

If the accumulation of the errors were to all increase or all decrease the predicted transmission at line center, the transmission could be affected as much as ±0.0295, or nearly 3%. It turns out the uncertainty in measuring the temperature of the air in the lab using a precision mercury thermometer provided the largest source of error. It is not surprising that a small error in measuring the temperature can have a big difference in the predicted transmission at line center because of the frequent temperature dependence found the equations used to calculate the absorption profile. Therefore, the degree to which we can estimate the temperature profile of the Martian atmosphere will likely be the major factor limiting the accuracy of the water vapor concentration measurements made by the future Mars lidar instrument.

Using the Laser to Monitor the Relative Humidity in the Lab

Thrilled by the excellent agreement between the predicted and measured profiles of the 935.68nm water vapor absorption line, I thought it would be fun to see if this experimental set up could be used to monitor the relative humidity of the lab! Instead of capturing the entire profile, the detectors would record only 4 values along the scan of the water vapor line. The arbitrary waveform generator has the capability to set TTL markers at any point in its output waveform. One marker was positioned at the center of the absorption line, a second marker was positioned at the end of the scan, off line, and the other two markers were positioned near the half-way point of the absorption line (Fig. 4.2.3).

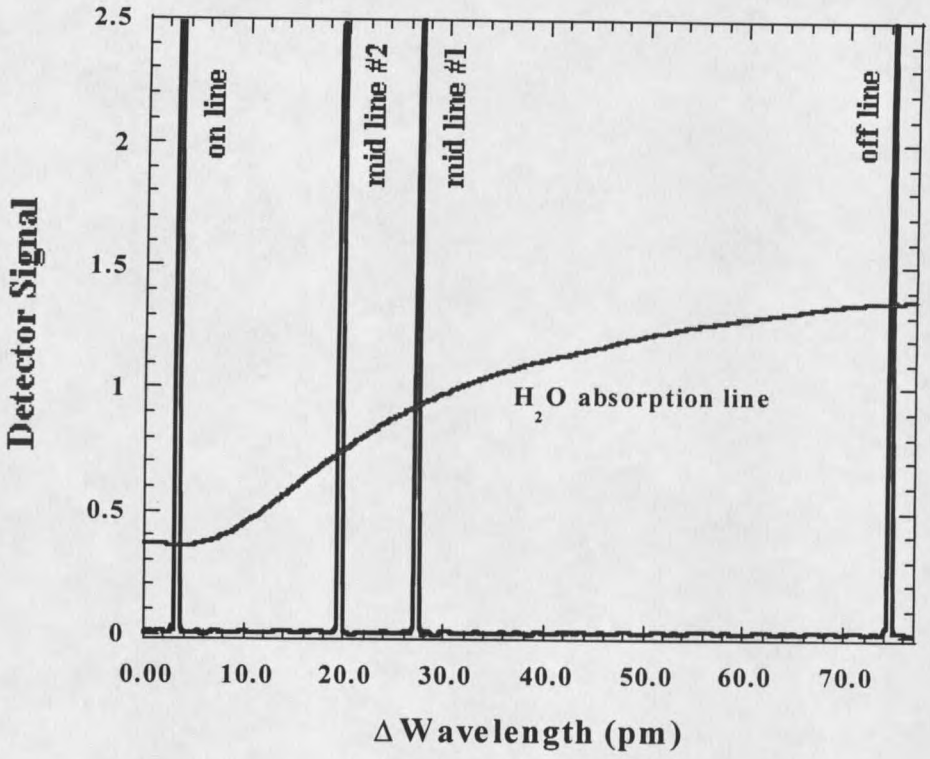


Figure 4.2.3. Method for making on-line/off-line absorption measurements. Markers were positioned along the wavelength scan and used to trigger the detectors to read the on line, mid line, and off line values along the absorption profile.

These markers were used to trigger the digitizing scope to display both the reference and signal detector outputs, read immediately by a computer using Labview [48]. The computer recorded the ratio of the detectors for each marker resulting in a 4 x n array of values. The computer interface was not fast enough to capture each marker value for each scan going by at 25Hz, the continuous scan rate of the ECDL. However, it was able to record the detector values at their corresponding marker location about every 3 to 4 seconds.

The equations used to predict the profile of the absorption line can be manipulated such that the relative humidity and concentration can be determined from the recorded

detector values. The beam intensity at the center of the absorption line is determined by the ratio of the detectors when the wavelength was tuned to the "on line" marker location.

$$I(on\ line) = \left(\frac{\text{signal detector}}{\text{reference detector}} \right)_{\text{on line marker}} \qquad 4.2.6$$

An identical ratio was taken to determine the off line intensity, I(off line). However, some of this "off line" intensity was still being absorbed by the tail of the pressure broadened line. This was corrected with an offset measured by comparing the intensity far outside the off line marker to I(off line). Such a correction will not be necessary when measuring water vapor on Mars because the line is much narrower at an atmospheric pressure of 5Torr. Incidentally, values were recorded at the two middle markers hoping that they could be used to help estimate the atmospheric pressure or temperature. This analysis still needs to be completed. The transmission of the light through the air at the center of the absorption line is normalized by:

$$T(\nu_o) = \frac{I(\text{on line})}{I(\text{off line})} \qquad 4.2.7$$

The Lorentzian profile in equation 4.2.3, $g(\nu-\nu_o)$ expressed in cm, is simplified if we are only interested in the transmission at the center of the absorption line ν_o.

$$g(\nu = \nu_o) \rightarrow \frac{1}{\pi \cdot \gamma_P} \qquad 4.2.8$$

Writing out the expression for the halfwidth, γ_P according to equation 4.2.2 and plugging it into expression 4.2.5, the transmission at line center $T(\nu_o)$ becomes:

$$T(\nu_o) = \exp\left[-K \frac{P_{H_2O}}{P_{H_2O}(gs - ga) + P_T ga} \right] \qquad 4.2.9$$

The constant K contains everything except for the partial pressure of the water vapor and the total pressure of the atmosphere. We can assign a value to the constant K specific to the current air temperature of T = 23.2°C and path length L = 18.66m for this experiment.

$$K = S \cdot \left[\pi \left(\frac{296}{T+273} \right)^{n} \right]^{-1} \cdot N_L \cdot \frac{296}{T+273} \cdot L \rightarrow 7.97 \ \text{atm}^{-1}cm^{-1} \qquad 4.2.10$$

Expression 4.2.9 can be solved for the partial pressure of the water vapor P_{H2O} in atmospheres which will depend on the normalized transmission.

$$P_{H_2O} = -P_T \cdot ga \left[\frac{K}{\ln[T(\nu_o)]} + (gs - ga) \right]^{-1} \qquad 4.2.11$$

That is, the partial pressure of water vapor can be determined by measuring the transmission of a laser beam on and off the absorption line through an unknown atmosphere over a given path length using the simple expression of 4.2.11! For instance, the transmission at the center wavelength was measured to be $T(\nu_o) = 0.257$ over an 18.66m path length across the lab. Therefore the partial pressure of the water vapor was calculated to be:

$$P_{H_2O} = 0.0166atm \rightarrow 12.6Torr \qquad 4.2.12$$

Determining this partial pressure tells us a lot about the water content in the atmosphere. For instance, the mass mixing ratio of the water vapor molecules to the rest of the "air" molecules is [51]:

$$Rm = \frac{P_{H_2O}}{P_T} \cdot \frac{M_{H_2O}}{M_{air}} \cdot 1000 \rightarrow 10.4 g/kg \qquad 4.2.13$$

The mass of air molecules on Earth is taken to be $M_{air} = 28.9 g/mol$. Similarly, the volume mixing ratio expresses the mass concentration of water vapor in parts per million:

$$Rv = \frac{P_{H_2O}}{P_T} \cdot 10^6 \rightarrow 16700 ppm \qquad 4.2.14$$

Recall the goal of this experiment was to monitor the relative humidity of the lab, readily available by solving equation 4.2.1 for RH:

$$RH = P_{H_2O} \times \left[6.11 \times 10^{\frac{aT}{b+T}} \right]^{-1} \times 1013.25 \rightarrow 0.590 \text{ or } 59\% \qquad 4.2.15$$

The average number density of water vapor molecules can be determined using the ideal gas law PV = nkT.

$$\rho_{H_2O} = \frac{n}{V} = \frac{P_{H_2O}}{k \cdot (T + 273)} \cdot \frac{1.01325 \times 10^5}{10^6} \rightarrow 4.10 \times 10^{17} \text{ molecules} / \text{cm}^3 \qquad 4.2.16$$

Equation 4.2.15 was used to express the data collected in terms of the relative humidity and equation 4.2.14 was used to express the results in terms of the concentration of the water vapor in the air. The ECDL monitored the atmosphere in the lab for over 3 hours and provided the results shown in figure 4.2.4.

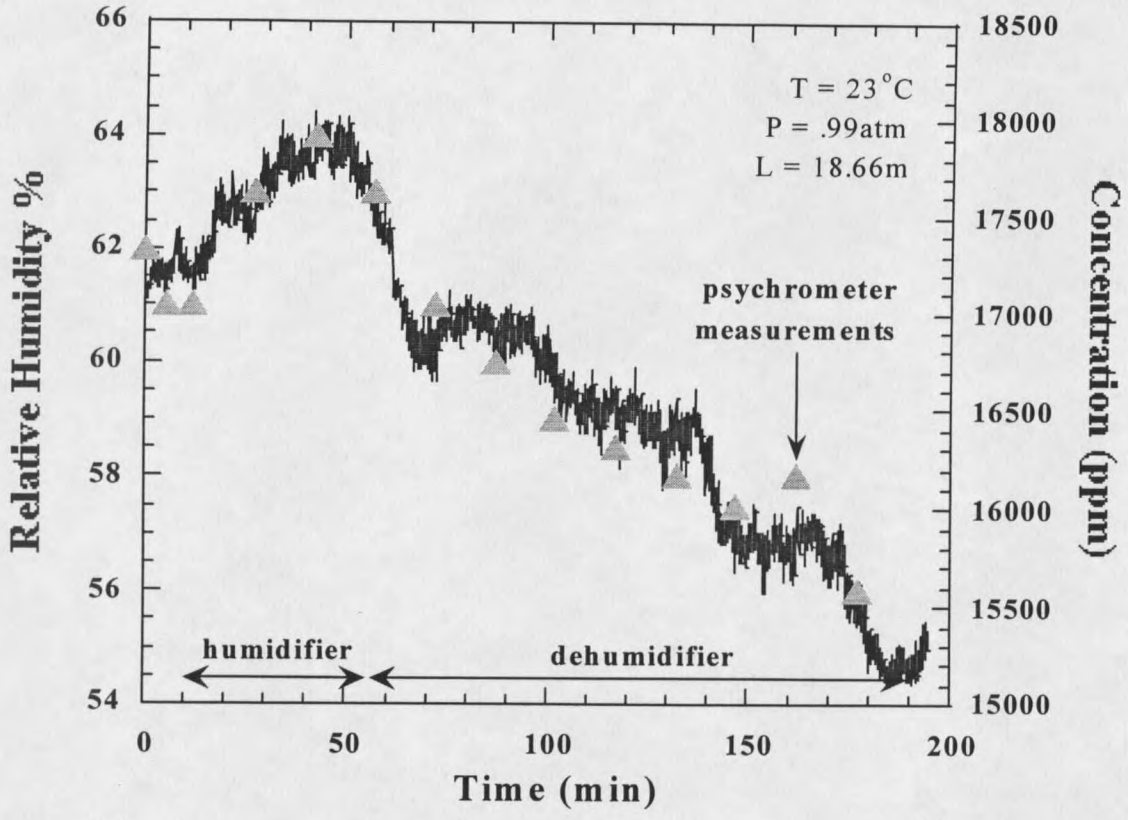


Figure 4.2.4. Relative humidity and water vapor concentration of the air in the lab as measured by the 935nm ECDL. The relative humidity was compared to psychrometer measurements taken every 15 minutes.

In attempt to make the curve more interesting, I brought a humidifier into the lab and turned it up to "high" for the first hour. Then I turned off the humidifier and turned on a de-humidifier, again up to "high", for the remainder of the experiment, trying to remove some of the humidity from the room. The small fluctuations in the curve correspond to a 250ppm uncertainty in the water vapor concentration. This is sufficient resolution to measure the expected 3000ppm concentration of water vapor in the Martian atmosphere! The relative humidity measured using the ECDL agrees well with those measured with a psychrometer. A psychrometer measures relative humidity by

comparing the temperatures between two thermometers, one dry and the other in a wetted wick. The dryer the air, the more the wick lowers the temperature of the thermometer through evaporation. The difference in temperatures between the thermometers can be correlated to the relative humidity for a specific air temperature using a table supplied with the psychrometer.

In proudly reporting my results to my peers at NASA/GSFC, they informed me of a commercially available instrument shown in figure 4.2.5 that could measure the relative humidity of the lab for only $170! [53]



Figure 4.2.5. Relative humidity meters are already commercially available!

This unit uses a thin-film polymer capacitor to sense a change in relative humidity. Air passes between the plates of the capacitor and, as the water content in the air varies, so does its dielectric constant. So why not just send this to Mars?

First, the lidar system will only measure water vapor because it identifies the absorption line that is unique to that particular atmospheric gas. Any gas that causes a change in the dielectric constant between the plates of the capacitor inside the commercial unit will register as a change in relative humidity. Second, a lidar system is the only convenient way to collect range resolved profiles up to 5km from the surface of Mars. Although not the easiest way to monitor the relative humidity of the lab, this experiment demonstrated that we could learn a lot of meaningful information about the water content in the atmosphere using our tunable laser.

4.3. Measuring Water Vapor at Low Pressures Using the ECDL/Amplifier

The atmospheric pressure on Mars averages about 6.1mbar (4.6Torr) near the surface compared a pressure of 1013mbar (760Torr) on Earth [54]. This lower pressure reduces the linewidth of the water vapor absorption lines a great deal, making them more challenging to measure. For instance, the narrow absorption line is much less forgiving to slight wavelength drift of the lidar transmitter or frequency chirp in its output. Therefore a low pressure "test atmosphere" containing water vapor is needed to characterized the laser transmitter's ability to accurately measure the narrow absorption line at 935.68nm. This is accomplished by passing the beam through an optical cell that can be evacuated to low pressures, yet allow us to bleed in pure water vapor. This section describes these experiments and their results using both the master oscillator (ECDL) and the power amplifier (flared amplifier) as the laser transmitter.

Model the Absorption Line Using HiTran Parameters

For the following experiments, the "test atmosphere" resides inside a low pressure optical cell containing pure water vapor. A photo of the water vapor cell is shown below in figure 4.3.1 [55].

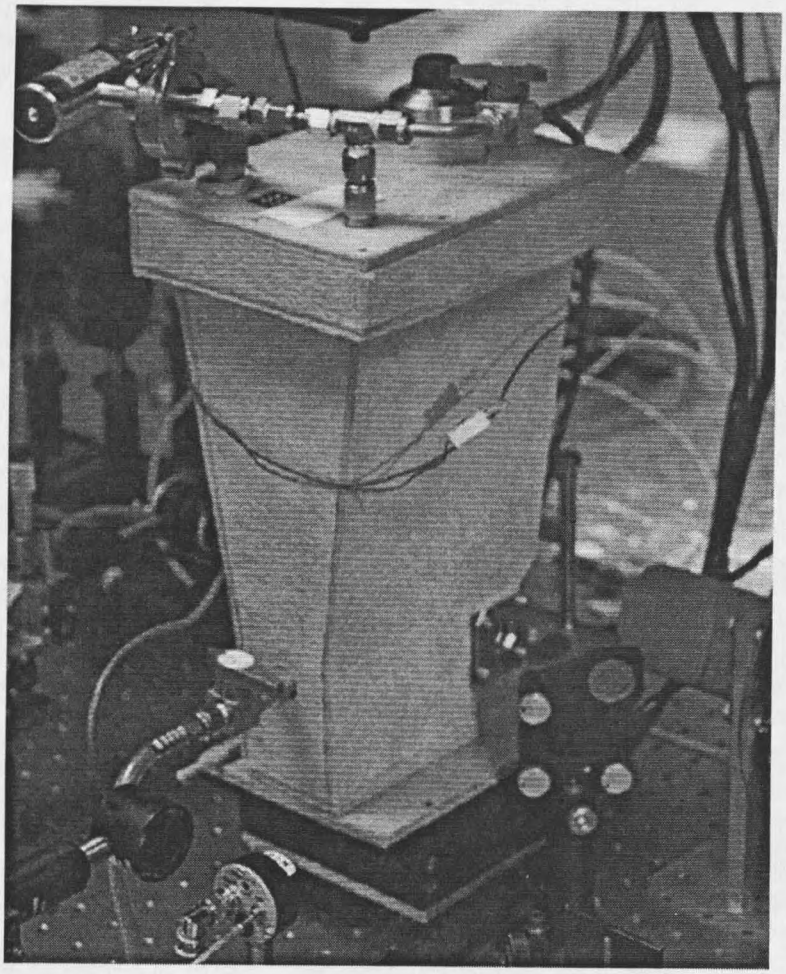


Figure 4.3.1. Low pressure, multi-pass optical cell used to create a low pressure test atmosphere containing water vapor.

In order to create this atmosphere, the cell was first pumped down to a few millitorr. Then water vapor was siphoned from a flask containing 99% pure water that was connected to the cell. At room temperature, the vapor pressure of water is approximately 20Torr, setting the upper limit of what the "atmospheric" pressure can be inside the cell. The cell was then evacuated and refilled with more water vapor. This process was repeated several times to guarantee the cell was saturated with pure water vapor. The

absorption line was measured at 5 different pressures from 0.5Torr to 10Torr. Table 4.3.1 list the atmospheric conditions inside the cell.

Table 4.3.1. Atmospheric conditions inside the low pressure optical cell.

Temperature, T	25°C = 298K
Pressure, P_T	5.0Torr = 0.0066atm
Relative Humidity, RH	1.0

For atmospheric pressures below a few Torr, the linewidth of the water vapor absorption line is dominated by Doppler/Gaussian broadening. Therefore in modeling the line profile, the pressure broadened halfwidth in equation 4.2.2 must be replaced by a the Doppler broadened halfwidth γD in cm^{-1} [52].

$$\gamma D = \frac{\nu_o}{c} \cdot \left(2RT \frac{\ln(2)}{M_{H_2O}} \right)^{\frac{1}{2}} \cdot 10^{\frac{3}{2}} \qquad 4.3.1$$

In the above expression, R = 8.3143J/mol K is the gas constant and the mass of the water vapor molecule M_{H2O} = 18.015g/mol. The factor of $10^{1.5}$ converts the units of M_{H2O} from grams to kilograms to cancel with the units of R. For similar reasons, the Lorentzian line shape function in equation 4.2.3 must be replace by the Gaussian line shape $g(\nu-\nu_o)$ in cm.

$$g(\nu - \nu_o) = \frac{1}{\gamma D} \cdot \left(\frac{\ln(2)}{\pi} \right)^{\frac{1}{2}} \cdot \exp\left[-\ln(2) \frac{(\nu - \nu_o)^2}{\gamma D^2} \right] \qquad 4.3.2$$

Since the optical cell contains only pure water vapor, the relative humidity RH = 1 for these experiments. The rest of the equations in section 4.2 remain unchanged and can be applied to modeling the low pressure absorption line.

Measure the Absorption Line using the ECDL/Amplifier

The pulsed, flared amplifier, seeded by the 935nm ECDL, was used to measure the profile of the absorption line calculated above for the same atmospheric conditions. 10% of the high power beam was split off and focused onto a reference detector. The remaining beam intensity was coupled into the cell using a 30cm lens before entering the cell through the input window where it can make up to 50 reflections inside the cell. The beam exited the cell through the output window and was focused onto the signal detector. The path lengths between the beam splitter and each detector were matched so that the small absorption caused by the water vapor in the lab air suffered by the beam before and after the beam splitter would be divided out. The angle of the gold coated, low loss mirrors inside the cell could be changed from outside the cell in order to vary the optical path length in increments of roughly 0.7m from 0.4m to 10m. The measurements of the narrow absorption line were performed primarily to test the spectral purity of the pulsed, laser transmitter. The following experimental set up was used to measure the absorption line by scanning the water vapor inside the cell (Fig. 4.3.2).

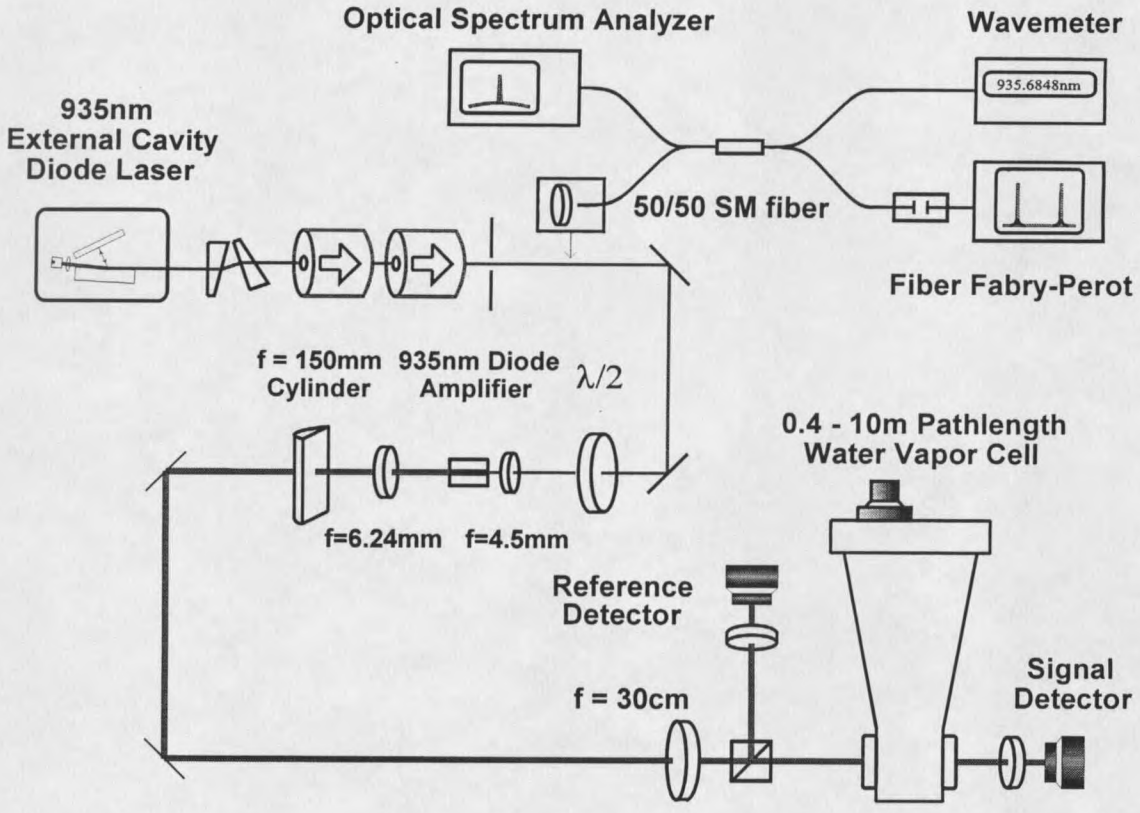


Figure 4.3.2. Experimental set up used to measure the 935.68nm water vapor absorption line at low pressures.

This setup is very similar to that used to measure the water vapor line at 755Torr with a few exceptions. First, the test atmosphere is contained in the optical cell instead of using the air in the lab. Second, the output from the ECDL is amplified and pulsed using the flared amplifier. Because the output beam from the laser transmitter was pulsed, the wavelength was stepped instead of scanned at 25Hz and the peak powers of the pulses were recorded for each step. Using Labview, a computer was used to step the PZT voltage on the ECDL increasing its output wavelength by 0.5pm per step [48]. This wavelength was amplified to 285mW with the flared amplifier over a 1.28μs pulse width at 3.906kHz providing 0.36μJ of energy per pulse. The pulse driver used to drive the

high current modulator was also used to trigger the digitizing oscilloscope which recorded the pulse amplitude from the reference and signal detectors. 98 steps were taken across the 50pm scan. The absorption line below was measured for a path length of 8.75m at a pressure of 5Torr inside the optical cell (Fig 4.3.3).

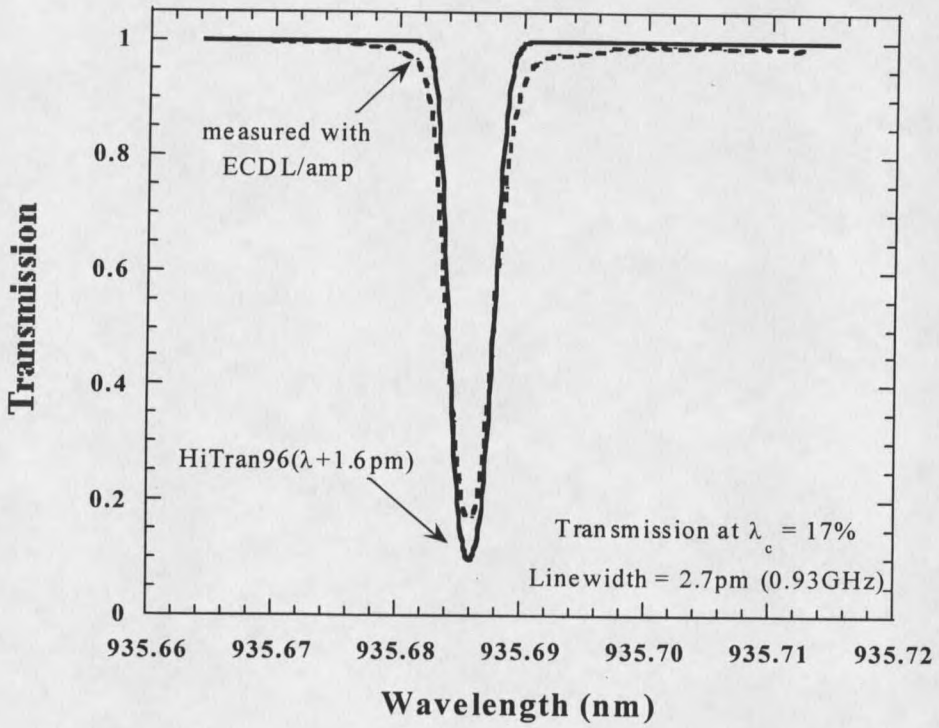


Figure 4.3.3. Comparison of the 935.68nm water vapor absorption line measured at 5Torr using the pulsed ECDL/amplifier (dashed line) with that theoretically predicted by HiTran '96 (solid line). The center wavelength of the calculated line had to be shifted over by 1.2pm because the theoretical prediction did not include the pressure shift in the line from vacuum to 5Torr.

This was the first time a pulsed, high power laser was used to successfully scan across an absorption line by our group at NASA/GSFC. Although the linewidth at half maximum of each line are identical, the measured line differs from the predicted line at the center and at the wings of the profile. This discrepancy arises from excluding the

effects that pressure has on the predicted profile, even at 5Torr. A Voigt profile can more accurately describe the absorption line by factoring in a combination of Doppler and pressure broadening. Selecting the correct Voigt profile becomes tricky when trying to weight the effects of the two types of broadening mechanisms and errors of a few percent in the transmission at line center is not uncommon. In this case, it is likely the measured absorption line profile is more accurate than the predicted profile.

Because the linewidth of the measured profile matches that of the predicted profile, it is unlikely the pulsed output from the amplifier is frequency chirped. As a second verification of the pulsed transmitter's spectral purity, similar scans of the 935.68nm absorption line were made using just the CW output from the ECDL alone, without the amplifier, which is known to be chirp free and have a linewidth of < 2MHz (Fig. 4.3.4)

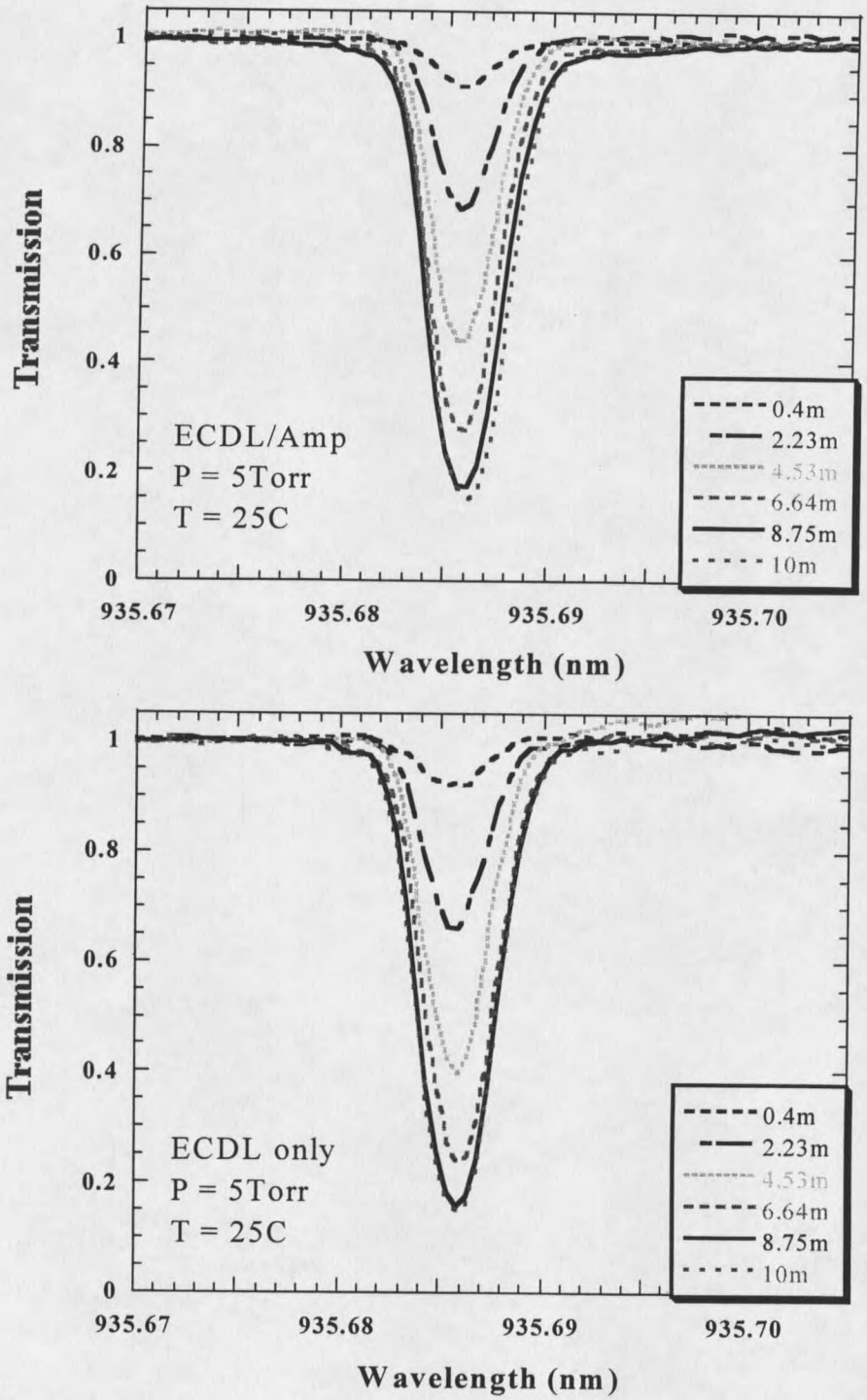


Figure 4.3.4. Comparing scans of the water vapor absorption line at 5T over several path lengths. The scans in the top graph were made using the pulsed ECDL/Amplifier and the bottom scans were made using just the ECDL. The line shapes are identical to those measured using the pulsed, flared amplifier verifying that its frequency output is chirp-free.

Many scans of the water vapor absorption line were made at various pressures and over various path lengths using the pulsed laser transmitter. This generated a lot of data that, when accumulated, could provide even more information about the low pressure atmosphere. For instance, from equation 4.2.5, we expect the transmission through the water vapor at line center to decrease exponentially.

$$T(\nu_o) = e^{-\alpha(\nu_o)\cdot L} \qquad 4.3.3$$

This is just a statement of the familiar Beer-Lambert law of absorption [56]. Therefore, plotting the log of the transmission at line center as a function of path length should result in a straight line whose slope is the absorption coefficient α of the water vapor at a particular pressure (Fig. 4.3.5).

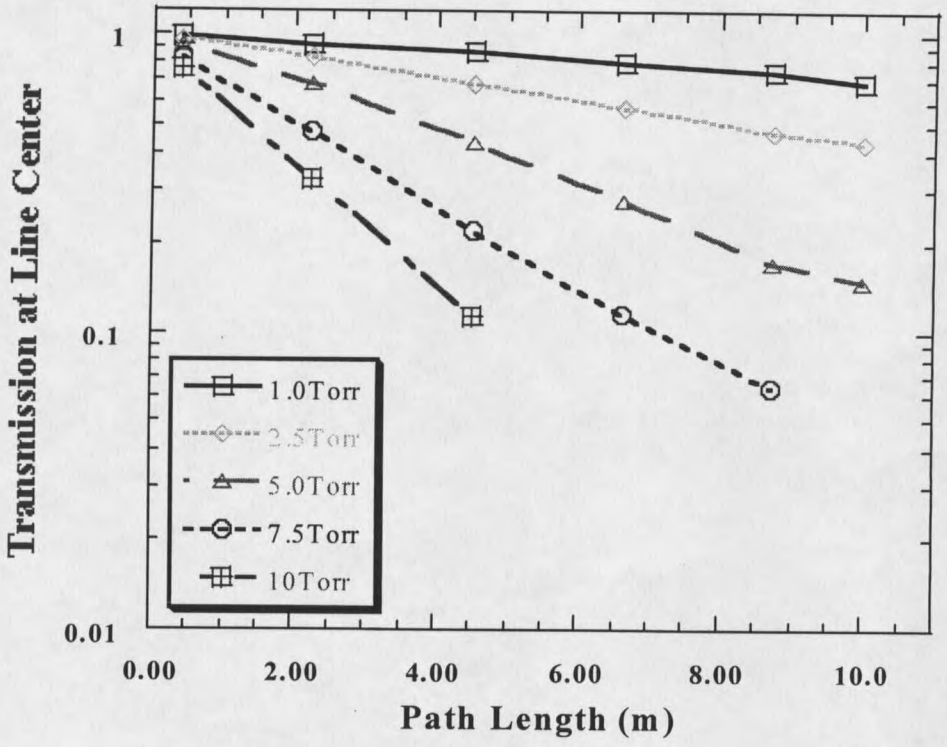


Figure 4.3.5. The transmission at the center of the 935.68nm water vapor absorption line as a function of path length through the low pressure cell. The water vapor completely absorbed the beam at the higher pressures and longer path lengths.

We can also learn how the pressure affects the absorption linewidth. Comparing the full width at half maximum (FWHM) absorption linewidth as a function of the pressure inside the cell for each path length demonstrates that pressure broadening of the line is taking place (Fig. 4.3.6.)

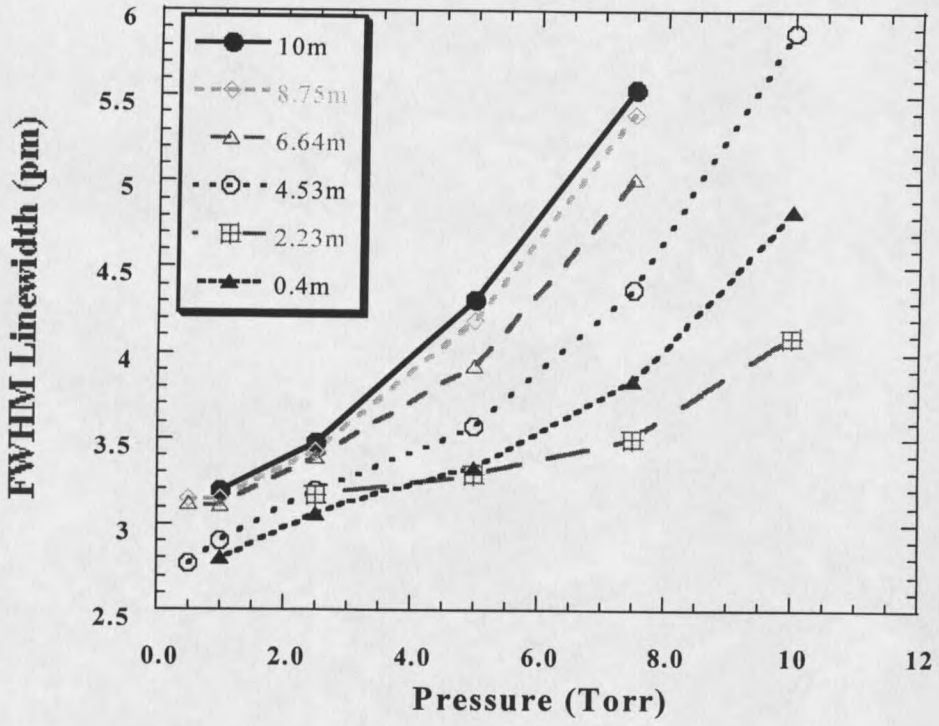


Figure 4.3.6. The FWHM linewidth of the 935.68nm absorption line begins to increase as the water vapor pressure inside the optical cell is increased from 1 to 10Torr.

This increase in linewidth due to pressure varaitions will not likely affect on line/off line lidar measurements because the laser can easily tune to an off line wavelength with zero absorption. However, by monitoring the linewidth by measuring the halfway points up the side of the profile, the unique pressure dependence of the linewidth might provide a sensitive method for measuring the atmospheric pressure as well as the water vapor concentration. This exciting idea could be easily incorporated into the actual lidar system for the Mars Lander and would not only improve the measurements of the water vapor content, but also provide a useful profiles of the atmospheric pressure!

CHAPTER 5

USING LIDAR TO MEASURE ATMOSPHERIC WATER VAPOR CONCENTRATION FROM THE SURFACE OF MARS

5.1 The Atmosphere on Mars

Suppose we were able to package up and send our small lidar system to the surface of Mars. How will it measure the water vapor concentration and to what altitude? We can predict our instrument performance only if we know something about the atmosphere it will be pointed into. Fortunately, this information is available thanks mostly to the observations from the Viking 1 and 2 Landers and Orbiters in 1976. The orbiters carried passive spectrometers known as Mars Atmospheric Water Detectors (MAWD), which globally mapped the quantity of water vapor at all seasons, and Infrared Thermal Mappers (IRTM), used to map the temperature, albedo and thermal inertia of the entire surface [54]. Using the Viking Landers as a reference point for calibration, the orbiters provided profiles of the temperature and pressure of the atmosphere as they passed over the Landers. In addition, CCD cameras on the Landers were able to perform sky brightness measurements by imaging the solar-illuminated sky at three infrared wavelengths, including views where the sun had set or was about to rise, and direct views of the sun at a wavelength of 670nm [57]. These optical depth measurements, together

with the MAWD and IRTM data, provided the temperature and pressure profile below at the Viking Lander 2 site (Fig. 5.1.1).

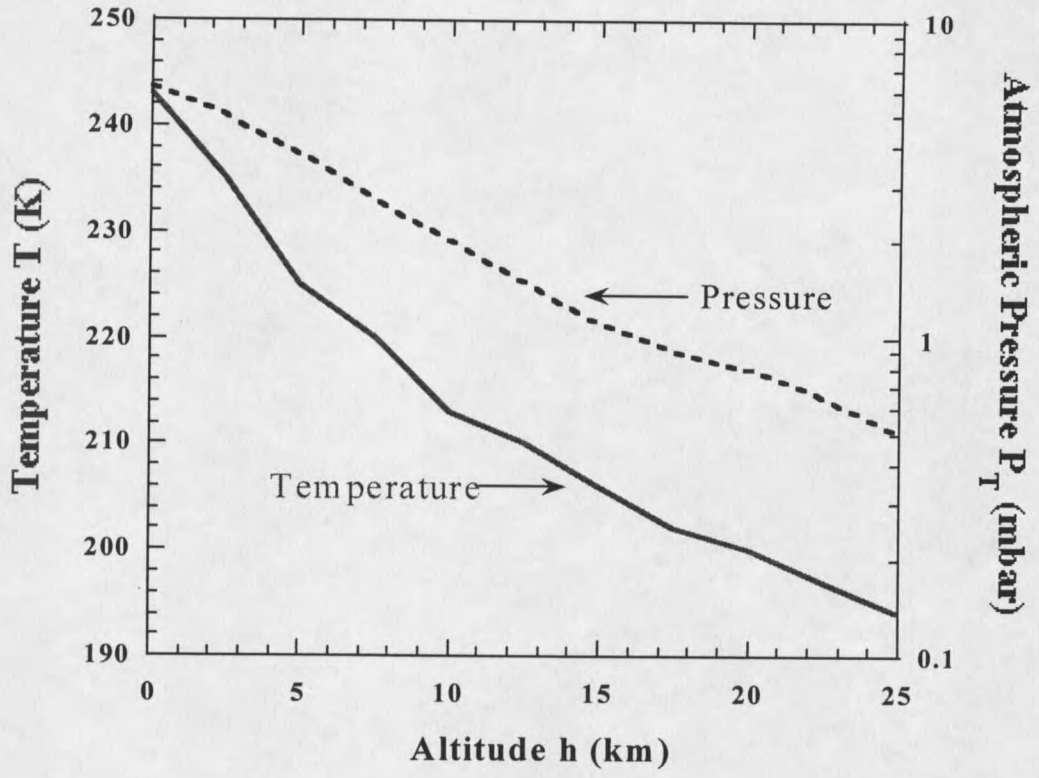


Figure 5.1.1. during Ls = 90. A pressure of 6.1mbar at the Temperature and pressure profiles at the Viking 2 Lander site surface corresponds to 4.6torr or 0.0060atm.

Now 21 years later, the Pathfinder mission verified the Viking Lander data by measuring very similar temperature profiles [58]. A profile of the atmospheric water vapor density could then be generated by combining the water vapor measurements made by MAWD with the above temperature and pressure profiles [57].

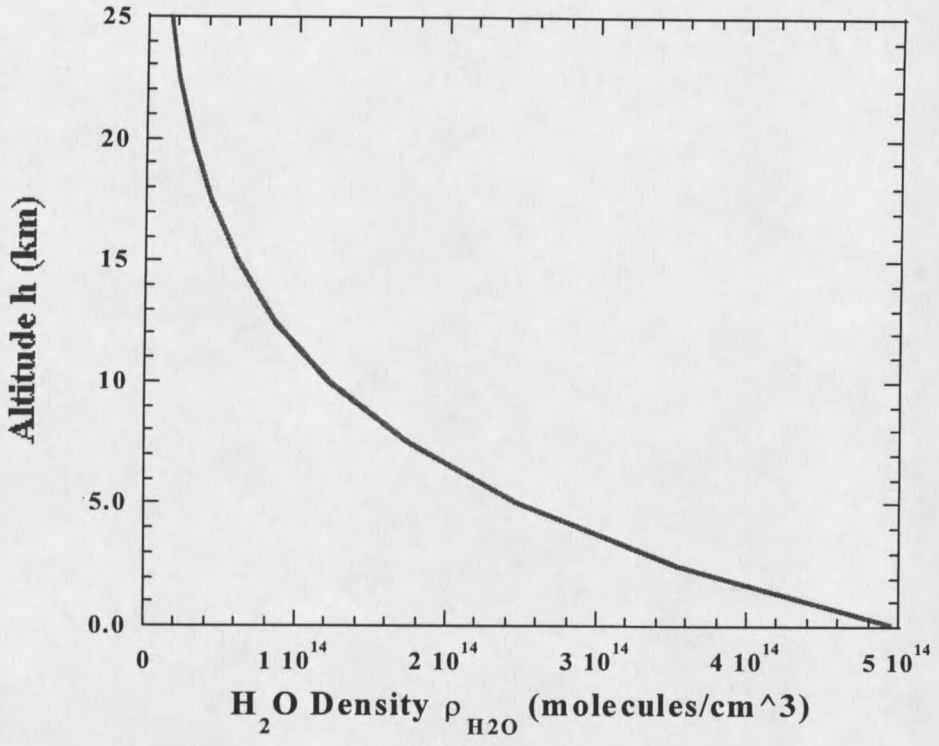


Figure 5.1.2. Vertical profile of water vapor density at the Viking Lander 2 site during Ls = 270.

This profile of the water vapor concentration represents the primary measurement goal for our water vapor lidar instrument! Determining the density of water vapor allows us to calculate the partial pressure of the water vapor P_{H2O}, mass and volume mixing ratio, and relative humidity just as we did in section 4.2. It is fun to compare the small amount of water vapor found in the atmosphere on Mars with that in Earth's atmosphere (Fig. 5.1.3).

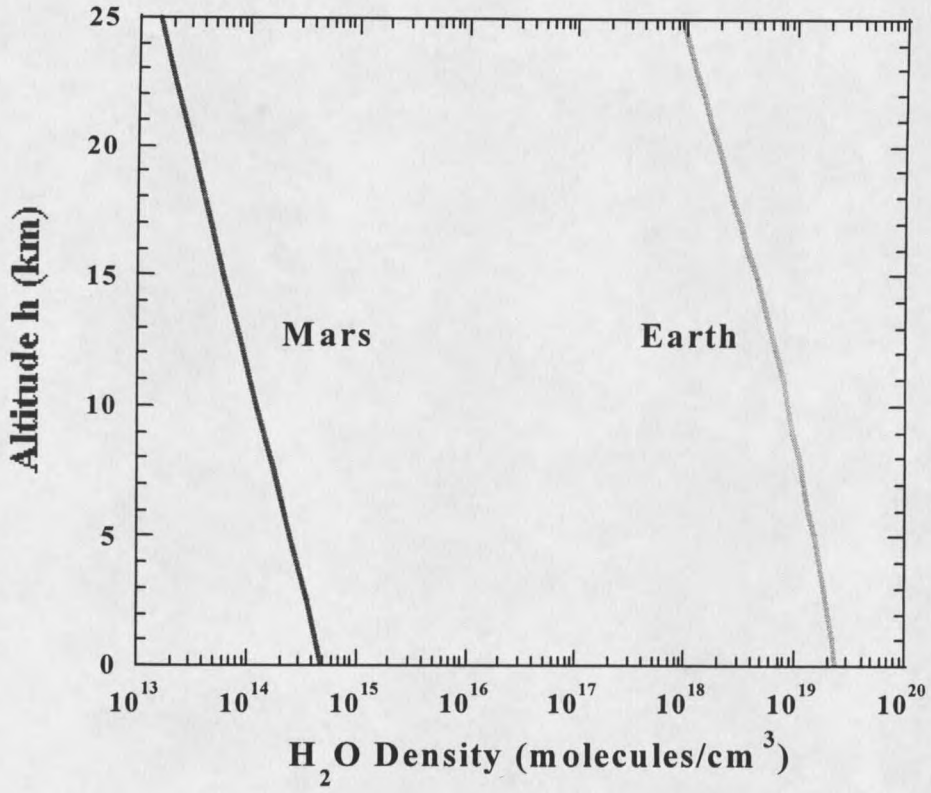


Figure 5.1.3. The atmospheric water vapor concentration on Earth is 50,000 times greater than on Mars!

It is interesting to note that the more recent Mars Pathfinder measured the water vapor content in a similar matter as did the Viking 2 Orbiter and Lander. The imager for Mars Pathfinder (IMP) is a stereoscopic CCD camera containing 12 selectable filters for spectroscopic studies. To measure the water vapor content in the atmosphere, the camera would look at the sun just after sunrise and just before sunset to provide the longest possible path length through the atmosphere. A 4.91nm narrow bandwidth filter at λ = 935.6nm was positioned in front of one eye and a 5.03nm narrow band filter at λ = 924.9nm was positioned in front of the other eye to simultaneously measure the on line

versus off line absorption [59]. Two more filters at 935.4 and 945.5nm were available for on line measurements and two additional filters at 883.4nm and 988.9nm were used to measure the off line, or continuum, measurements. While providing useful information, these measurements taken on the most recent Lander mission estimate the water vapor concentration only twice a day and still lacks directly measured, ranged resolved profiles. Our lidar instrument will be able to measure accurate profiles of water vapor concentration at least every half hour, day and night, providing new and important information about the dynamics of the lower atmosphere.

5.2 How the Lidar will Measure Atmospheric Water Vapor Concentration

This lidar system will use the differential absorption lidar, or DIAL, technique to measure the atmospheric water vapor concentration. The laser transmitter emits pulses of light into the atmosphere whose wavelength either lies at the center of the water vapor absorption line, λ_{on} or lies off to one side of the absorption line, λ_{off}. Fractions of the pulsed beam are scattered back to the lidar receiver from various altitudes by aerosols and molecules in the atmosphere. If the two wavelengths, λ_{on} and λ_{off} are within a 100GHz of each other, the elastic scattering properties of the atmosphere are assumed to be identical. Therefore the complicated scattering processes for each wavelength pulse can be divided out by taking the ratio of the on-line/off-line signal. The ratio leaves only the information about the absorption of the on-line pulse as it travels through the atmosphere. The lidar receiver will measure the number of photoelectrons per time as the back-scattered signal is collected by the photon counting detectors. Roughly two photoelectron counts will be generated for each return photon. The rate at which the number of photoelectrons are counted can be described using the single-scattering lidar equation [41,56,60].

$$\frac{dn}{dt}(h) = \frac{E_{pulse}}{E_{h\nu}} \cdot \frac{\Delta R}{h^2} \cdot \xi(h) A_{rec} \tau_{rec} \eta_{QE} \left[\beta_a(h) + \beta_m(h)\right] \cdot \left[T_a(h) T_m(h) T_\lambda(h)\right]^2 \qquad 5.2.1$$

This expression assumes that the light was scattered only once before being collected by the receiver. Light scattered more than once has a low probability of returning back to the receiver, having little effect on the count rate. A description of each variable follows:

E_{pulse} = pulse energy from laser transmitter (peak power)(pulse width) in Joules

$E_{h\nu}$ = photon energy = hc/λ at 935.68nm in Joules

ΔR = length of range bin = 2c(pulse width)/2 in km

h = altitude measured from the surface in km

$\xi(h)$ = transmitter/receiver geometric overlap factor

A_{rec} = receiver area of the 12" Cassegrainian telescope in m^2

τ_{rec} = transmission efficiency of the telescope optics

η_{QE} = quantum efficiency of the photon counting detectors

$\beta_a(h)$ = aerosol backscatter coefficient in 1/(km steradians)

$\beta_m(h)$ = molecular backscatter coefficient in 1/(km steradians)

$T_a(h)$ = net transmission through the aerosols

$T_m(h)$ = net transmission through the atmospheric molecules

$T_\lambda(h)$ = net transmission with λ on or off the water vapor line

Notice that the photo electron count rate dn/dt has a direct dependence on the pulse energy of the laser E_{pulse} and inverse dependence on the square of the altitude h^2. This dependence is largely responsible for a weak return signal which is why it is so important to maximize the peak output power from the laser transmitter. The lidar equation not only describes the pulsed output parameters of the laser transmitter, but also the collection efficiency of the receiver. It also includes contains a description about the light scatters and transmission through the aerosols and molecules in the atmosphere. The "aerosols" in the Martian atmosphere refer primarily to dust, but can also include water ice and CO_2 ice particles. The model used to determine the backscatter and transmission coefficients will be discussed next.

Backscatter Coefficients for the Atmosphere

Fortunately for our lidar system, the atmosphere on Mars is very dusty and provides a strong, back scattered signal to the receiver. The Viking mission estimated the average radius of the dust particles to be $1.85 \pm 0.3\mu m$, now in slight disagreement with 1.0 (+0.3, -0.2) μm radius recently estimated by the Mars Pathfinder [61]. In either case, the average particle size is greater than the wavelength of the transmitter, and therefore elastically scatters the light with high efficiency. The density of aerosols can vary significantly from place to place and from one time to another, making it virtually impossible to accurately predict the expected aerosol scattering contribution to a particular lidar signal. However, I was fortunate to have met an expert on aerosol scattering at NASA/GSFC, Dr. James Spinhirne [62]. He has developed a scattering model based on his extensive lidar measurements and others [63,64]. Dr. Spinhirne derived coefficients specifically describing the atmosphere on Mars for his model presented in [60] which were based on an extensive study of available Mars data. The vertical distribution for the aerosol scattering cross section σ(h) can be estimated by:

$$\sigma_a(h) = \lambda_{cal}\sigma_o(1+a)^2 \frac{e^{\frac{h}{b}}}{\left(a+e^{\frac{h}{b}}\right)^2} + \lambda_{cal} f(1+a')^2 \frac{e^{\frac{h}{b'}}}{\left(a'+e^{\frac{h}{b'}}\right)^2} \qquad 5.2.2$$

This model was developed for a ruby laser at a wavelength of 694.3nm. It can be calibrated to the wavelength of our lidar system by:

$$\lambda_{cal} = \frac{694.3nm}{\lambda} \cdot 1.5 \rightarrow 1.11 \text{ for } \lambda = 935.7\text{nm} \qquad 5.2.3$$

The factor of 1.5 is used to strengthen the scattering cross section due the large scattering size of the atmospheric aerosols. Values for the constants in equation 5.2.2 specific to the atmosphere on Mars are:

$\sigma_o = 0.025$ 1/km; $f = 6x10^{-6}$ 1/km

$a = 0.4$; $a' = 2981$

$b = 3.2$ km; $b' = 5.0$ km

The aerosol backscatter coefficient results from dividing the scattering cross section $\sigma_a(h)$ by constant, S_p, that is representative of tropospheric aerosols [65]. For instance, $S_p = 1$ if the particle could scatter 100% of the incident light directly backwards toward the receiver. However, depending on the shape of the particle, it can scatter the light over 4π steradians. The particle of index of refraction n can also partially absorb the light, further reducing the backscattered light. This extinction-to-backscatter ratio S_p can have values from 10 to 100 steradians and is assumed to be independent of altitude. For this model, $S_p = 30$ steradians for an aerosol backscatter coefficient β_a in 1/(km steradians):

$$\beta_a(h) = \frac{\sigma_a(h)}{S_p} \qquad 5.2.4$$

The back scattered light from atmospheric molecules is much weaker than that of the aerosols mainly because of the lack of available scatters in the thin atmosphere. The molecular scattering cross section follows the familiar $1/\lambda^4$ dependence of Raleigh scattering given by [56]

$$\sigma_m(h) = \frac{8\pi}{3}\left(\frac{\pi^2(n^2-1)^2}{\rho_{air}^{\ 2}\lambda^4}\right) \qquad 5.2.5$$

ρ_{air} is the number density of scattering molecules assumed to have an oscillator strength of 1. The index of refraction n depends on the species of molecules making up the atmosphere. Table 5.2.1 below lists the atmospheric composition and their natural abundance in the Martian atmosphere [54].

Table 5.2.1. Atmospheric composition of Mars by volume.

Species	Abundance
CO_2	0.9532
N_2	0.027
Ar	0.016
O_2	0.0013
CO	0.0007
H_2O	0.0003
Ne	2.5 ppm
Kr	0.3 ppm
Xe	0.08 ppm
O_3	0.04 to 0.02 ppm

Since the Martian atmosphere is composed almost entirely of CO_2, a scattering cross section in 1/km was calculated using values for this gas found in Table 2.3 of [56]:

$$\sigma_m(h) = \frac{8\pi}{3} \cdot \left[16.15 \cdot \left(\frac{550}{\lambda} \right)^4 \cdot 10^{-28} \right] \cdot \rho_{air}(h) \cdot 10^5 \qquad 5.2.6$$

The density of the "air" $\rho_{air}(h)$ was derived from the ideal gas law and the temperature and pressure profiles provided in figure 5.1.1. An exponential fit was used to describe this density profile in molecules/cm^3

$$\rho_{air}(h) = 1.818 \times 10^{17} \cdot e^{-(0.9 \cdot h + 0.0002 \cdot h^2)} \qquad 5.2.7$$

The backscatter coefficient, in 1/(km steradians) is just the scattering cross section $\sigma_m(h)$ above before integrating over 4π steradians.

$$\beta_m(h) = \frac{3}{8\pi} \cdot \sigma_m(h) \qquad 5.2.8$$

For this particular atmosphere, the molecular backscatter is typically over 200 times less than the backscatter from aerosols. Therefore, our lidar system is very dependent on the backscatter from aerosols. Finally, the total backscatter coefficient is the sum of the molecular and the aerosol backscatter coefficients.

$$\beta(h) = \beta_a(h) + \beta_m(h) \qquad 5.2.9$$

A plot of the total backscatter from the atmosphere is plotted below (Fig. 5.2.1).

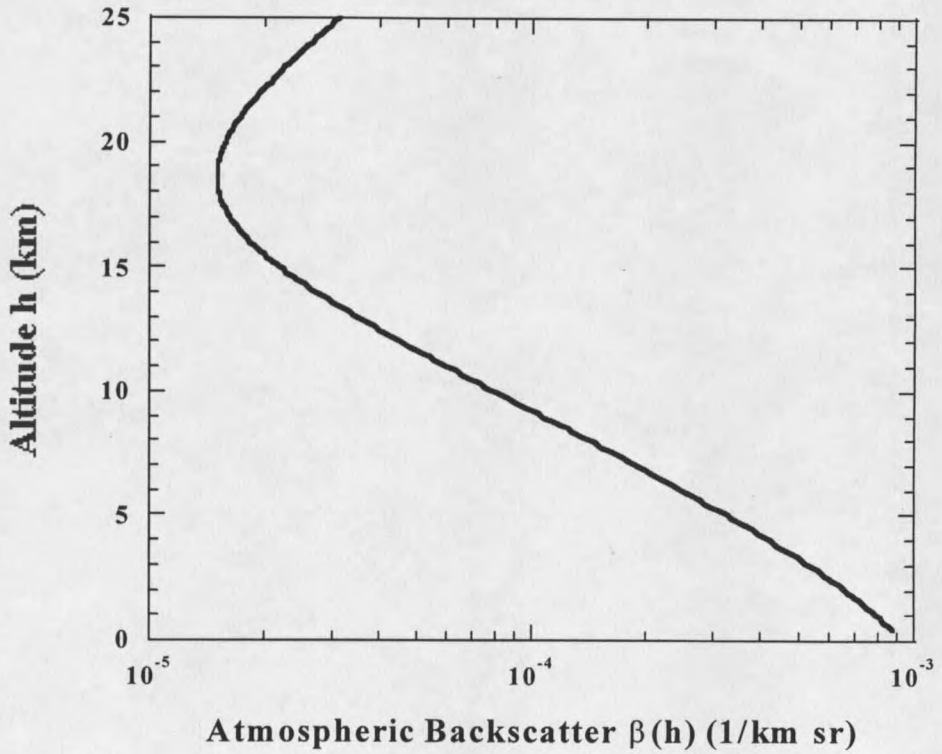


Figure 5.2.1. The net backscatter of the lidar signal from the molecules and aerosols in the Martian atmosphere.

This plot shows that we can expect only 1 out of every 1000 to 66,000 photons to scatter back towards the lidar receiver!

Transmission Through the Atmosphere

The scattering due to atmospheric aerosols and molecules can also work against us by attenuating the lidar signal. The net transmission through just the aerosols in the atmosphere can be estimated using the differential form of the Beer-Lambert equation and the absorption cross section given in equation 5.2.2.

$$T_a(h) = e^{-\int_0^h \sigma_a(h')dh'} \qquad 5.2.10$$

Similarly the net transmission through just the molecules in the atmosphere can be estimated using a similar expression, but replacing the scattering cross for aerosols with that in equation 5.2.6 for molecules.

$$T_m(h) = e^{-\int_0^h \sigma_m(h')dh'} \qquad 5.2.11$$

Once again the molecules have little effect on the net transmission because the low atmospheric density. The total round trip transmission of light through this atmosphere is the multiplication of the square of the aerosol and molecular transmission.

$$T_{am}^{\ 2}(h) = T_a^{\ 2}(h) \cdot T_m^{\ 2}(h) \qquad 5.2.12$$

A plot of the round trip transmission through the atmosphere is plotted below (Fig. 5.2.2)

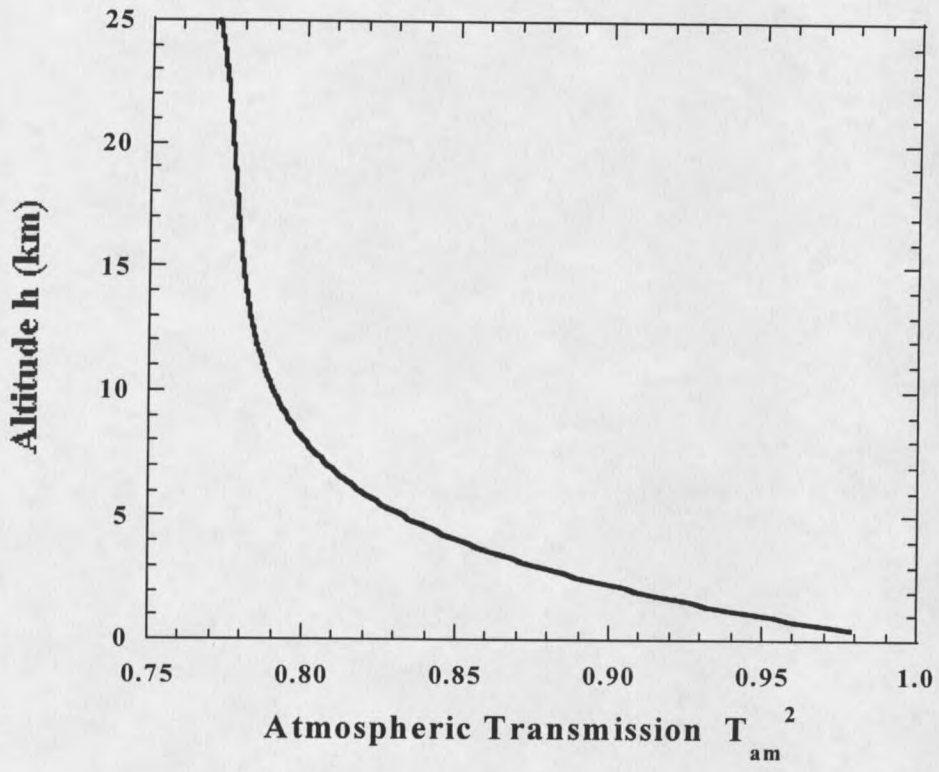


Figure 5.2.2. The net round trip transmission of the lidar signal through the Martian atmosphere is reduced by aerosols and molecular scattering losses.

The transmission is reduced even further when the wavelength of the lidar signal lies at the center of a water vapor absorption line. This reduced transmission due to absorption by the water vapor can be estimated using the HiTran '96 parameters for the 935.68nm absorption line. Because the atmospheric pressure will be 5Torr or less, the linewidth is primarily Doppler broadened. Therefore the Doppler halfwidth γ_D from equation 4.3.1 can be used to model the absorption line.

$$\gamma_D = \frac{\nu_o}{c} \cdot \left(2RT(h) \frac{\ln(2)}{M_{H_2O}} \right)^{\frac{1}{2}} \cdot 10^{\frac{3}{2}} \qquad 5.2.13$$

The atmospheric temperature as a function of altitude h in the above expression can be described by a third order polynomial fit to the temperature profile given in figure 5.1.1.

$$T(h) = 243.43 - 4.1600 \cdot h + 0.14341 \cdot h^2 - 0.0022379 \cdot h^3 \qquad 5.2.14$$

This halfwidth is used to calculate the strength of the absorption using the Gaussian profile of 4.3.2. At the center of the absorption, $\nu = \nu_o$, simplifying this expression to:

$$g(h) = \frac{1}{\gamma_D(h)} \cdot \left(\frac{\ln(2)}{\pi}\right)^{\frac{1}{2}} \qquad 5.2.15$$

The absorption cross section $\sigma_{H2O}(h)$ in cm^2/molecule is just the product of the line intensity S with the above expression g(h).

$$\sigma_{H2O}(h) = S \cdot g(h) \qquad 5.2.16$$

An exponential fit is used to describe the vertical profile of the atmospheric water vapor density in molecules per cm^3 given in figure 5.1.2.

$$\rho_{H2O}(h) = 4.9913 \times 10^{14} \cdot e^{-0.13987 \cdot h} \qquad 5.2.17$$

Although this information is exactly what we hope to measure using our lidar system, it will be used here to estimate the photoelectron count rate we can expect to receive for the on line signal. Because the absorption cross section and the water vapor density vary with altitude, we must determine the transmission through the atmosphere at the center of the absorption line using the differential form of the Beer-Lambert equation.

$$T_{online}(h) = e^{-\int_0^h \sigma_{H2O}(h') \cdot \rho_{H2O}(h') \cdot 10^5 \, dh'} \qquad 5.2.18$$

The factor of 10^5 converts the units of integrand from 1/cm to 1/km. The strong, 935.68nm absorption line causes a large reduction in the net round trip transmission of

the on-line wavelength lidar signal, even though there is very little water vapor in the atmosphere (Fig. 5.2.3).

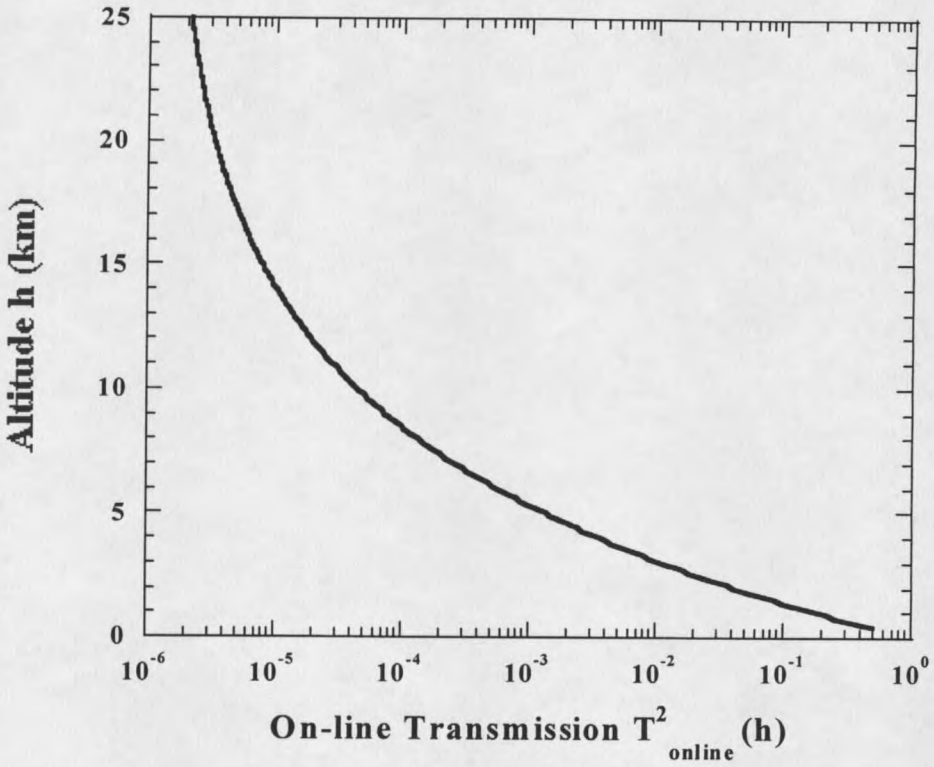


Figure 5.2.3. The net round trip transmission of the lidar signal through the Martian atmosphere is reduced by the absorption of the water vapor at λ_{online} = 935.68nm.

The off-line wavelength lidar signal will suffer very little if any absorption loss due to the water vapor absorption. This will provide a large signal ratio between the on-line and off-line measurements for a good estimate of the absorption due to water vapor.

Evaluating the Return Lidar Signal

The optical receiver for the bread board water lidar system has already been assembled and tested at NASA/GSFC for a similar semiconductor lidar system at λ = 670nm used to measure the height of clouds in the Antarctic (Fig. 5.2.4).

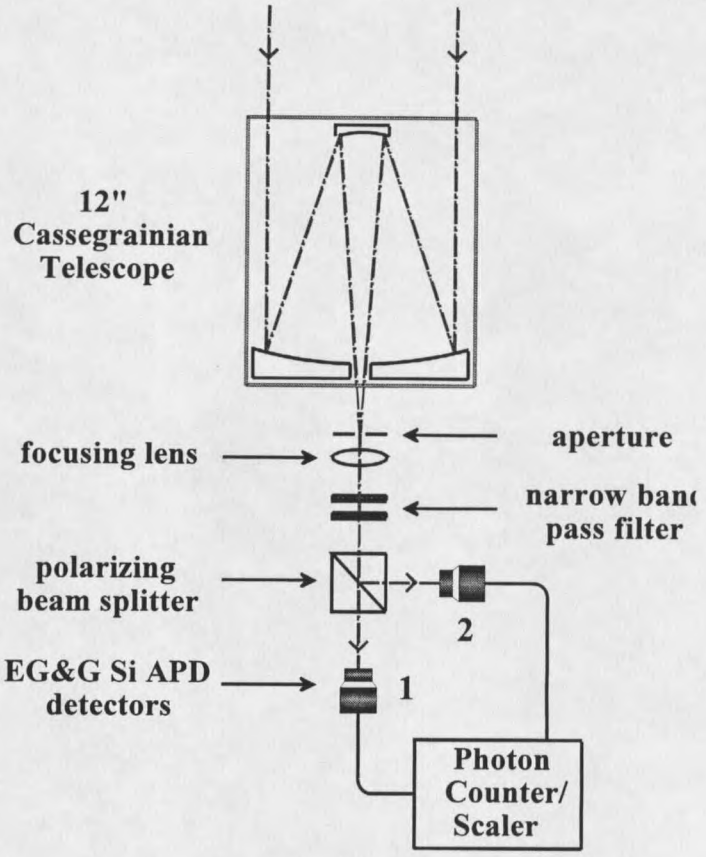


Figure 5.2.4.. Schematic of the bread board lidar receiver. The actual Mars lidar will likely have a lightweight, 5.1" diameter beryllium telescope for required mass and size constraints.

The primary component of the receiver is a 12" diameter, Cassegrainian telescope used to collect the back scattered photons. A small aperture is used to match the acceptance angle of the telescope to the divergence angle of the laser transmitter in order to filter out as much stray background light as possible. The light then passes through a very narrow

band, etalon-type filter, centered between λ_{on} and λ_{off}, used to spectrally filter out the stray background light. Next, the light passes through a polarized beam splitter which serves two functions. First, the polarized light from the transmitter which was back scattered by the aerosols will pass through the beam splitter to the detector #1. Any portion of the transmitter pulse that is scattered off of ice particles in the atmosphere will have its polarization rotated by the birefringent properties of the ice and be partially recorded by the detector #2. The ratio of the two detectors can then be used to measure the profile of the ice crystals and track their dynamical processes. This will be an important compliment to the water vapor measurements, especially when the water freezes at night as the temperature drops. Second, the beam splitter will filter out half of the unpolarized signal to detector #1 from the background light originating from the sunlit atmosphere. Although the parameters have been measured for this receiver at λ = 670nm, the optics in the system such as the focusing lens, narrow band pass filter, and beam splitter can be easily replaced with identical optics AR coated at 935nm.

Table 5.2.2..Typical values for the optical parameters of the lidar receiver.

Receiver Parameter	**Value**
Transmitter/receiver geometric overlap factor, $\xi(h)$	$\simeq 1$
Receiver area of 12" Cassegrainian telescope, A_{red}	$0.292m^2$
Transmission efficiency of the telescope optics, τ_{rec}	$\simeq 0.30$ or 30%
Quantum efficiency of each Si, APD photon counting detector, η_{QE}	0.45 or 45%
Narrow band pass filter/etalon, $\Delta\lambda_{BP}$	10pm FWHM

In the above table, $\xi(h)$ describes the geometrical overlap of the transmitter beam with the receiver field of view, as illustrated below (Fig. 5.2.5).

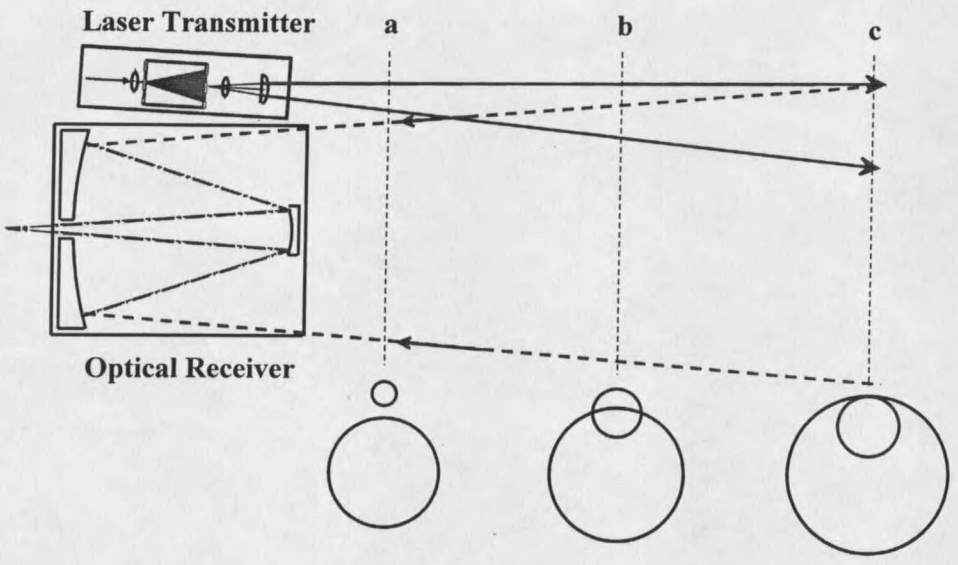


Figure 5.2.5. Geometrical overlap $\xi(h)$ of the transmitted beam with the receiver field of view.

The laser transmitter is tilted slightly so that its beam overlaps with the field of view of the receiver. However, at low altitudes near the lidar system, there can be a) no overlap, b) partial overlap or finally c) complete overlap. This will tend only to reduce the signal received in the first couple of range bins. For simplicity, I let $\xi(h) = 1$ for all h realizing that the predicted signal will be higher than it will actually be in the first couple of range bins.

We are now ready to apply all the parameters describing the transmitter and receiver and the estimates of the atmospheric backscatter and transmission to the lidar equation. We will scan the laser transmitter on and off the line at a 50Hz rate, and send out two pulses per scan, λ_{on} and λ_{off}. This will increase the photoelectron count rate by a factor of 50 for each wavelength. For the off line pulse, T_λ becomes $T_{offline} = 1$ so that the off line count rate dn/dt becomes:

$$\frac{dn_{offline}}{dt}(h) = 50 \cdot \frac{E_{pulse}}{E_{h\nu}} \cdot \frac{\Delta R}{h^2} \cdot \xi(h) A_{rec} \tau_{rec} \eta_{QE} \left[\beta_a(h) + \beta_m(h)\right] \cdot \left[T_a(h) T_m(h) \cdot 1\right]^2 \qquad 5.2.19$$

For the on line pulse, the transmission T_λ becomes T_{online} whose values were determined using HiTran parameters along with temperature and water density profiles estimated by the Viking mission. The count rate dn/dt for the online pulse becomes:

$$\frac{dn_{online}}{dt}(h) = 50 \cdot \frac{E_{pulse}}{E_{h\nu}} \cdot \frac{\Delta R}{h^2} \cdot \xi(h) A_{rec} \tau_{rec} \eta_{QE} \left[\beta_a(h) + \beta_m(h)\right] \cdot \left[T_a(h) T_m(h) T_{online}(h)\right]^2 \qquad 5.2.20$$

The lidar receiver can integrate this count rate over time, generating a histogram of the total number of counts per range bin. This effectively time averages the return signal of the atmosphere. Integrating over a longer time will reduce the uncertainty in the results at the cost of loosing information about the dynamic behavior of the atmosphere on short time scales. A good compromise for our system is to let it integrate the signal for 20 minutes, which will certainly provide much more information than the twice a day rates of previous missions. The total number of counts recorded by the receiver is then:

$$\begin{aligned} n_{offline}(h) &= \frac{dn_{offline}}{dt}(h) \times \text{integration time}, \\ n_{online}(h) &= \frac{dn_{online}}{dt}(h) \times \text{integration time} \end{aligned} \qquad 5.2.21$$

The off-line and on-line count rates we expect to receive as a function of altitude is plotted below (Fig. 5.2.6).

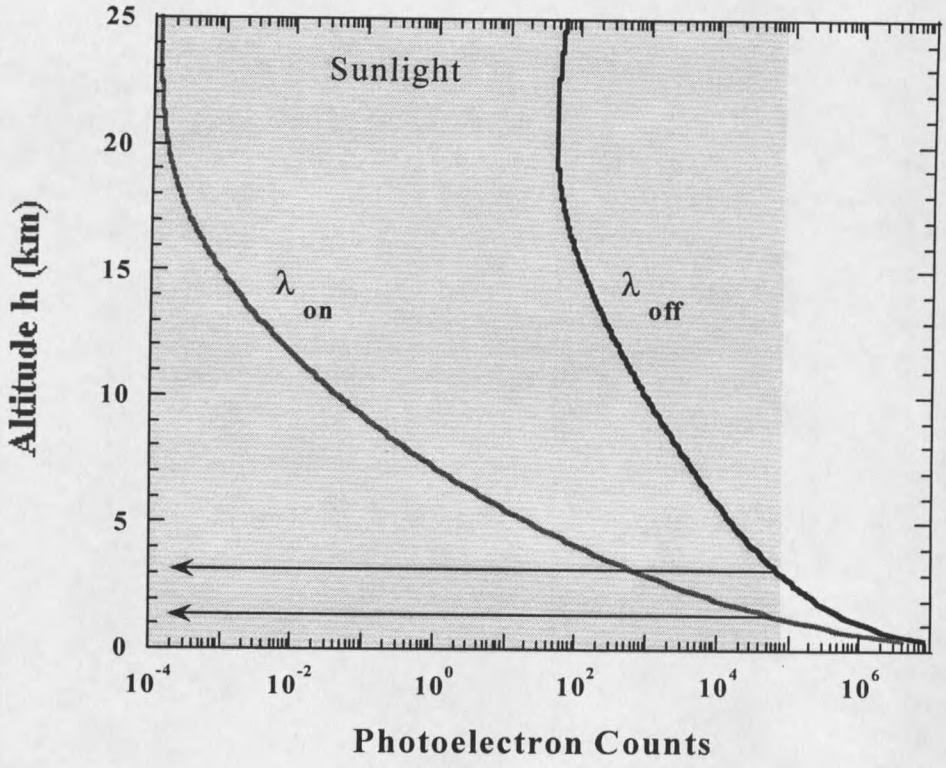


Figure 5.2.6. Predicted number of photoelectron counts from the lidar receiver for λ_{on} and λ_{off} wavelength pulses. Approximately 68,000 background counts from the sunlight will limit the maximum altitude the on-line signal can measure to only 1.33km.

The recent Mars Pathfinder mission was able to measure the brightness of the Martian sky during the day and found that, when looking 30^0 azimuth angle from the sun, the brightness measured 100Watts/(m^2 sr μm) [61]. In spite of the attempts to optically filter out the background light, the sunlit atmosphere provided a whopping 68,000 counts which dominated the number of counts from the lidar signal over almost the entire range! In fact, the background counts limit the on-line altitude to only 1.33km and the off-line altitude to 3.19km. How can the range of this lidar system be increased?

The most obvious suggestion is to increase the peak output power of the laser transmitter. This is already under way. A new custom flared amplifier chip has already

been developed and delivered to NASA/GSFC for testing in our bread board transmitter. This devices promises to increase the output power to 3W, at least 10 times more power than the current amplifier will generate. This will increase the maximum on-line altitude to 2.1km and the off-line amplitude to 6.4km. Perhaps the 935nm ECDL can simultaneously seed multiple amplifiers. This will also be tested soon.

A second suggestion involves replacing the 10pm wide band pass filter with a stabilized high finesse cavity. In our lab, we have designed and assembled high finesse Fabry-Perot cavities with transmission linewidths on the order of 200kHz [66]. The mirror spacing in these high-finesse cavity can be adjusted or scanned by applying a voltage to a PZT attached to the mirrors. The distance between the mirrors of the cavity could be designed to provide two optical resonances whose wavelength spacing matches the on wavelength spacing of the on-line/off-line pulses. These optical resonances would provide two, very narrow filters whose center wavelength could be frequency locked to the on-line/off-line wavelength pulses. A fraction of each output pulse could be directed immediately into the telescope using a corner cube which can be used to lock the cavity to the wavelength pulse. A conservative estimate predicts the background light could be reduced by a factor of 500, increasing the maximum on-line altitude to nearly 4km and the off-line altitude to over 14km using the current laser transmitter output. The high finesse cavity would ease the power requirements of the laser transmitter for daytime lidar measurements while maintaining the simplicity of the original receiver.

A final suggestion would be to measure the atmospheric profiles every time except for midday. Early morning and late evening measurements promise interesting dynamics as

the ice transforms into water vapor through sublimation and then later freezes as the temperature drops. The instrument could also be designed to point more horizontally, away from the sun and look for plumes of water vapor which would identify attractive locations for later missions to look for life. In any case, it is important to remember that these results are based on many estimates about the atmosphere on Mars and, even challenged by a bright sunny day, our bread board lidar system would still provide us useful information that is not currently known.

Using DIAL to Measure Atmospheric Water Vapor Concentration

The photon counting detectors in the receiver will emit a single pulse of photocurrent for every two photons collected. These "photoelectron counts" are sent to a multi-channel scaler which places each count in a range bin according to its arrival time relative to the output pulse. Over time, the scaler adds up all the counts in each bin forming a histogram describing an altitude profile of the number of back scattered photons. How can the water vapor density of the atmosphere be derived from the number of photoelectron counts?

The lidar equations 5.2.19 and 5.2.20 show that the photoelectron count rate is directly related to the net transmission of the lidar signal through the atmosphere reduced by the absorption of water vapor. When multiplied by the integration time, the count rate becomes the total number of integrated counts as shown in 5.2.21. By taking the ratio of the on-line to off-line counts, all transmitter and receiver parameters divide out as well as the scattering processes, leaving only the round trip transmission due to water vapor.

$$\frac{n_{online}(h)}{n_{offline}(h)} = T^2{}_{online}(h) \qquad 5.2.22$$

Recall that $T^2_{offline}(h) = 1$ when the wavelength pulse lies off the absorption line. The on-line transmission is described by the differential from of the Beer-Lambert equation in 5.2.18. The differential absorption (DIAL) technique compares the transmission at an altitude h with that of a neighboring range bin, h +ΔR. We can assume that the absorption cross section σ_{H2O} and the water vapor density ρ_{H2O} are constant across the short range bin, ΔR. In that case, the change in transmission across the range bin of length ΔR is:

$$T_{online}(h+\Delta R) - T_{online}(h) = e^{-\sigma_{H2O}(h)\cdot\rho_{H2O}(h)\cdot 10^5\cdot \int_h^{h+\Delta R} dh'} \qquad 5.2.23$$

Performing the simple integration and substituting the ratio of the photoelectron counts in for the transmission at the appropriate altitude, the above express takes the from:

$$\sqrt{\frac{n_{online}(h+\Delta R)}{n_{offline}(h+\Delta R)}} - \sqrt{\frac{n_{online}(h)}{n_{offline}(h)}} = e^{-\sigma_{H2O}(h)\cdot\rho_{H2O}(h)\cdot 10^5\cdot\Delta R} \qquad 5.2.24$$

By first taking the natural log of both sides of the above equation, we can solve 5.2.24 for the density of water vapor $\rho_{H2O}(h)$.

$$\rho_{H2O}(h) = \frac{-1}{\sigma_{H2O}(h)\cdot 10^5\cdot\Delta R}\cdot\frac{1}{2}\cdot\ln\left[\frac{\frac{n_{online}(h+\Delta R)}{n_{offline}(h+\Delta R)}}{\frac{n_{online}(h)}{n_{offline}(h)}}\right] \qquad 5.2.25$$

This is how we can turn our lidar signal into a valuable measurement of water vapor concentration! To be accurate, 5.2.25 actually calculates the density at the middle of the range bin, $\rho_{H2O}(h+\Delta R/2)$, and not at the exact altitude h. As a check, the water vapor

density profile from the "measured" lidar signal shown below should agree with the initial density profile in figure 5.1.2 modeled from the Viking mission (Fig. 5.2.7)

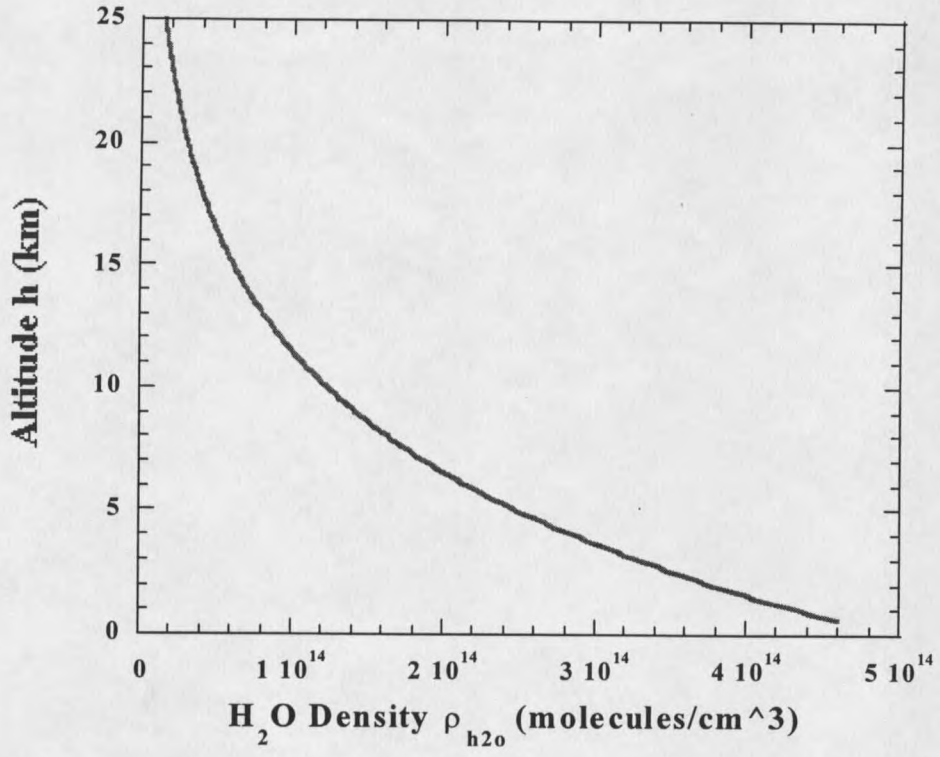


Figure 5.2.7. Vertical profile of the water vapor density "measured" by our lidar instrument using the DIAL technique.

Although the current lidar system would be limited to measuring low altitudes, it would be able to measure accurate profiles of water vapor concentration frequently, at least every half hour, day and night, providing new and important information about the dynamics of the lower atmosphere. Relatively simple improvements can be made to increase the output power of the transmitter and reduce the background signal from the sunlit atmosphere which will enable the lidar to reach higher altitudes. This instrument would provide direct detection of atmospheric water vapor, aerosols and ice crystals,

including their dynamical processes, which are critical to the understanding of the present and past climate on Mars.

CHAPTER 6

CONCLUSION

A compact, efficient, all-semiconductor laser transmitter was developed and tested to demonstrate the feasibility of building a novel, low power miniature lidar system that could measure the atmospheric water vapor concentration on Mars.

A unique, single mode, narrow linewidth, external cavity diode laser (ECDL) was developed specifically for this project to be the master oscillator of laser transmitter. The wavelength of the laser's output could be continuously scanned across the 935.68nm water vapor absorption line. The CW output of the ECDL was amplified and pulsed using a flared semiconductor amplifier. By pulsing its drive current, the amplifier delivered 285mW of optical power whose narrow linewidth was free from frequency chirp. The master oscillator, power amplifier laser transmitter emitted 0.36μJ pulses at 4kHz needing less than 0.5W of electrical power.

The laser transmitter was used to measure the absorption profile of the 935.68nm water vapor line at low atmospheric pressure. The measurements were in good agreement with predictions made using HiTran '96 atmospheric data base. This verified the transmitter could be used to accurately measure the concentration of water vapor to within a few percent. A photon counting optical receiver was described that could

measure the low power, return lidar signal from the laser transmitter. A theoretical prediction of the maximum altitude over which this mini-lidar could measure atmospheric water vapor concentration was made using data from past missions to Mars. Although the current instrument would be limited to low altitude measurements, simple improvements would enable the lidar system to measure the dynamics of the water vapor up to 5km and aerosols, such as dust and ice, up to 15km. Using this lidar to measure the dynamics of the lower atmosphere would provide valuable information crucial to understanding the past and present climate of Mars.

APPENDICES

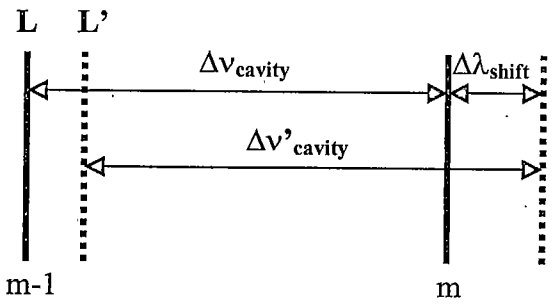
APPENDIX A

COMPARISON OF EXTERNAL CAVITY MODE SPACING WITH MODE SHIFT WHILE TUNING THE WAVELENGTH OF THE ECDL

The wavelength of the ECDL can be continuously tuned by synchronously changing the cavity length as the prism is rotated. Changing the length of the external cavity will not only shift the wavelength of the modes but also change their relative spacing. It is shown below that the change in spacing can be ignored for a large number of external cavity modes and small change in the overall cavity length.

Consider the frequency spacing of the m^{th} mode of the external cavity in air (n = 1) at length L and at L':

$$\Delta\nu_{cavity} = \frac{c}{2L}; \quad \Delta\nu'_{cavity} = \frac{c}{2L'}$$



The difference between the frequency spacing between the modes at slightly different cavity lengths ($L \simeq L'$) is:

$$(\Delta\nu - \Delta\nu')_{cavity} = \frac{c}{2}\left(\frac{1}{L} - \frac{1}{L'}\right) \cong \frac{c}{2}\left(\frac{\Delta L}{L^2}\right)$$

To determine the wavelength shift of the m^{th} mode by changing the cavity length from L to L', consider the wavelength that satisfies the resonant condition of the external cavity.

$$\lambda = \frac{2L}{m}; \quad \lambda' = \frac{2L'}{m}$$

The difference in the wavelength leads to a wavelength shift of:

$$\Delta\lambda_{shift} = \frac{2\Delta L}{m}$$

which can be expressed in terms of a shift in optical frequency using:

$$\Delta\nu_{shift} = \frac{c\Delta\lambda_{shift}}{\lambda^2} = \frac{c2\Delta L}{\lambda^2 m}$$

Substituting in the resonant condition for the cavity wavelength $\lambda = 2L/m$:

$$\Delta\nu_{shift} = \frac{cm\Delta L}{2L^2} = m(\Delta\nu - \Delta\nu')_{cavity}$$

That is, the variation in the mode spacing as the cavity tunes is m times less than the shift in frequency the m^{th} mode travels while changing the cavity length from L to L'. For this particular external cavity, the variation in the mode spacing can be ignored since the number of cavity modes is so large:

$$m = \frac{2L}{\lambda} = \frac{2(.0575 \text{ meters})}{(935 \cdot 10^{-9} \text{ meters})} = 123{,}000 \text{ modes}$$

APPENDIX B

SPATIAL MODES IN THE OUTPUT BEAM OF THE ECDL

Occasionally, the output of the 935nm ECDL was not single mode, even though the external cavity was designed to allow only one longitudinal mode. The laser would emit two or three wavelengths simultaneously! It is believed that these extra wavelengths were due to the excitation of spatial modes inside the laser diode and not longitudinal modes of the external cavity. After discussions with the manufacturer, it was determined this particular laser diode was gain guided and not index guided [13]. This means the width of the waveguide inside the laser diode is determined by the electrical contact above the active region. Index guiding defines the width of the waveguide more accurately by surrounding the sides of the waveguide with a material of a different index of refraction. As a result, the waveguide in this particular laser is able to support higher order spatial modes in addition to the lowest order mode down the center of the waveguide (Fig. B.1)

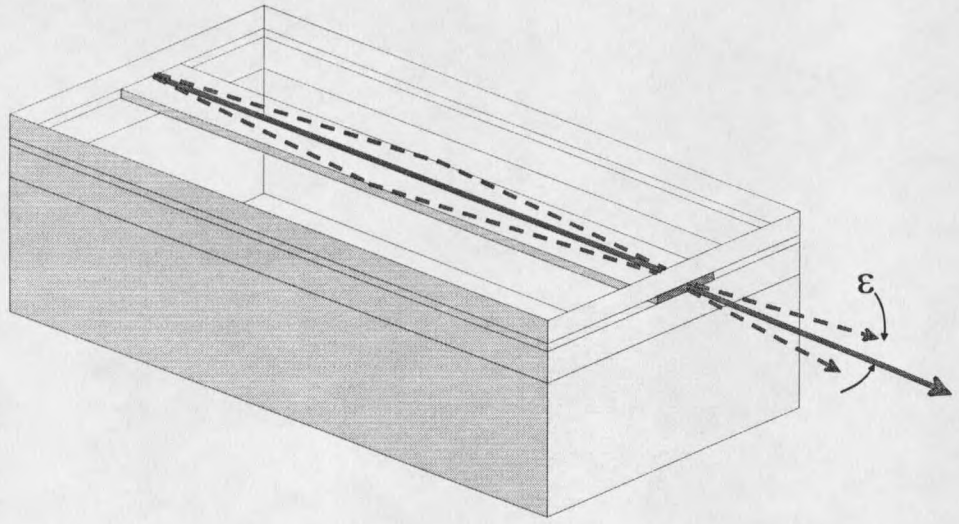


Figure B.1. Spatial modes of the gain guided, 935nm laser diode.

Emission from higher order spatial modes (shown by the dashed lines above) exit the laser at slightly different angles $\pm \varepsilon$ than the lowest order mode (shown by the solid line). This slight variation in the angle of incidence of the higher order spatial modes will be diffracted by the grating at a different wavelength for a given diffraction angle β.

$$\lambda = d[\sin(\alpha \pm \varepsilon) + \sin(\beta)]$$

These new wavelengths will be reflected by the beam folding prism and returned to the laser to be amplified. Once in awhile, the wavelength of the laser could be tuned from the lowest order spatial mode to a higher order spatial mode, emitting two wavelengths simultaneously (Fig. B.2.)

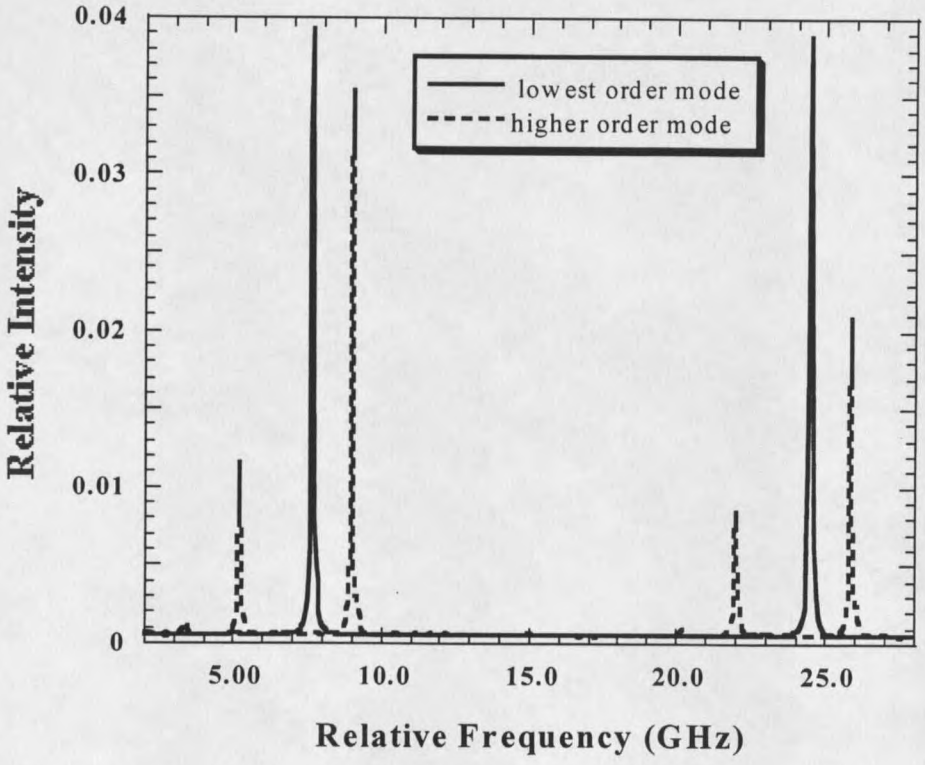


Figure B.2. Frequency output of the lowest and higher order spatial modes.

The higher order spatial mode also appeared in the spatial profile of the output beam as two lobes instead of a single gaussian-shaped lobe of the lowest order mode (Fig. B.3).

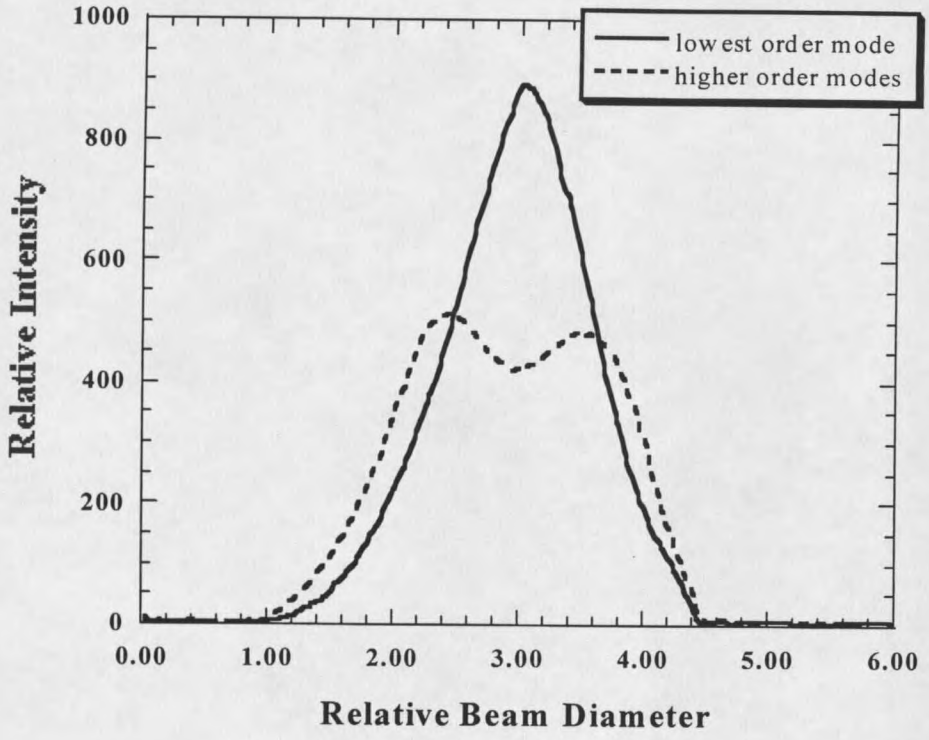


Figure B.3. Spatial profile of the lowest and higher order spatial modes.

These spatial modes appeared more frequently at higher drive currents which increased the gain for all possible modes in the waveguide. Spatial modes could be identified from longitudinal modes of the cavity in three ways. First, the modes would run simultaneously instead of hopping from one mode to the next. Second, the spacing of the modes could be changed by tuning the wavelength of the external cavity. Finally, the multimode output could be made single mode by blocking part of the beam folding prism. This last method was used to suppress the spatial modes as much as possible during continuous wavelength scans. Still, spatial modes caused a great deal of

confusion during the characterization of the ECDL. It is highly recommended that only index guided laser diodes be used as the gain element for external cavity diode lasers.

APPENDIX C

UNDERGRADUATES AND THEIR PROJECTS

I have listed a few of the several students that I had the fortunate opportunity to advise and a brief summary of their projects. I felt there should be some sort of permanent record of the excellent work these students did during the few years I was able to work with them in Dr. Carlsten's lab. Working with them provided me with an understanding of their work and mine that I could not have gotten in any other way, for which I am deeply thankful. I only hope these students benefited a fraction as much from the experience as I did.

Tony Roberts

"Design and Improvement of a Ramp Generator"; Optical Science and Laser Technology Conference, MSU, Bozeman, MT, 1994.

Tony Roberts was the first undergraduate I worked together with in the lab. Tony was extremely talented and I learned a great deal from him. He was successful with many projects, one of which was reducing the noise on the output from a high voltage ramp generator made in-house by Genieve Anderson and Kevin Repasky. The ramp generator was used to drive a PZT that scanned the mirrors in our high-finesse cavities. Several of these cavities were built to measure laser linewidth and measure laser frequency stability [66]. The ramp generator was causing ripple in the transmission peak of the interferometer, reducing the accuracy of the linewidth and long term frequency stability measurements. Using his knowledge of electronics, Tony filtered out the ripple which reduced the distortion of the transmission peak (Fig C.1).

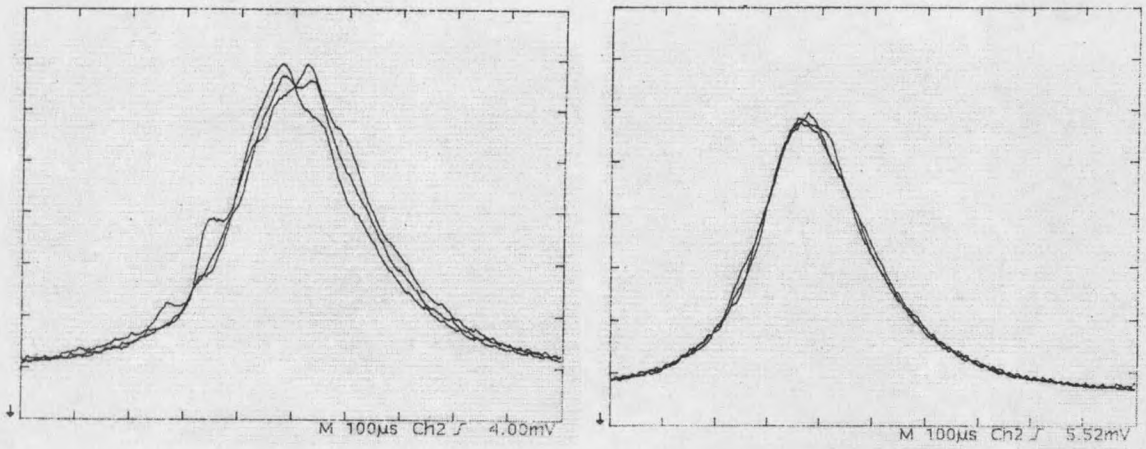


Figure C.1. Transmission of scanning, high finesse cavity before filtering (left) and after filtering (right) the voltage ramp.

Tony and I were the first in the lab to stabilize an external cavity diode laser to a Fabry-Perot cavity. Typical locking schemes stabilize the laser to the center of a transmission peak by dithering the output frequency back and forth across the peak, for instance. For better stabilization without dithering the frequency, we choose to stabilize the 780nm laser using a "DC" feedback scheme by locking to the side of a transmission peak of the cavity. For our first attempt, we controlled the feedback using a computer using a program Tony wrote, but we were limited by the speed of the computer and its interface with the equipment (Fig. C.2).

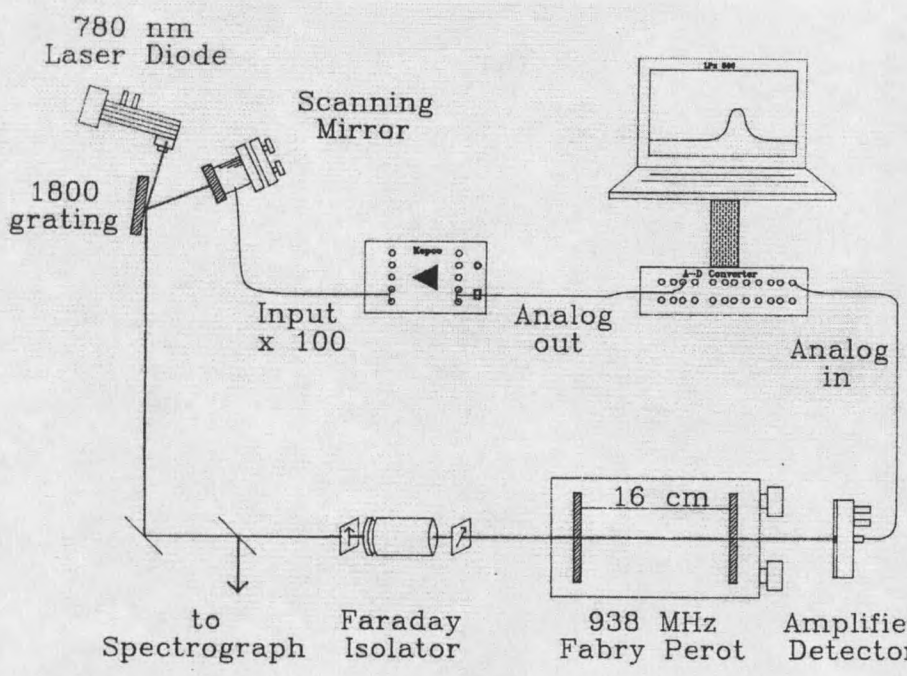


Figure C.2. Stabilizing the frequency of a 780nm ECDL to a Fabry-Perot using a computer. The computer was later replaced by a locking circuit to improve the response of the feedback loop.

To improve the speed of the feedback loop, Tony built a locking circuit that would continuously match a detector voltage monitoring the transmitted power through the cavity to a reference voltage [67]. If the detector voltage varied from the reference voltage, a potential was supplied to a PZT on the ECDL tuning its wavelength back to the side of the transmission peak. The laser was stabilized to the Fabry-Perot cavity to less than 300KHz over several minutes! Both the laser and the cavity were open to air currents in the lab. I later used this identical locking scheme while at NASA/GSFC to stabilize a DBR laser to a very weak water vapor line at 823nm. This set up was used to demonstrate the detection of water using single tone fm spectroscopy.

Tony is currently attending graduate school at Yale.

Amy Hyfield

"High Resolution Spectroscopy using an External Cavity Tunable Diode Laser"
Optical Science and Laser Technology Conference '96, Bozeman, MT.

Amy was an MSU chemistry undergraduate when she participated in Carlsten's lab in the summer of 1996. Her project was to set up an experiment to measure the absorption spectra of acetylene (C_2H_2) at 1530nm using an external cavity diode laser developed in the lab. The goal was to measure the center wavelength of a few of the absorption lines more accurately than the Fourier Transform Interferometer (FTIR) could in the Chemistry Department at MSU. It would also serve as a proving ground for using the newly developed ECDL for spectroscopy of gasses. Her activity in the lab made for a nice collaboration between Dr. Lee Spangler's lab in chemistry and Dr. Carlsten's lab in physics.

Amy began by designing and machining an 8" optical cell that could be evacuated and filled with acetylene at various low pressures. The cell was designed so that it would fit into the FTIR so the spectra of the same pressure of C_2H_2 could be compared. The cell was filled with welder's grade acetylene from the torch in the physics shop that contains 99% $C^{12}{}_2H_2$ and 1% $C^{13}{}_2H_2$. Her experimental set up is shown below (Fig. C.3).

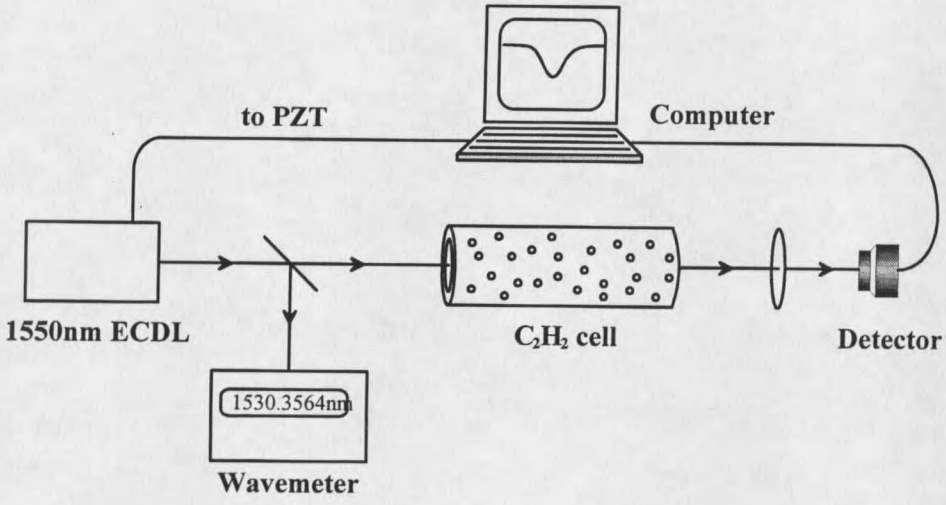


Figure C.3 Experimental setup for high resolution spectroscopy of acetylene using an ECDL built in the lab.

The PZT on the ECDL was scanned using a voltage ramp generated by a computer and driven with an A to D board. The output of the ECDL was sent through the optical cell containing acetylene and focused onto an amplified detector. The output of the detector was sent to a digital oscilloscope synchronized with the PZT scan. This generated a "scan window" for absorption lines to appear as the wavelength of the ECDL was mechanically set. Once an absorption line appeared, the scanning was turned off. The second half of Amy's program would finely scan the wavelength across the absorption line and record the signal from the detector. Using the data, the program would determine the minima and full width at half minima points of the absorption line and briefly set the laser wavelength to those points by supplying the correct voltage to the PZT. We could then read off the corresponding wavelength on the wavemeter, known to be accurate to $\pm$ 0.0002nm [38]. The absorption line could then be plotted using the data

file and label its center wavelength and full width at half minima as shown below. Over 20 such lines were characterized (Fig. C.4).

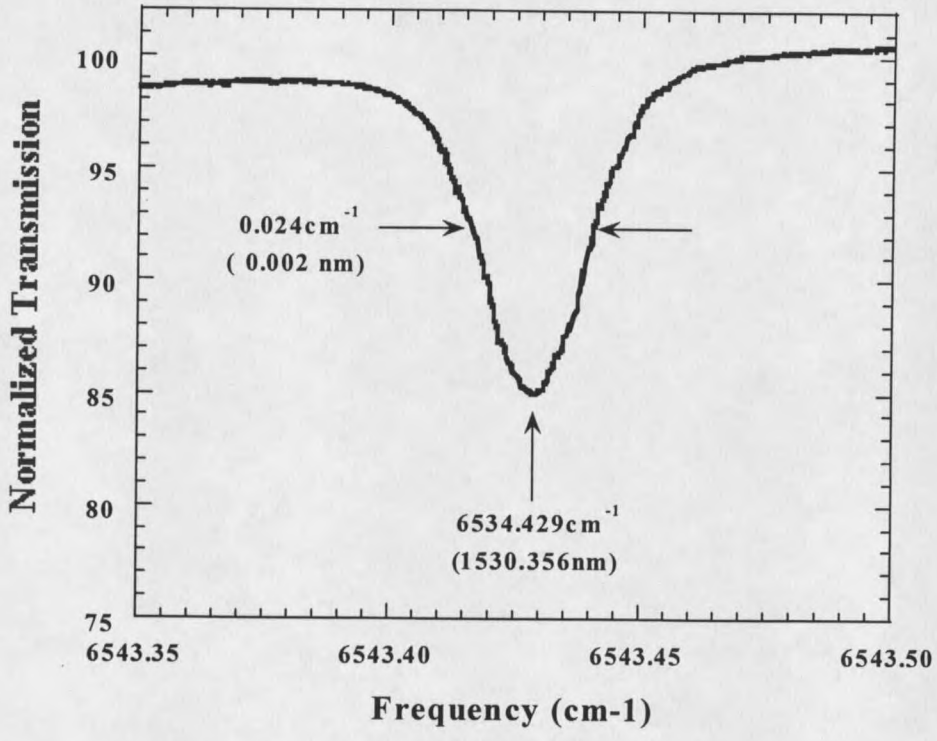


Figure C.4 A high resolution plot of the P9 absorption line of C_2H_2 at 24torr over an 8" path length. This plot contains over 800 points.

With this simple experiment, Amy achieved an accuracy and resolution of $0.001cm^{-1}$, a factor of 100 times that of the FTIR! Amy and I also learned to tell when the laser was not scanning single mode by identifying certain features in the absorption spectrum such as additional humps in the line (mode hops) or additional absorption lines (multi-mode). This was valuable experience for me when measuring the water vapor absorption lines in much the same way.

Before the end of the summer, Amy was hired part time at Scientific Materials to characterize crystals for lasers and other applications. One of her responsibilities was to measure the absorption spectrum using the FTIR in the chemistry department. Amy is now a graduate school in the Department of Chemistry at Montana State University.

Keith Ypma

"Optical Spectrum Analyzer Calibration Source Using Acetylene"; Optical Science and Laser Technology Conference '97, Bozeman, MT.

Keith was a physics undergraduate student that came into the lab during his senior year looking to acquire some practical lab experience to improve his upcoming employment opportunities. At the same time, ILX Lightwave was very interested in developing a device that could accurately calibrate optical spectrum analyzers in the $\lambda =$ 1550nm region. Based on the Amy Hyfield's previous work, the acetylene absorption lines provided accurate wavelength references in that region and seemed like a natural solution to the problem. Keith developed a low cost, very compact, sealed, optical cell that could hold acetylene gas at 500Torr (Fig. C.5).

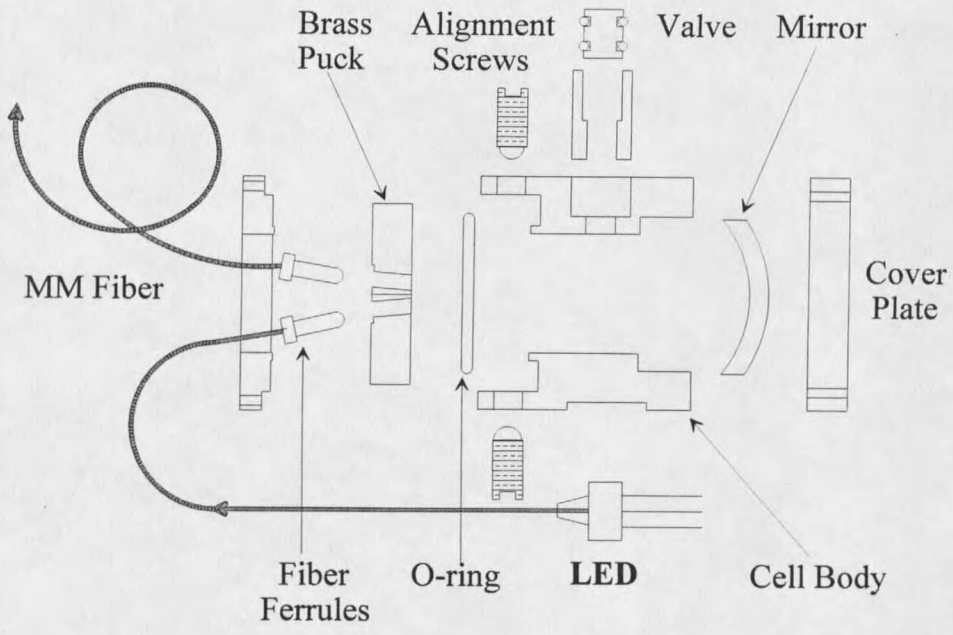


Figure C.5. Acetylene absorption cell used as a calibration source for optical spectrum analyzers.

Light from a broad band, $\lambda = 1530$nm, fiber coupled LED was sent into the acetylene cell where it was allowed to diverge from the 62.5μm, multi-mode fiber. The light was reflected back across the cell using an inexpensive, gold plated curved mirror and was focused into a second multi-mode fiber used to deliver the output. The input and output fibers were aligned with the mirror using fine adjustment screws to optimize the coupling. A coupling efficiency of 80% was achieved in the absence of acetylene! The LED source was mounted to the outside of the aluminum acetylene cell to form a compact unit measuring only 29 x 44 x 50mm. This unit was installed inside a fiber optic source donated by ILX Lightwave and its internal current driver supplied the power to the LED. The result was a packaged calibration source that provided the absorption spectrum of acetylene with the flip of a switch. Keith measured the center wavelength of

several absorption lines using a tunable 1550nm ECDL developed in the lab and the Burleigh wavelength meter. A few of these line-center wavelengths are listed below.

Table C.1. Center wavelength of a few acetylene absorption lines.

Absorption Line Number	Center Wavelength Measured by Keith	Center Wavelength Measured by NIST
P - 1	1525.762nm	1525.76nm
P - 3	1526.885nm	1526.87nm
P - 5	1527.992nm	1528.01nm
P - 7	1529.168nm	1529.18nm
P - 9	1530.362nm	1530.37nm
P - 11	1531.590nm	1531.59nm

Keith's results are in excellent agreement with NIST implying the calibration cell can be made traceable to NIST standards [68]. The acetylene cell was then used to calibrate our optical spectrum analyzer and compare this calibration against the factory calibration and calibration using a HeNe laser source at $\lambda = 633$nm (Fig. C.6).

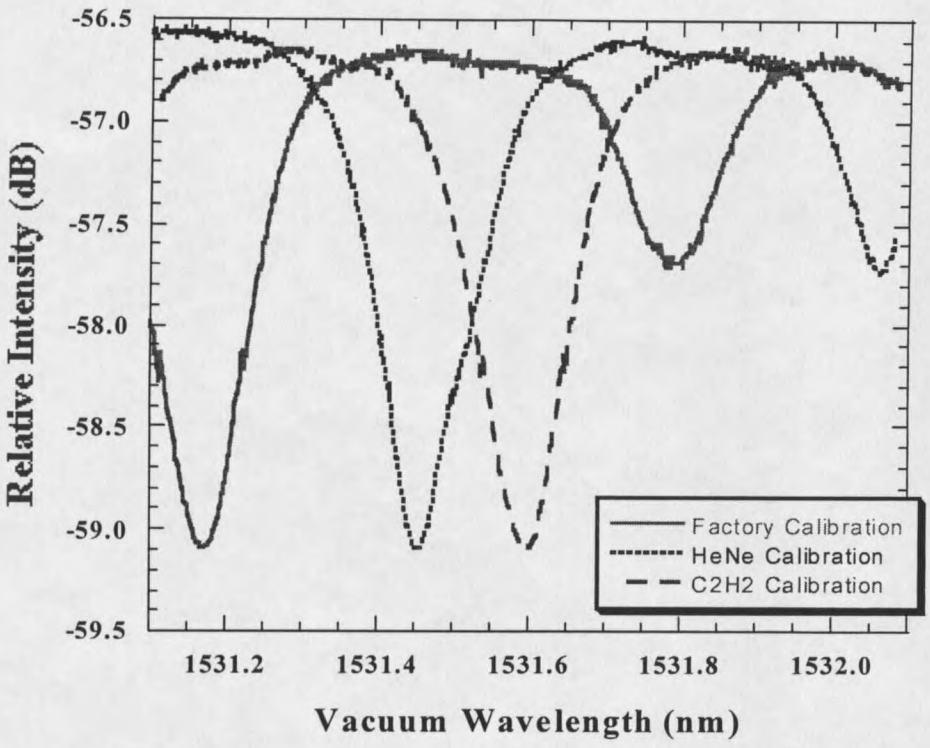


Figure C.6. The P - 11 absorption line measured with the optical spectrum analyzer. The center of the absorption line differs from the actual center at $\lambda = 1531.590$nm depending on which source was used to calibrate the spectrum analyzer.

The center of the absorption line differed from the actual wavelength by 0.14nm when calibrated with a HeNe laser at 633nm and by 0.42nm using the factory calibration. The error in the center wavelength of the P - 11 absorption line illustrates the importance of calibrating the optical spectrum analyzer with Keith's calibration source.

Keith was immediately employed by ILX Lightwave and is currently working as an engineer at Hewlett-Packard in California.

Misty Bare

"External Cavity Diode Laser: An Example of Technology Transfer"; Optical Science and Laser Technology Conference '96, Bozeman, MT.

Misty was a physics undergraduate student that came into the lab during her senior year also looking to acquire some practical lab experience. She was interested in working in a local, high-tech industry but felt she needed a broader technical background. We began by characterizing laser diodes at $\lambda = 1550$nm that could be used in the external cavities currently under development at ILX Lightwave. The lasers were then installed in an external cavity and its output performance was correlated to the initial output characteristics of the laser diode. This proved to be very important when specifying the parameters the laser diodes must meet when placing an order with the laser diode vendors. These tests were also used to decide the output specifications of the ECDL's that would be used for the wavelength settable, fiber optic source (Fig. C.7).

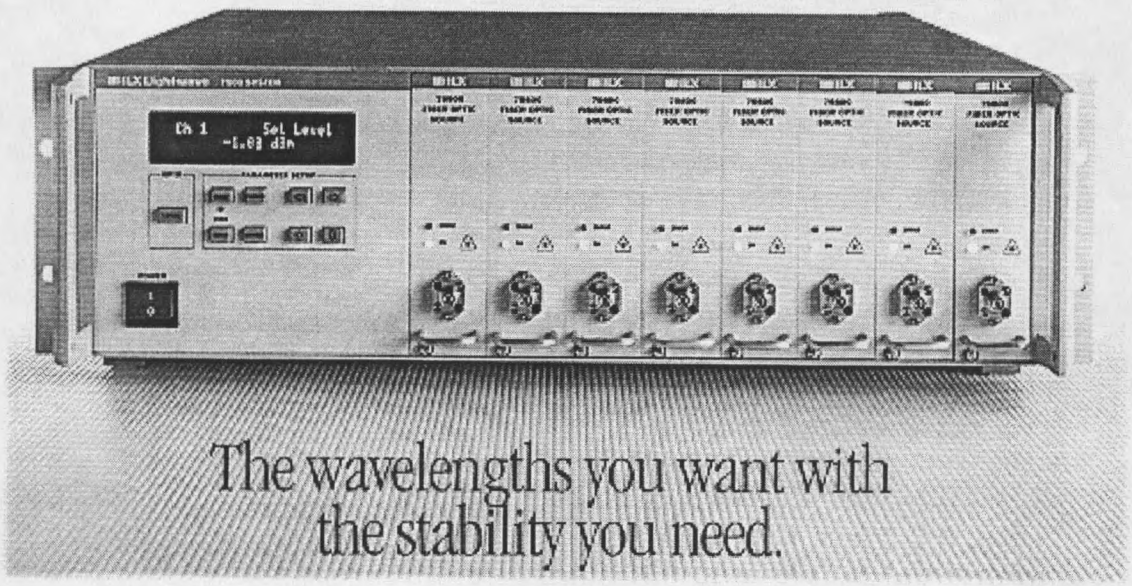


Figure C.7. FOS 79870 8-channel fiber optic source developed with ILX Lightwave.

This settable, fiber optic source contains eight, ECDL's developed in collaboration with the Carlsten lab and is a successful product for ILX Lightwave.

Misty is currently one of the primary sales representatives for fiber optic components at ILX Lightwave in Bozeman, MT.

Kevin Flanagan

"Laser Diode Beam Profiler"; Optical Science and Laser Technology Conference '96, Bozeman, MT.

Kevin was a physics undergraduate student that came into the lab early his sophomore year out of interest and curiosity. Although he had no previous experience, Kevin quickly became familiar with much of the equipment in the laboratory and soon became a near-expert machinist in the machine shop. He evaluated the plans for the laser diode beam profiler proposed earlier that year by a group of mechanical engineering students [39]. After making some improvements and simplifications to the design, Kevin machined, assembled and aligned the components for the beam profiler (Fig. C.8).

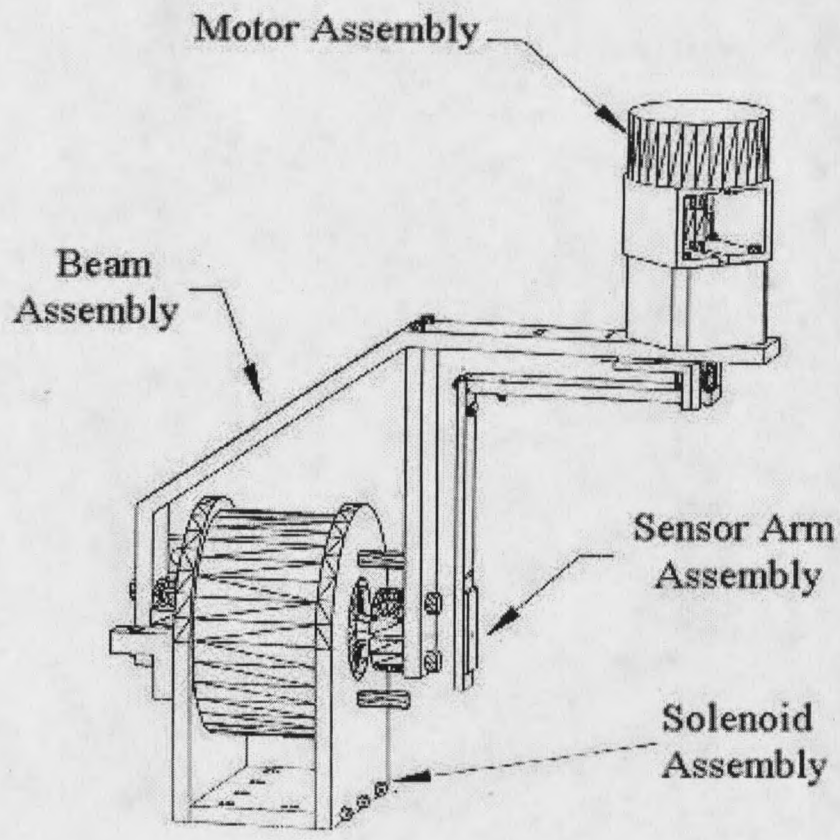


Figure C.8. Mechanical drawing laser diode beam profiler.

The profiler is able to measure the divergence angle of optical sources by scanning a detector in front of the source at a fixed radius of 3". This method can be used to accurately measure farfield beam profiles of highly divergent sources such as laser diodes. The beam assembly can be rotated to scan the intensity along the horizontal or vertical plane. A computer is used to step the sensor arm in 0.5 degree increments and record the optical power using an detector placed behind a small 250μm aperture. Later, Kevin replaced the detector with a fiber optic coupler that could deliver the light to an optical spectrum analyzer. This allowed us to measure both the power and wavelength as

a function of angle. This configuration was used to measure the frequency dependent spatial modes of vertical cavity surface emitting laser diodes (VCSELs) [69].

Kevin's farfield beam profiler was immediately used to characterize laser diodes both in the lab and for the ECDLs used in the ILX Lightwave, 8 channel fiber optic source. The profiler also provided the first hint that the 935nm laser diodes could possibly support multiple spatial modes along the wide axis of the waveguide [Appendix B]. Notice the double lobed output in the horizontal direction emitted from one of the laser diodes that we chose not to use in the ECDL (Fig C.9).

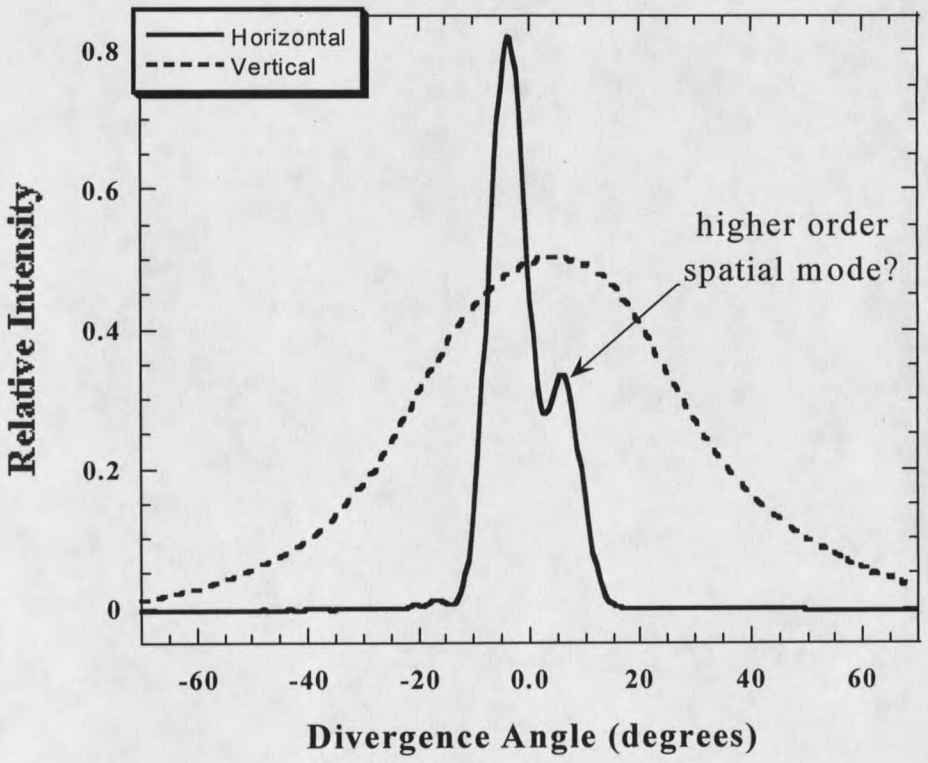


Figure C.9. Beam profile of the output from 935nm laser diode using Kevin's beam profiler. The horizontal sweep lies in the same plane as the wide, 3μm axis of the waveguide.

The profiler is currently being used to measure the divergence angles of lensed, single mode fibers that will be used to fiber pigtail laser diodes. This device has been extremely useful for many of the laser diode studies done in the lab.

Kevin is currently a senior in Physics at Montana State University and still an important member of our lab.

REFERENCES CITED

REFERENCES CITED

1. M.H. Carr; Water Vapor on Mars; Oxford University Press, 1996.

2. W.T. Silfvast; Laser Fundamentals; Cambridge University Press, 1996.

3. J.B. Abshire, J.A.R. Rall, J.D. Spinhirne, R.M. Hardesty, M.A. Krainak, S.M. Lord; "Planetary miniature lidar for water vapor, aerosol and temperature profiles from Mars"; Proposal to the NASA Planetary Instrument Definition and Development Program; Aug. 1, 1995.

4. G.W. Switzer; "High power laser diode transmitter to measure water vapor and temperature of the atmosphere on Mars"; NASA Graduate Student Researchers Program Proposal; awarded Sept. 1, 1996.

5. N. Holonyak, Jr., "The semiconductor laser: a thirty-five-year perspective"; Proceedings of the IEEE, Vol. 85, No. 11, November 1997.

6. R.N. Hall, G.E. Fenner, J.D. Kingsley, T.J. Soltys, and R.O. Carlson, "Coherent light emission from GaAs junctions"; Physical Review Letters, Vol. 9, No. 9, November 1962.

7. N. Holonyak, Jr. and S.F. Bevacqua, "Coherent (visible) light emission from $Ga(As_{1-x}P_x)$ junctions"; Physical Review Letters, Vol. 1, No. 4, December 1962.

8. M.I. Nathan, W.P. Dumke, G. Burns, F.H. Dill, Jr., and G. Lasher, "Stimulated emission of radiation from GaAs p-n junctions"; Physical Review Letters, Vol. 1, No. 3, November 1962.

9. T.M. Quist, R.H. Rediker, R.J. Keyes, W.E. Krag, B. Lax, A.L. McWhorter, and H.J. Zeigler, "Semiconductor maser of GaAs"; Physical Review Letters, Vol. 1, No. 4, December 1962.

10. I. Hayashi, M.B. Panish, P.W. Foy, and S. Sumski, "Junction lasers which operate continuously at room temperature"; Physical Review Letters, Vol. 17, No. 3, August 1970.

11. E. A. Rezek, N. Holonyak, Jr., B.A. Vojak, G.E. Stillman, J.A. Rossi, D.L. Keune, and J.D. Fairing, "LPE $In_{1-x}Ga_xP_{1-z}As_z$ (x~0.12, z~0.26) DH laser with multiple thin-layer (<500 A) active region"; Applied Physics Letters, Vol. 31, No. 4, August 15, 1977.

12. E.A. Rezek, H. Shichijo, B.A. Vojak, and N. Holonyak, Jr., "Confined-carrier luminescence of a thin $In_{1-x}Ga_xP_{1-z}As_z$ well (x~0.13, z~0.29, ~400A) in an InP p-n junction"; Applied Physics Letters, Vol. 31, No. 8, October 15, 1977.

13. Special thanks to Sensors Unlimited in Princeton, NJ. Model #: SU935-CD-FP

14. S. O'Brien, D.F. Welch, R.A. Parke, D Mehuys, K. Dzurko, R.J.Lang, R Warts, D. Scifres; "Operating Characteristics of a High-Power Monolithically Integrated Flared Amplifier Master Oscillator Power Amplifier"; IEEE Journal of Quantum Electronics, Vol. 29, No. 6, June 1993.

15. L.A. Coldren, S.W. Corzine; Diode Lasers and Photonic Integrated Circuits; John Wiley and Sons, 1995.

16. E. Kato, H. Noguchi, A. Ishibashi, "Significant profress in II-VI blue-green laser diode lifetime"; Electronics Letters, Vol. 34, No. 3, February 5, 1998.

17 Z. Shi, M. Tacke, A. Lambrecht, H. Bottner, "Midinfrared lead salt multi-quantum-well diode lasers with 282K operation"; Applied Physics Letters, Vol. 66, No. 19, May 8, 1995.

18. Buus, J., Single Frequency Semiconductor Lasers, SPIE Optical Engineering Press, 1991.

19. K. Liu and M.G. Littman, "Novel geometry for single-mode scanning of tunable lasers," Optics Letters, Vol. 6, 1981.

20. P. McNicholl and H.J. Metcalf, "Synchronous cavity mode and feedback wavelength scanning in dye laser oscillators with gratings"; Applied Optics, Vol. 24, No. 17, September 1, 1985.

21. L.F. Stokes; "Accurate measurement of reflectivity over wavelength of a laser diode antireflective coating using an external cavity laser"; Journal of Lightwave Technology, Vol. 11, No. 7, July 1993.

22. D.M. Braun, R.L. Jungerman, "Broadband multilayer antireflection coating for semiconductor laser facets"; Optics Letters, Vol. 20, No. 10, May 15, 1995.

23. Thanks for the useful discussions with Chris Cook and T.Y Fan at MIT Lincoln Labs in Lexington; MA, September 10, 1996.

24. The author is indebted to Dr. John Connolly at Sarnoff Corporation for his help in providing a state-of-the-art AR coating for the front facet of the 935nm laser diode used in this project.

25. P.J.S. Heim, Z.F. Fan, S.H. Cho, K. Nam, M. Dagenais, F.G. Johnson, R. Leavitt; "Single-angled-facet laser diode for widely tunable external cavity semiconductor lasers with high spectral purity"; Electronics Letters, Vol. 33, No. 16, July 31, 1997.

26. Frank Fan, Peter Heim, Etc. with 50dB side mode suppression ratio. Also, author used SAF devices in ECDL's at 960nm and 1530nm for high resolution spectroscopy of water vapor and acetylene respectively.

27. Special thanks to Steve Finn at Spectrogon Inc. in Parsippany, NJ for his many usuful discussions and information about holographic gratings.

28. E. Hecht, Optics, 2nd edition, Addison-Wesley Publishing Company, 1987.

29. 40-50% coupling efficiency can be measured by focusing light from an external source such as an ECDL at 935 into the waveguide of a 935nm laser diode and measuring the photocurrent generated by the diode. This technique is discussed in section 3.2.

30. B.E.A. Saleh, M.C. Teich, Photonics, John Wiley and Sons, Inc., 1991.

31. G.S. Hayat, G. Pieuchard, "Classically ruled diffraction gratings (C.R.D.G.)"; Jobin Yvon-Spex, Edison, NJ, 1973.

32. Margaret M. Hall; "Low Frequency Intensity Noise in Semiconductor Lasers"; Ph.D. Thesis, Montana State University, 1996.

33. P. Zorabedian; "Tunable External-Cavity Semiconductor Lasers"; Tunable Lasers Handbook, Academic Press 1995.

34. T. Day, F. Luecke, M. Brownell for New Focus Inc; "Continuously Tunable Diode Lasers"; Lasers and Optronics, June 1993.

35. Amy Hyfield, Gregg Switzer; "High Resolution Spectroscopy using an External Cavity Tunable Diode Laser"; Optec '96 Conference, Bozeman, MT. See also Appendix C.

36. Fiber Fabry-Perot Tunable Filter is commercially available from Micron Optics Inc. Atlanta, GA; model FFP-TF-935 and controller, FFP-C.

37. 7900 Modular Fiber Optic Source; ILX Lightwave, Bozeman, MT. This product provides up to 8 modular channels containing a fiber-coupled sources setable to $1525<\lambda<1570$nm. The ECDL used in this source was developed as a collaborative project between ILX Lightwave and the Carlsten lab.

38. W.S. Gornall; "Model WA-1500 Wavemeter Accuracy Analysis";Technical Note for Burleigh Instruments Inc.; received from Burleigh May 1998 and an informative discussion over the phone with Pual Kruly, Customer Service Manager at Burleigh.

39. Greg Ault, Russell Evertz, Sanna Watson; "Laser Diode Beam Profiler", ME 302 design project report with instructor Robb Larson and in collaboration with Gregg Switzer, Carlsten Lab and Thad Orosz and Kent Noonan, ILX Lightwave; May 3, 1996.

40. K. Flanagan, Gregg Switzer; "Laser Diode Beam Profiler"; Optec Conference; Bozeman, MT, Sept. 7, 1996.

41. J.A.R. Rall; "Differential Absorption Lidar Measurement of Atmospheric Water Vapor Using a Pseudonoise Code Modulated AlGaAs Laser"; Ph.D. dissertation, NASA Technical Memorandum 104610, July 1994.

42. Flared Semiconductor Amplifiers are commercially available from SDL, Inc, San Jose, CA.

43. D. Mehuys, S. O'Brein, R.J. Lang, A. Hardy, D.F. Welch; "5W, diffraction-limited, tapered-stripe resonator semiconductor laser."; Electronics Letters, Vol. 30, No. 22, Oct. 27, 1994.

44. This optical configuration was developed by Dr. Don Cornwell, at NASA/GSFC which was successfully used to collimate flared amplifiers for the Antarctic Geophysical Observatory lidar.

45. D.M. Cornwell; "Miniature lidar wind profiler"; Ph.D. Dissertation; University of MD, Electrical Engineering; May 1998.

46. O'Shea, Callen, Rhodes; An Introduction to Lasers and their Applications; Addison-Wesley Publishing, 1977.

47. High-current laser modulator designed and built by Mr. Alan Lukemire of Space Power, Inc. MD. The modulator was originally designed to drive the amplifiers on the Antarctic Geophysical Observatory lidar program.

48. The author is indebted to Mariusz "Marty" Miodek for writing the Labview software used to make this measurement.

49. L.M. Little, P.D. Dragic, S.D. Roh, J.J. Coleman, G.C. Papin; "Initial development of a fiber-based lidar system for atmospheric water vapor measurements"; 19th International Laser Radar Conference, Annapolis, MD, July 7, 1998. This group at the University of Illinois, Urbana-Champaign, also collaborating with NASA/GSFC, is also developing a laser transmitter at 935. This system uses a custom DBR semiconductor laser to seed a fiber amplifier but is limited to a 100mW peak pulse power.

50. HiTran-PC, version 2.51, August 1997. Ontar Corp., North Andover, MA.

51. T.G. Kyle; Atmospheric Transmission, Emission and Scattering; Pergamon Press, 1991.

52. HiTran-PC; users manual, Ontar Corp, North Andover, MA.

53. "Relative Humidity and Temperature Transmitters"; model HX93; Omega Engineering, Inc. Stamford, CT.

54. H.H. Kieffer, B.M. Jakowsky, C.W. Snyder, M.S. Matthews; Mars, University of Arizona Press, 1992.

55. "The Pathfinder" 10m multipass optical cell, CIC Photonics, Albuqerque, NM.

56. R.M. Measures; Laser Remote Sensing; Krieger Publishing Company, 1992.

57. D.S. Colburn, J.B. Pollack, R.M. Haberle; "Diurnal variations in optical depth at Mars: observations and interpretations"; NASA Technical Memorandum 100057, May 1998.

58. J.T. Schofield; "The Mars Pathfinder Atmospheric Structure Investigation/Meteorology (ASI/MET) Experiment"; Science, Vol. 278, December 5, 1997.

59. P.H. Smith, et al.; "The imager for the Mars Pathfinder experiment"; Journal of Geophysical Research, Vol. 102, No. E2, February 25, 1997.

60. J.D. Spinhirne; "Micro Pulse Lidar"; IEEE Transactions on Geoscience and Remote Sensing, Vol. 31, No. 1; January 1993.

61. P.H. Smith et al.; Results from the Mars Pathfinder Camera"; Science, Vol. 278, December 5, 1997.

62. The author is indebted to Dr. Spinhirne at NASA/GSFC for his assistance and sharing his insight on this matter.

63. J.A. Reagan et al.; "Lidar sensing of aerosols and clouds in the troposphere and stratosphere"; Proeedings of the IEEE, Vol. 77, 1989.

64. J.D. Spinhirne et al.; "Vertical distribution of aerosol extinction cross section and inference of aerosol imaginary index in the troposphere by lidar technique"; Journal of Applied Meteorology, Vol. 19, 1980.

65. J.A. Reagan et al.; "Assesment of extinction to backscatter ratio measurements made at 694.3nm in Tucson, Arizona"; Aerosol. Science Technology, Vol. 8, 1984.

66. K.S. Repasky, L.E. Watson, J.L. Carlsten; "High-finesse interferometers"; Applied Optics, Vol. 34, No. 15; May 20, 1995.

67. K.B. MacAdam, A. Steinbach, C. Weiman, "A narrow-band tunable diode laser system with grating feedback, and a saturated absorption spectrometer for Cs and Rb"; American Journal of Physics, Vol. 60, No. 12, December 1992.

68. S.L. Gilbert, W.C. Swann, "Acetylene $^{12}C_2H_2$ absorption reference for 1510-1540nm Wavelength Calibration - SRM2517"; NIST special publication 260-133, US Government Printing Office, January 1998.

69. P.A. Roos, J.L. Carlsten, D.C. Kilper, K.L. Lear "Diffraction from oxide confinement apertures in VCSELs"; CLEO 98, San Fransisco May 7, 1998.

MONTANA STATE UNIVERSITY - BOZEMAN
3 1762 10421226 9